Performance Improvement of Switched Reluctance Motor (SRM) Drives Through Online Optimization Based Reference Current Identification and Digital Sliding-Mode Control

PERFORMANCE IMPROVEMENT OF SWITCHED RELUCTANCE MOTOR (SRM) DRIVES THROUGH ONLINE OPTIMIZATION BASED REFERENCE CURRENT IDENTIFICATION AND DIGITAL SLIDING-MODE CONTROL

BY

SUMEDH BHASKARRAO DHALE, B.E, M. Tech.

A THESIS
SUBMITTED TO THE DEPARTMENT OF ELECTRICAL & COMPUTER ENGINEERING
AND THE SCHOOL OF GRADUATE STUDIES
OF MCMASTER UNIVERSITY
IN PARTIAL FULFILMENT OF THE REQUIREMENTS
FOR THE DEGREE OF
DOCTOR OF PHILOSOPHY

Doctor of Philosophy (2021) McMaster University
(Electrical & Computer Engineering) Hamilton, Ontario, Canada

TITLE:	Performance Improvement of Switched Reluctance Motor (SRM) Drives Through Online Optimization Based Reference Current Identification and Digital Sliding-Mode Control
AUTHOR:	Sumedh Bhaskarrao Dhale B.E.(Electrical Engineering), M. Tech.
SUPERVISOR:	Dr. Ali Emadi IEEE Fellow Canada Excellence Research Chair Laureate
CO-SUPERVISOR:	Dr. Babak Nahid-Mobarakeh IEEE Senior Member
NUMBER OF PAGES:	xxv, 199

Dedicated to my mother, Saroj

In the memory of my father, Bhaskarrao Dhale

Abstract

This thesis presents a torque control mechanism for switched reluctance machine (SRM) drives. The proposed mechanism is capable of maintaining ripple free torque control while minimizing the copper loss or mode-0 radial force or both at a fixed switching frequency.

In the proposed approach, the torque control problem is addressed by splitting it into two parts. The first part consists of identification of optimum phase current references while the second part incorporates the design of an efficient current controller. For the identification of optimum phase current references, three algorithms are presented in the form of a developmental process. The nature of the online optimization problem is demonstrated using a simple 2-dimensional gradient descent method. Subsequently, a parametric form gradient descent algorithm is presented which transforms the original optimization problem into two 1-dimensional problems, viz. torque error minimization and identification of optimum search direction. This method yields improved computational efficiency and accuracy. The third algorithm incorporates projection using equality constraint on the phase torque contributions to achieve a 1-dimensional solution process. Although this algorithm takes more iteration as compared to the parametric form gradient descent algorithm, it demonstrates greater accuracy and computational efficiency. A comparative analysis of these algorithms is performed in at different operating conditions in terms of the torque ripple magnitude and computational effort.

The thesis also presents a comprehensive analysis of well known control techniques for application in SRM current control in discrete-time domain. This analysis also presents a comparative evaluation of these control techniques under different operating conditions. On account of this analysis, several recommendations pertaining to the performance improvement are presented.

Finally, a digital sliding-mode based model-free current controller suitable for fixed switching frequency operation is presented. The proposed controller is capable of providing a consistent dynamic response over wide operating range without utilizing any model information. The reference current tracking performance of this controller is verified through simulation studies in MATLAB/Simulink® environment and over a 1.2kW, 100V, 2500RPM, 12/8 experimental SRM drive.

Acknowledgements

I would like to begin by expressing my sincere gratitude to my supervisor Dr. Ali Emadi for providing me with the opportunity to pursue the Ph.D. degree under his supervision and offering the necessary support and guidance. His work ethic and vision inspired me throughout my Ph.D. studies. I would also like to thank him for showing exceptional leadership and care during Covid-19 crisis. Because of his support, my colleagues and I suffered negligible impact on our studies.

I would like to thank my co-supervisor Dr. Babak Nahid-Mobarakeh for supporting me through the most critical phase of my Ph.D. journey. His knowledge and ability to elucidate the most difficult of the concepts helped me in the development of my own understanding of electric machines and the principles of control system. I thoroughly enjoy having technical discussions with him and I strive to achieve the clarity and wisdom with which he tackles the technical challenges.

I am extremely grateful to Dr. Timothy Davidson for helping me understand the complex theoretical principles in non-linear optimization. His enthusiasm and creative thinking motivated me to pursue the complex problems in electric motor control and estimation using nonlinear optimization.

I will be ever grateful for the assistance I received from late Prof. J. K. Zhang. I will always remember him as a very patient and wise educator.

I would also like to thank Dr. Shamsuddeen Nalakath and Dr. Aniket Anand for wholeheartedly supporting me with their excellent technical insights and engineering skills.

I would like to thank the members of my supervisory committee, Dr. Mehdi Narimani and Dr. Jin Ye for providing valuable feedback on my progress and their insightful comments.

I was fortunate to attend the courses conducted by Drs. Jenifer Bowman, Mehdi Narimani, Berker Bilgin and Saeed Habibi. These courses played a vital role in development of the foundation of my Ph.D. thesis.

I would like to thank Dr. Phil Kollmeyer, Theresa Mitchelle, Teresa Janes, Dan Manolescu, Paul Nguyen and Dr. Peter Azer for their excellent management of the lab activities. Thanks to their efforts and agility, my colleagues and I are able to safely carry out experimental studies amid Covid-19 crisis.

I am thankful to my former senior colleagues, Dr. Yashomani Kolhatkar, Dr. Arvind Kumar Tiwari, Rahul R. Pillai and P Veena from Ge Global Reaserch for providing me with useful career advice.

I would like to take this opportunity to thank my masters supervisor Dr. N Rajasekar for supporting me in beginning of my journey as a researcher.

I want to thank my friends Carin Yeghiazarian, Dr. Atriya Biswas, Alex Wang, Amirreza Poorfakhraei, Dr. Negar Noroozi, Jeremy Lempert, and Lucas Bruk for their support and encouragement.

I would also like to acknowledge the support from my lab colleagues, Silvio Rotilli Filho, Joshua Taylor, Wesam Taha, Zisui Zhang, Drs. Rasul Tarvirdilu Asl, Zekun Xia and Diego Valencia.

I want to remember my colleagues Late Dr. Iman Aghabali and Mehdi Eshaghian who tragically lost their lives in the plane crash earlier in 2020. Their loss is irrecuperable for the entire engineering community. I will cherish the fond memories of them forever.

I am extremely grateful, to my mother for being relentlessly optimistic and showing great patience towards me. Her passionate approach in her job has inspired me since childhood. I will always be grateful to my late father who is remembered for his hard working attitude and academic achievements. I also want to thank my sister for taking all the responsibilities in my absence. Above all, I am grateful to my family for the virtues which always helped me navigate through the challenges in my life.

Abbreviations and Symbols

Abbreviations

SRM	Switched Reluctance Machine/Motor
PE	Power Electronics
PM	Permanent Magnet
TSF	Torque Sharing Function
OLTSF	Online Torque Sharing Function
ATC	Average Torque Control
DTC	Direct Torque Control
DITC	Direct Instantaneous Torque Control
DATC	Direct Average Torque Control
LLC	Low-Loss Control
DIT&FC	Direct Instantaneous Torque & Force Control

FL	Feedback Linearization
ITC	Indirect Torque Control
D	Dimension
APOD	Alternate Phase Opposition Disposition
DC	Direct Current
AC	Alternating Current
EMF	Electromotive Force
PI	Proportional+Integral
LQR	Linear Quadratic Regulator
LQG	Linear Quadratic Gaussian
SISO	Single Input Single Output
MIMO	Multi Input Multi Outpu
CARIMA	Controller Auto-Regressive Integrated Moving Average
ARE	Algebraic Riccati Equation
LTV	Linear Time Varying
RLS	Recursive Least Square
SMC	Sliding Mode Control
MRAC	Model Reference Adaptive Control

DSMC	Digital Sliding Mode Control
LUT	Lookup Table
RPM	Revolutions Per Minute
PWM	Pulse-Width Modulation
DSP	Digital Signal Processor
IGBT	Integrated Gate Bipolar Transistor
IPMSM	Interior Permanent Magnet Synchronous Machine

Symbols

T_s, k, ω_s	Sample time, instant and frequency
i_{ph}, $\hat{i}_{ph}$, i_{ref}, i_c	Phase current, its estimation, reference current and its steady state value
ψ_{ph}, $\hat{\psi}_{ph}$, $\tilde{\psi}_{ph}$	Phase flux linkage, its measurement and its estimation error
d^*_{ph}, u^*_{ph}, u_{ph}	Controller output duty ratio, voltage, and phase terminal voltage
ϵ_{ph}, $\hat{\epsilon}_{ph}$, $\tilde{\epsilon}_{ph}$	Induced EMF per phase, its estimation and estimation error
ζ,η	Mis-matched disturbance and measurement noise
r_{ph}, $\hat{r}_{ph}$, $\tilde{r}_{ph}$	Phase resistance, its estimate, and estimation error
l_{ph}, $\hat{l}_{ph}$, $\tilde{l}_{ph}$	Phase inductance, its estimate, and estimation error

θ_m, N_r	Mechanical rotor position, and number of rotor poles
$\theta_{on}, \theta_{off}$	Turn off, and Turn on angles
θ_e, ω_e	Electrical rotor position, and speed
V_{dc}, $\hat{V}_{dc}$	Dc-link voltage and its measurement
λ	Pseudo integration variable
ω_{bw}	Closed-loop bandwidth
e_i, e_p	Current tracking, and parameter estimation errors
$\mathscr{G}_{pp}$	Controller gain via pole placement
K_p, K_i	Proportional and integral gains
W_{pre}, W_{post}	Pre, and post filters/compensators
H_p, H_c	Prediction and control horizons
A, B, x, u	State transition matrix, input matrix, state vector, input vector of a strictly linear system
e_{H_c}, u_{H_c}	Tracking error and control input vectors of length H_c
J,V	Quadratic cost and value functions
Q, R	Quadratic performance indices for control accuracy and and effort respectively
P, $\mathscr{K}$	Value matrix and control gain

ϕ	Input vector
p, $\hat{p}$, $\tilde{p}$	Parameter vector, its estimate, and error
σ, γ	Sliding surface and closed-loop pole
υ, ρ	Order of sliding mode, and magnitude of the discontinuous switching function
$\mathscr{V}$	Lyapunov candidate energy function
Γ	Parameter adaptation gradient
$\lvert\cdot\rvert, \lVert\cdot\rVert, \lVert\cdot\rVert_\infty$	1, 2, and Supremum norms respectively
$\mathscr{R}$	Magnetic Reluctance
ϕ_{ph}	Phase flux
N_{ph}	Number of phase turns
g_{ip}, A_{ov}	Airgap, and Overlap area
μ_0, μ_r	Permeability of free space, and Relative permeability of the magnetic material
T_e, T_{ripple}, T_{avg}	Electromagnetic torque, Torque ripple, and Average torque.
$n(X)$	Cardinality of a set X.
T_{ref-ss}	Steady state value of the reference torque dynamics
a_f, b_f, c_f	Coefficients of the reference torque dynamic equation

i_{ph-pri}, i_{ph-sec}	Primary, and Secondary phase currents
i_{max}	Phase current limit
T_{ph-pri}, T_{ph-sec}	Primary, and Secondary phase torques
J_{cu}	Objective function for copper loss minimization in 2-D gradient descent algorithm
W_t, γ_{ic}	Weighing functions for torque error and inequality constraints respectively
$\mathscr{V}_t, \mathcal{V}_\alpha$	Value functions for torque error minimization and identification of optimum search direction respectively
$\mathcal{V}_{cu}, \mathcal{V}_{rf}$	Value functions for copper loss and mode-0 radial force minimization respectively
W_w, W_v	Weighing functions for the objective of mode-0 radial force and DC-link voltage minimization
h	Reference Model
f_{ph}	Extended state continuous-time domain
δ_{ph}	Discrete-time domain equivalent of f_{ph}
$\mathscr{V}$	Lyapunov energy function
J	Magnitude of discontinuous switching function
L	Upper bound of unmodelled dynamics
V_{comp}	Auxiliary control voltage

Contents

List of Tables

List of Figures

Chapter 1

Introduction

1.1 Background

The unique construction of the 'Switched Reluctance Machine' (SRM) yields several attractive features. The most prominent ones include the rugged and fault-tolerant construction, low manufacturing cost, and simple geometry [Krishnan (2017)]. Compared to its PM counterparts, higher fault-tolerance, and greater structural robustness make the SRM drive a better candidate for applications involving harsh operating conditions such as aircraft power generation [Radun (1994)], [Richter (1988)], gas turbine starter/generators [Richter and Ferreira (1995)] and mining [Hao and Pavlitov (2009)]. Additionally, the cost-effectiveness makes it a desirable candidate for applications in domestic appliances and HVAC [Bilgin *et al.* (2019)].

The induction machines have long since dominated the field of industrial drives on the strength of their self-starting capability and simpler construction than the synchronous machines. Following the rapid development in power electronics technology over the last few decades, the inverter fed AC machine drives are becoming increasingly common owing to their quicker dynamic response, and wider operating range compared to line start machines [Bose (2020)]. With the aforementioned advantages, this development has also aided the candidature of the SRM drives against induction machine drives for variable-speed industrial applications.

The SRM also stands out against its singly excited sisters: the synchronous reluctance machine (SynRM) and mutually coupled SRM (McSRM). Although both of these machines support balanced operation with a 3-ph AC power supply, the former has lower power density [Bostanci *et al.* (2017)] while the latter suffers from inferior torque quality and power factor [Li *et al.* (2016)].

1.1.1 Switched Reluctance Machines (SRMs) for Automotive Applications

The rise in global awareness associated with the environmental impact of the conventional internal combustion engines has lead to the exploration of cleaner propulsion technologies. Mainly, the hybrid-electric and fully electric drivetrain technologies have paved the way for vehicular electrification. This development have created a huge demand for the electric machines with following specifications [Chan (2002); Zhu and Howe (2007)].

- High torque and power densities
- Wide controllable operating speed
- Intermittent overload capability
- High reliability

- Cost-effectiveness
- Low torque ripple
- Low acoustics noise and radial vibrations

The permanent magnet (PM) synchronous and induction are the most successful candidates among the electric machines finding utility in the commercial electric vehicles either as a traction motor or a motor-generator device. The success of these machines can be attributed to their superior power density, torque quality and high reliability [Hashemnia and Asaei (2008)].

The PM synchronous are the most expensive among the commercially available electric machines suitable for electric drive train application due to the presence of rare-earth permanent magnets in their rotor constitution. Ever fluctuating market prices of the permanent magnets pose a considerable obstacle in the mass utilisation of these machines [Bilgin *et al.* (2020)]. The induction machines on the other hand, enjoy the advantage of a rugged PM-free and simple rotor construction. However, they exhibit relatively lower efficiency. This limitation is often countered by using copper bars in the rotor cage, which inevitably leads to a higher cost.

The SRM is the simplest, cheapest, and most rugged among the promising electric machine technologies available today. However, lower power density, higher torque ripple, acoustic noise, and radial vibrations are the main challenges in its adoption for application in electric propulsion [Bostanci *et al.* (2017)]. The recent research in this field has proved that a substantial improvement in the performance of an SRM drive can be achieved when these challenges are approached from the control point of view [Liaw *et al.* (2020)]. Therefore, development of an advanced torque control technology capable of mitigating these challenges is a very promising research field having the potential to promote SRM for the exigent automotive applications.

1.2 Motivation

The SRM drive exhibits a highly nonlinear surjective relationship between the phase voltages and electromagnetic torque. This relationship is also influenced by the rotor position and magnetic saturation in iron core. For an individual phase, such a nonlinear relationship also exists between the phase voltage and the magnitude of the radial force [Gan *et al.* (2018); Garrigan *et al.* (1999)], as well as the power conversion loss and voltage utilization [Hasegawa *et al.* (2002); Yu *et al.* (2015)]. In a typical low to medium power SRM, the operation of each phase is independent of the rest due to the insignificant mutual coupling [Li *et al.* (2009)]. However, the overall performance of the machine can be optimized by balancing the torque contribution from each phase. This principle forms the basis for all the torque control techniques for SRM directed towards achieving a smooth torque while maintaining an optimum balance among the remaining objectives such as copper loss minimization, radial force control, extension of base speed etc.

1.2.1 Torque Control Techniques for SRM Drives

The most popular torque control techniques for SRM in literature are classified as, direct torque control (DTC), indirect torque control (ITC), and intelligent [de Paula *et al.* (2020); Seshadri and Lenin (2019)]. A DTC technique is characterized by a control structure in which the command voltage or the power converter switching state is directly dictated by the desired reference torque while ITC consists of an intermediate torque distribution, and reference current identification mechanisms, followed by a current controller [Xue *et al.* (2009)]. The attractive feature of emulating the nonlinear electromagnetic behaviour of SRM via online learning has inspired application of several intelligent control techniques to the torque control problem such iterative learning control (ILC) and fuzzy-logic control [Kamalakannan *et al.* (2011)].

The current profiling is an analogous technique to TSF where the phase current references are identified either online, or offline and stored in the form of lookup-tables (LUTs) [Keerthana and Sundaram (2020)]. Owing to their identical nature, the terms current profiling and TSF are often used interchangeably.

Due to the highly nonlinear doubly salient geometry of SRM, it also exhibits highly nonlinear torque characteristics. Owing to this aspect of SRM and its significance, the reduction of torque ripple is regarded as a primary objective in almost all the advanced SRM torque control techniques [Liu *et al.* (2020)].

The evolution of the advanced torque control techniques can largely be attributed to the limitations of 'Average Torque Control' (ATC) technology in attaining the acceptable torque quality. In ATC, the phase current reference is generated through a torque control loop where, torque feedback is achieved using the average torque estimation unit. The conduction period of each phase and the commutation angles are predetermined through either FEA, experimental analysis or online estimation [Husain (2002)]. The offline conduction angles can also be optimized for achieving reduced torque ripple and in some cases, the copper loss and radial forces. A typical ATC implementation on a 3-ph. SRM is shown in Fig.(1.1).

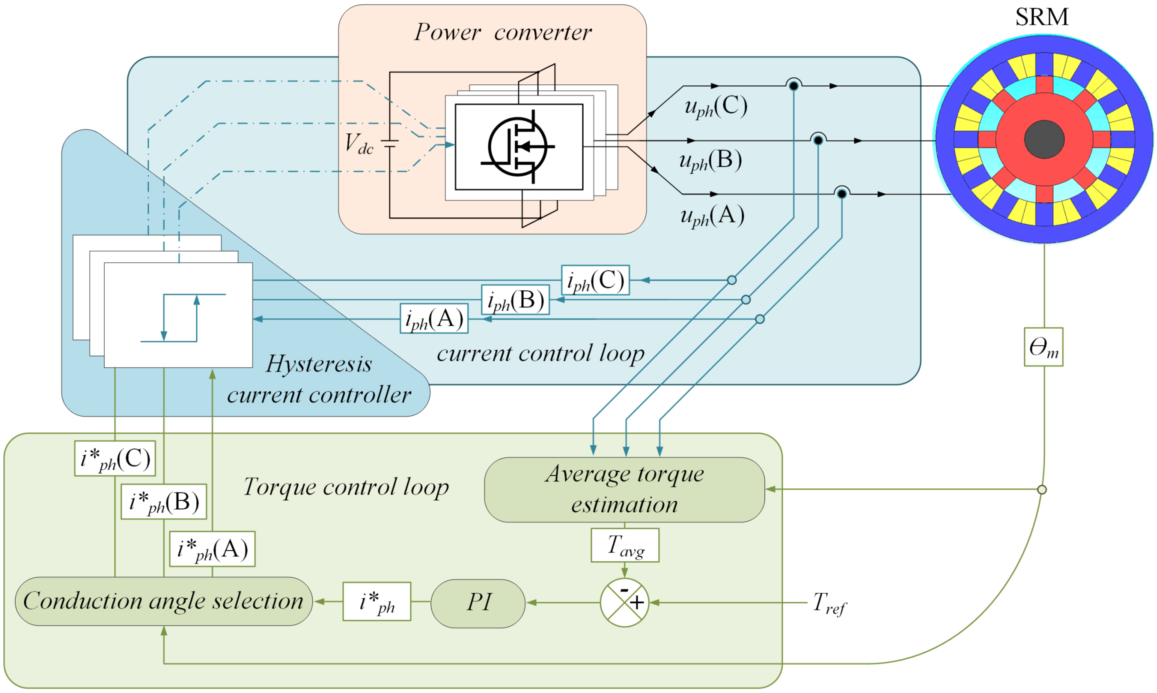

Figure 1.1: Average torque control of a 3-ph. SRM drive

The bandwidth of torque control loop in ATC is limited by the dynamic response of the torque estimation unit. To overcome this challenge, the torque estimation is either realized through an LUT [Husain and Ehsani (1996)], speed dynamics [Husain (2002)] or flux linkage dynamics [Inderka and De Doncker (2003b)]. This limitation also dictates that the reference current remains constant over a conduction period. Therefore, the objectives of torque ripple, copper loss, and radial force reduction etc. can only be achieved through optimization of the span and instant of the conduction period for each phase [Banque *et al.* (2005); Mademlis and Kioskeridis (2003)].

The fixed nature of the commutation angles as well as the reference current magnitude over an electrical cycle proved to be insufficient in terms of performance enhancement, as the optimum set of commutation span and instances vary significantly for different operating conditions. This led to an investigation into the identification of optimum commutation angles over the entire operation map of the drive [Fisch *et al.* (1997)].

Although the optimized commutation in ATC provided a substantial improvement in the drive performance, it still remained inferior to that of the popular AC machines which inspired further advancements as discussed ahead.

Direct Torque Control (DTC)

The earliest among the DTC methods proposed in the literature is 'Direct Average torque control' (DATC) [Inderka and De Doncker (2003b)]. In DATC, a voltage model is used to calculate the average torque through online estimation of flux linkage. This estimated torque is then used to correct the reference current output achieving greater immunity to DC link fluctuations. DATC still relies on offline calculation of commutation angles and reference currents specific to each operating condition and only incorporates the objective of torque ripple reduction.

The offline calculation of commutation angles and current references is a very exhaustive process and need large memory in micro-controller for the storage of these parameters specific to each operating condition. Inderka and De Donker mitigated this issue through complete elimination of the current loop. The torque control is directly implemented using torque estimation feedback and a hysteresis controller. This control structure is popularly known as 'Direct Instantaneous Torque Control' (DITC) [Inderka and De Doncker (2003a)]. DITC achieves the reference torque by utilizing the incoming phase to its fullest capacity while the outgoing phase only supplies the deficit. The control logic of DITC has also seen utility in the reduction of mode-0 radial force magnitude (DIT&FC) [Klein-Hessling *et al.* (2017)] and vibration reduction control [Zhang *et al.* (2019a)].

DITC is effective when the control logic is evaluated at each sampling instant. Moreover, the presence of a hysteresis controller makes this method incompatible with fixed switching frequency PWM operation. This limitation of DITC led to the development of predictive DITC control [Neuhaus *et al.* (2006)]. In this method, the prediction of future states at least for a unit sampling time period is performed using flux linkage and torque characteristics know as 'Predictive PWM-DITC' control. Using predictive PWM-DITC, simultaneous minimization of torque ripple, and copper loss is addressed in [Brauer *et al.* (2011)] by adding a 'Low loss control' (LLC) algorithm along with torque distribution mechanism. Whereas [Sun *et al.* (2020a)] employed adaptation in commutation angles for the same. A typical torque control loop using DITC/DITC&FC for 3-ph SRM is shown in Fig.(1.2). In comparison with its predecessor, the predictive DITC with LLC follows similar approach in copper loss minimization. DITC with predictive control has recently been successfully implemented for minimization of mode-0 radial force in [Weiss *et al.* (2020)]. This technique is yet to be explored for combined evaluation with LLC.

Feedback linearization provides an effective framework for application of linear controllers for SRM. In [Ilic *et al.* (1987)], this principle is used to linearize the torque control loop. Subsequently, the robustness of this control towards inexact feedback linearization is improved using parameter adaptation [Amor *et al.* (1993)], and Lyapunov energy function based corrective action [Sahoo *et al.* (2011)]. These techniques benefit from reliable and well established control principles. However, the torque distribution mechanism follows the similar logic as predictive PWM-DITC control leading to similar performance.

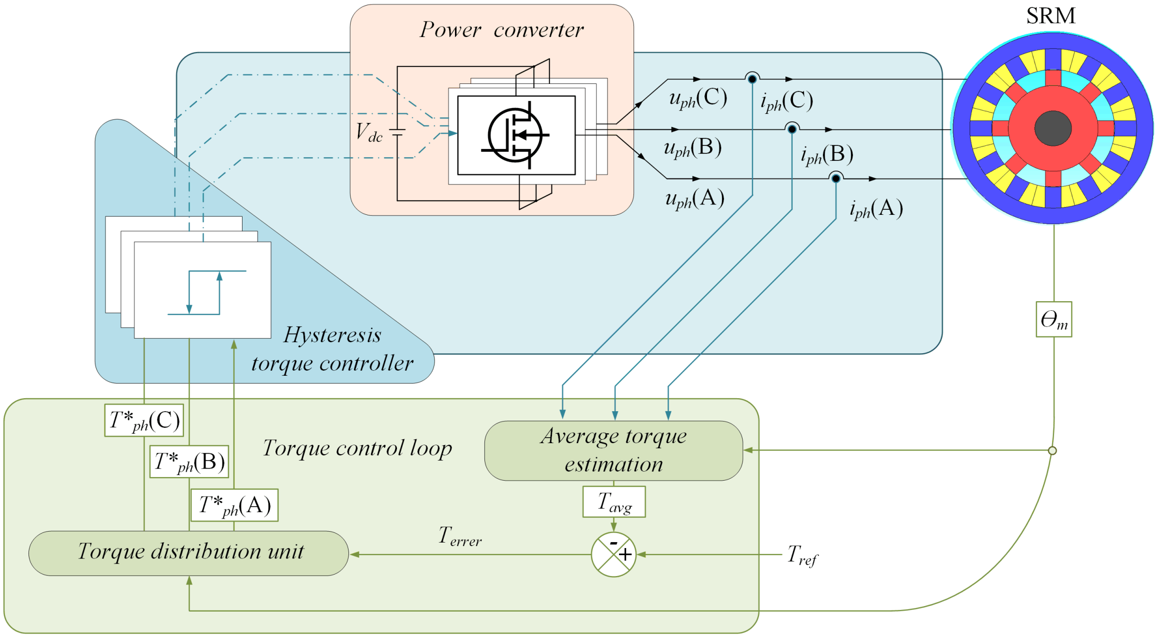

Figure 1.2: Direct instantaneous torque/torque and force control of 3-ph SRM

In a nutshell, the current state of art in direct torque control technology has been successful in performing the torque ripple reduction with fixed switching frequency via predictive PWM-DITC with copper loss minimization and mode-0 radial force minimization. However, the torque distribution mechanism utilized in these processes is very simple and favours incoming phase in all operating conditions which is contradictory to the objective of copper loss minimization in low to medium speed range. The investigation into combined application of LLC and mode-0 radial force minimization is necessary to optimize the torque control performance online for specific operating conditions.

Torque Sharing Functions (TSFs) and Current Profiling

Control via torque sharing functions is a promising area of performance improvement in SRM drives. Since their advent [Ilic-Spong *et al.* (1987)], the TSFs have been utilised in the identification of optimum current reference profiles while achieving multiple of the control objectives such as: torque ripple minimization [Husain (2002); Lee *et al.* (2009)], torque ripple and copper loss minimization [Li *et al.* (2018); Ye *et al.* (2015)] and radial force reduction [Callegaro *et al.* (2019)]. The principle types of the TSFs are, Offline [Mikail *et al.* (2013); Ye *et al.* (2015)] and Online [Lee *et al.* (2009)]. In literature, The Offline TSFs have been studied rigorously for identification of optimum phase current profiles mainly using heuristic algorithms such as GA [Li *et al.* (2018); Xia *et al.* (2020)]. Due to their heavy computational load, these algorithms are not suitable for online applications. The main limitation with the offline TSFs is their inability to maintain consistent performance across wide operating conditions.

Online realization of TSFs with a fixed set of rules is attempted in [Lee *et al.* (2009)]. This approach successfully mitigated the issue of performance degradation due to variation in operating conditions. However, similar to the predictive PWM-DITC, the torque distribution disproportionately favours the incoming phase with a presupposition that it benefits the objective of copper loss reduction. A very pragmatic approach is presented in [Harikrishnan and Fernandez (2016)] where the optimum torque sharing is first identified via computer simulation followed by a comparative analysis to identify the nature of variation in torque sharing. This knowledge is then utilized to develop an efficient scheme for online implementation of TSF based control. This approach is further developed by base speed extension [Al-Amyal *et al.* (2020)] and [Maksoud (2020)]. The torque control of a 3-ph SRM drive using a typical TSF based ITC is shown in the Fig.(1.3).

Recently, the online implementation of popular optimization algorithms has been

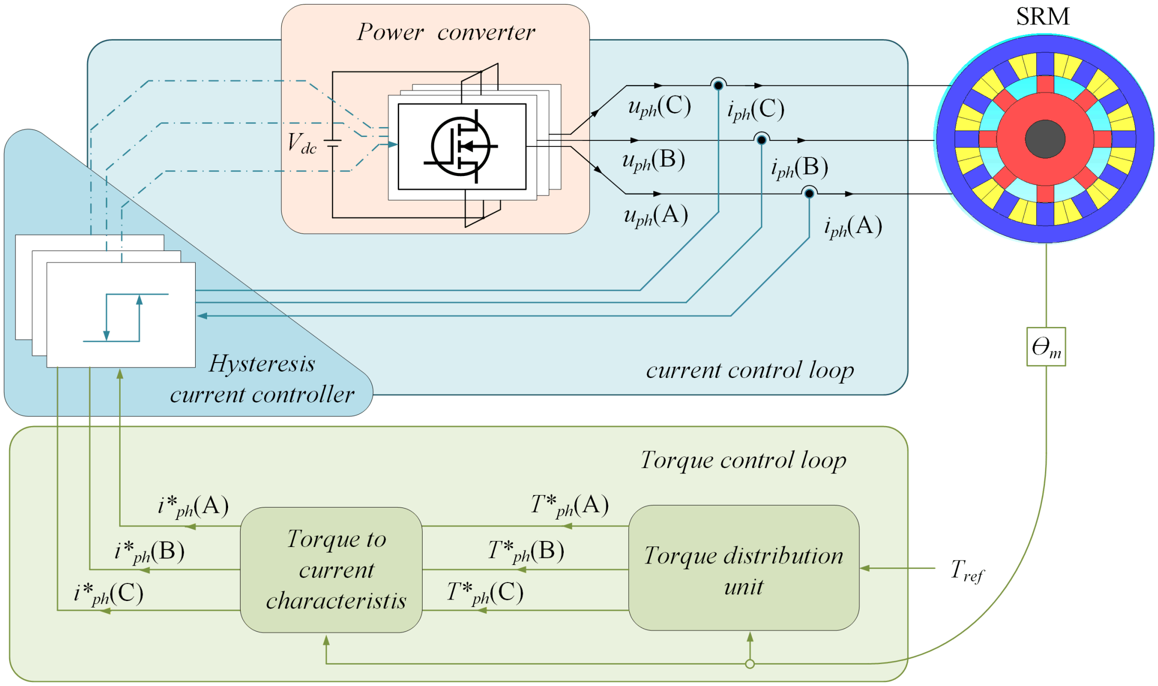

Figure 1.3: Indirect torque control of a 3-ph SRM drive

reported for torque ripple and copper-loss reduction in [de Paula and Barros (2021)] where the steepest-descent based optimization is employed to identify optimum torque distribution while the regulation is achieved via sliding mode control. This method does not provide direct control over current which is a well known disadvantage of DITC in addition to the variable switching frequency. Due to their high computational inefficiency, the population based heuristic algorithms are implemented with huge restrictions [Abdel-Maksoud (2020); Song *et al.* (2020); Üstün and Önder (2020)]. A more efficient optimization approach is attempted in [Anuchin *et al.* (2020)] for torque control with copper loss reduction as a secondary objective however their scope is still limited till offline implementation.

Other Promising Control Techniques

The intelligent control techniques provide very simple mechanisms for modelling the input-output behaviour of the SRM. Especially, the use of 'Artificial Neural Network' (ANN) technology has been extensively used for modelling the electromagnetic characteristics [Belfore and Arkadan (1997); Ustun (2009)], estimation [Lu *et al.* (2003)], and control [Rahman *et al.* (1997)]. In [Sahoo *et al.* (2005); Sahoo *et al.* (2005)], the iterative learning control is employed to achieve reliable tracking of reference torque command while the principles of fuzzy logic control are employed in [Bolognani and Zigliotto (1996)]. Except the implementation framework, the intelligent control techniques have not been utilized to identify the optimum control variables to satisfy the above mentioned secondary objectives.

The tree diagram in Fig.(1.4) provides detailed classification of the control techniques discussed in this chapter.

Necessity of Fixed Switching Frequency Control

The most prominent advantage of fixed switching frequency operation as opposed to the variable one appears in terms of thermal management, mainly due to uniform distribution of power loss over an electrical cycle. This phenomenon also prevents premature aging of the power electronic devices and allows reliable operation with relatively less exhaustive cooling efforts. In addition, the electromagnetic interference management for fixed switching frequency operation is simpler as compared to its variable switching frequency counterpart [Wang (2017)]. In the light of these aspects, fixed switching frequency or PWM operation is a desirable characteristic of a control method.

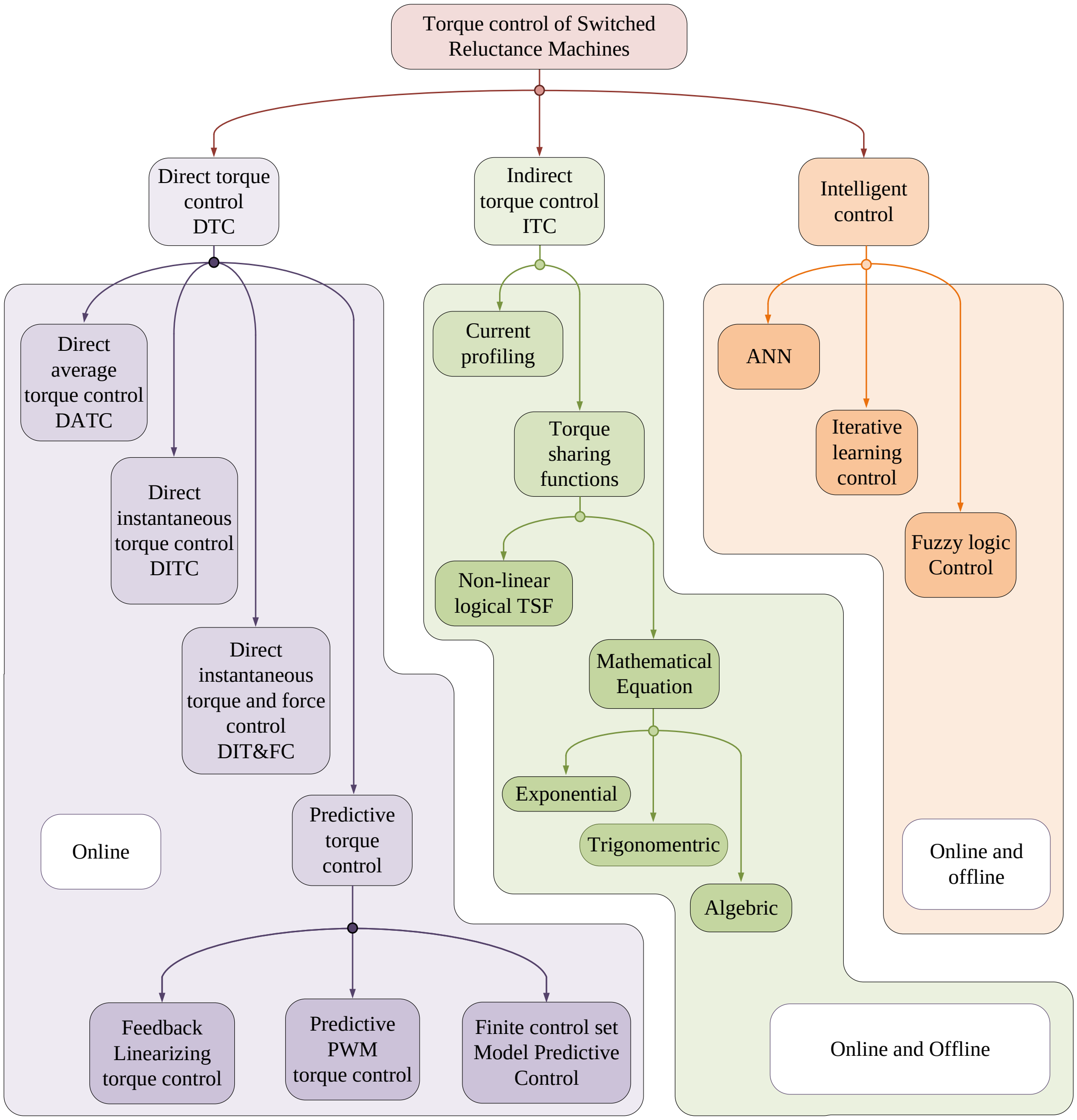

Figure 1.4: Classification torque control techniques for SRM

Performance Optimization in AC Machines vs SRMs

The objective of loss minimization control in electric machines is to achieve operation at a given operating point with minimum loss (copper loss or core loss), which leads to maximum torque per ampere (MTPA) and maximum torque per volt (MTPV) type of operation. Both MTPA and MTPV provide optimum magnitudes of electrical and field energies at desired operating point to achieve minimum loss. For all of the AC machines, the field and real power components are decoupled in the synchronous reference frame. Therefore, the MTPA solution is derived in the field and real power components of phase currents. In SRM, the field and real power components of phase current are nonlinear functions of rotor position also. Therefore, the objective of MTPA control becomes the identification of the optimal phase current profile over a phase commutation period. Specifically, the current waveform during the phase overlap period and the instant of commutation almost entirely determines the loss characteristics of SRM at a given operating point.

1.3 Contributions

The thesis presents the development of an efficient framework for identification and tracking of optimum phase current profiles to achieve reliable torque control while satisfying the following objectives:

i Torque ripple minimization

ii Copper-loss minimization

iii Radial force minimization

The contributions by the author associated with the above development are summarized below.

1 Development of a nonlinear optimization based algorithm for online identification optimum phase current references to achieve minimum copper-loss while maintaining very low torque ripple.

2 Expansion of the optimization algorithm developed for torque ripple and copper loss reduction by incorporating the objective of mode-0 radial force minimization.

3 A comprehensive review of fixed switching frequency current control techniques for switched reluctance machine drives. (Published in IEEE Access:[Dhale *et al.* (2021)])

4 Development of a robust model-free current regulator based on the principles of digital sliding mode control. (Submitted to the IEEE Transactions on Industrial Electronics)

Fig.(1.5) shows the above contributions in the context of the proposed torque control framework.

1.4 Thesis Outline

The proposed framework for online identification of current references and their control is elaborated through the subsequent chapters in this thesis as detailed below.

Chapter 2 introduces the electromagnetic principles of switched reluctance machines and describes their torque generation mechanism through the theory of electromechanical energy conversion. The chapter also describes in detail, the challenges pertaining to the torque control of the SRM drives.

Chapter 3 introduces the proposed framework for closed-loop torque control in discrete-time domain. It begins with the introduction to the nonlinear torque dynamics of the SRM with phase voltage as input and torque as output. Using this model, the admissible set of control inputs is defined for the reference torque dynamics. The objectives of copper loss and mode-0 radial force reduction are established in the form of optimization problems over this set of control inputs. The proposed simplification approach is performed by splitting this control problem in two parts. The first part being identification of optimum phase current references and the second part consists of current control. Finally, a detailed analysis of the nonlinear dynamics of SRM electromagnetic model is presented in the discrete-time domain and a set of performance criteria is established to assess the current control techniques reviewed in the next chapter.

Chapter 4 presents a comprehensive review of current control techniques suitable for fixed switching frequency current control of SRM. The most popular control techniques from the literature are identified and their operating principles are reviewed in the light of the control performance evaluation criteria established in Chapter 3. The summary of this evaluation is presented in the form a comparative analysis. The chapter concludes with proposed solutions for control performance enhancement using these control techniques.

Chapter 5 presents a robust model-free PWM current control method for SRM drives. The proposed technique is developed using the principles of digital sliding-mode control. In the presented approach, the necessary model information required to achieve a consistent closed-loop dynamic response is treated as an extended state and it is estimated online through a unit sample time delayed approximation to be used for control in subsequent time step. The deterioration in the control action due to the delay in estimation of the extended state and the noise in current measurement is corrected through an auxiliary control action derived from a Lyapunov energy function analysis. This control action provides a robust compensation for the mismatch between the estimation and real value of the extended state. Consequently, the resulting control law is capable of providing accurate tracking of reference current profile throughout the controllable operating range of the drive amid low signal to noise ratio and without using any a-priori model information.

Chapter 6 introduces the operating principles of the optimization algorithms for online identification of optimum phase current references of copper loss and mode-0 radial force reduction. These algorithms are presented in the form of a developmental process. Beginning with the most basic approach of 2-dimensional gradient descent, the chapter presents the nature and challenges related to the online optimization using SRM characteristics. Subsequently, a parametric form gradient descent algorithm is presented. This method benefits from a more efficient 1-dimensional optimization approach. Specifically, this method splits the 2-dimensional gradient descent algorithm into two 1-dimensional problems viz, optimum search direction identification and torque error minimization. This approach leads to more efficient solution identification than the 2-dimensional gradient descent algorithm. Finally a projected gradient descent algorithm is introduced. Unlike the parametric form gradient descent algorithm, this algorithm achieves reduction to 1-dimension through incorporation of equality constraint on one of the optimization variables.

Chapter 7 provides performance verification of the online optimization algorithms presented in Chapter 6. The 2-dimensional gradient descent and parametric form gradient descent algorithms are evaluated for copper loss minimization only while the projected gradient descent algorithm is also evaluated for mode-0 radial force minimization.

Finally, Chapter 8 provides the concluding remarks and possible avenues for improvement in performance of the control framework proposed in this thesis.

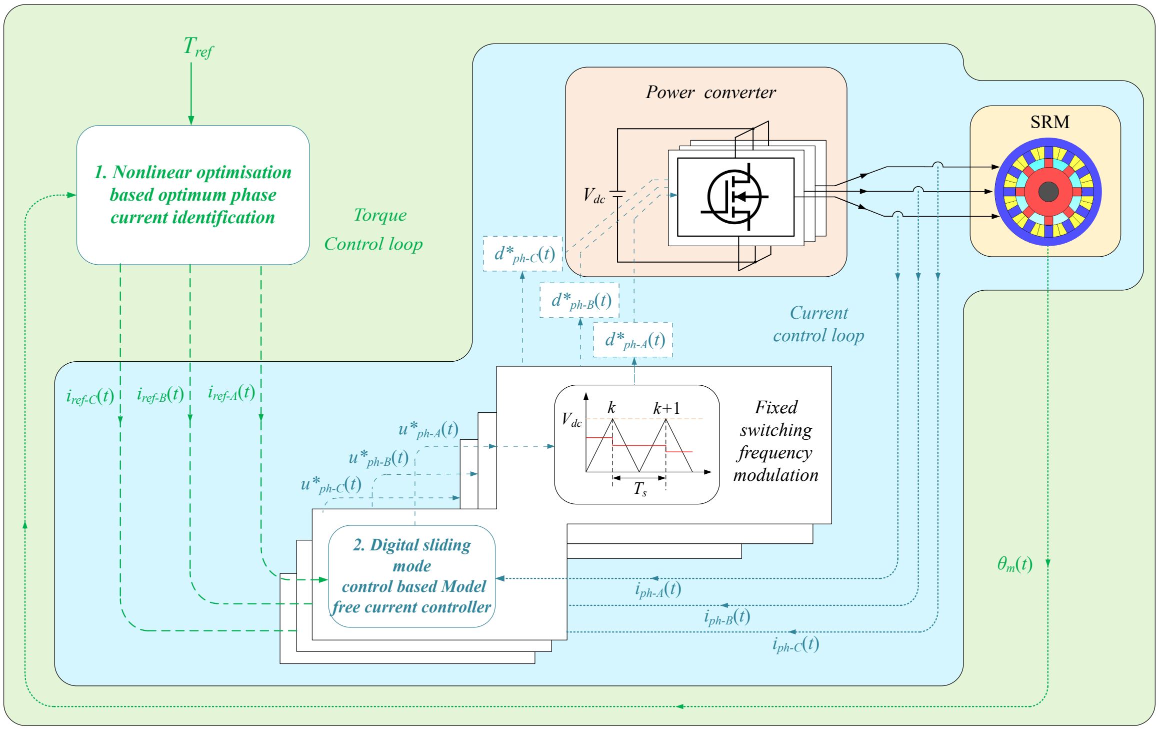

Figure 1.5: Thesis contributions

Chapter 2

Fundamental Principles of Switched Reluctance Machines and Challenges in Torque Control

2.1 Introduction

A successful demonstration of rotary motion via sequential switching of reluctance torque by W.H. Taylor had substantiated the concept of the SRMs as early as in 1838. Since then, the lack of efficient power conversion mechanism prevented realisation of an industrial grade SRM drive until the latter half of the 20^{th} century. The advent of power semiconductor technology has predominantly paved the way for the development of the modern SRM drive. Lawrenson and Agu [Lawrenson and Agu (1964)] theoretically validated the superior performance of SRM drives and expounded upon the technological breakthroughs in power semiconductor technology and their utility in development of the SRM drive [Lawrenson (1965)] known today.

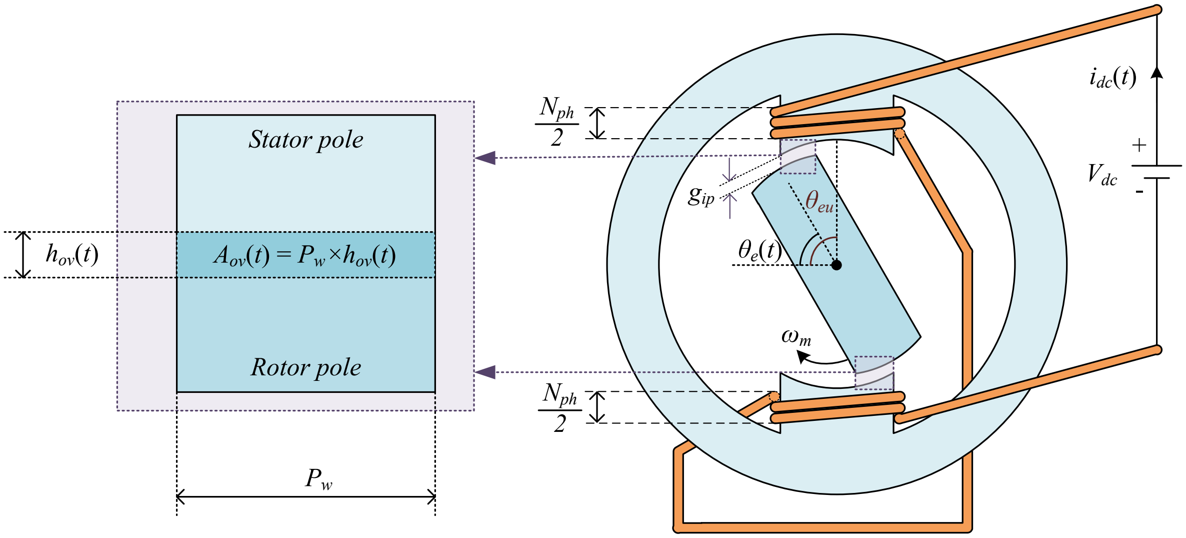

Figure 2.1: Torque generation principle of SRM

In this chapter, the operating principles an SRM drive are explained in detail. In the first half of this chapter, the principles of electromagnetic energy conversion are used to describe the torque generation mechanism and the unique nonlinear characteristics of an SRM. The latter half of the chapter presents the challenges pertaining to the torque control by comparing the operational characteristics of ideal and real world SRM drives.

2.2 Electromagnetic Principles

Magnetic Circuit

A typical SRM consists of a doubly salient geometry with stator housing the phase windings. The torque is generated by exploiting the fundamental property of electromagnetic flux to attain a magnetic circuit with least reluctance. Subsequently, a controlled excitation of the successive phases is employed to maintain the sustenance of the generated torque.

A detailed exposition of torque generation principle is obtained by analysis the interaction between a pair of excited stator and rotor poles as shown in Fig.(2.1).

The flux linkage magnitude as a specific instant is calculated as a function of instantaneous magnetic characteristics as,

$$\psi_{ph}(t) = l_{ph}(\theta_e, i_{ph}) \times i_{ph}(t) = \frac{N_{ph}^2}{\mathscr{R}_l(\theta_e, i_{ph})} \times i_{ph}(t) = N_{ph} \times \frac{\text{MMF}(t)}{\mathscr{R}_l(\theta_e, i_{ph})} = N_{ph}\phi_{ph}(t) \tag{2.1}$$

By definition, the magnetic reluctance ($\mathscr{R}_l(\theta_e, i_{ph})$) represents opposition offered to the magnetic flux ($\phi_{ph}(t)$) in the magnetic circuit and it is calculated as following.

$$\mathscr{R}_l(\theta_e, i_{ph}) = \left(\frac{1}{\mu_0\mu_r}\right)\frac{2g_{ip}(i_{ph})}{A_{ov}(\theta_e)} \tag{2.2}$$

Evidently from Eq.(2.2), the reluctance of the magnetic circuit is inversely proportional to the area of overlap between the stator and rotor poles whereas, the current dependence of the air-gap appears from the effect of saturation in the magnetic circuit. This phenomenon is explained in greater detail ahead. For the sake of simplicity, if the fringing flux is considered negligibly small, all the electromagnetic energy conversion can be considered to be confined within the area: $A_p(\theta_e)$. By nature, the flux lines act as stretched rubber bands, exerting torque on the rotor in a process of attaining the least reluctance path. As the rotor attains alignment with the stator pole, the overlap area $A_{ov}(\theta_e)$ grows, thus reducing the magnitude of the reluctance as described in Eq.(2.2). For a fixed value of phase current, the magnitude of flux linkage $\psi_{ph}(t)$ is largest for least reluctance position: θ_{eu}.

Electromagnetic Energy Interaction

For a constant magnitude of phase current, the electrical energy supplied to the magnetic circuit is calculated as,

$$W_{elect}(t) = \int_0^t V_{dc} i_{ph} dt \tag{2.3}$$

The supplied electrical energy described by Eq.(2.3) in part gets stored in the magnetic circuit known as, field energy while the remaining gets transformed into useful mechanical energy as described in the following equation [Krishnan (2017)].

$$W_{elect}(t) = W_{field}(t) + W_{mech}(t) \tag{2.4}$$

The stored magnetic energy produces magnetic magnetic field in the airgap between the stator and rotor poles. Higher magnitude of magnetic filed also implies higher magnitude of $\phi_{ph}(t)$. This relation is expressed as following.

$$W_{field}(t) = \frac{1}{2} \frac{\phi_{ph}^2(t)}{\mathscr{R}_l(\theta_e, i_{ph})} \tag{2.5}$$

For a stationary rotor ($\omega_m = 0$) in a position shown in the Fig.(2.1), no mechanical work is done, thus all the supplied electrical energy is stored in the field. A graphical representation of this condition in terms of electro-mechanical energies is shown in Fig.(2.2). For $\omega_m > 0$, mechanical work is produced at the expense of both electrical and field energies. The contribution of each is determined by the operating speed. For two different operating speeds viz, ω_{m1} and ω_{m2}, the process of mechanical energy generation is depicted in Fig.(2.3). As evident from Eq.(2.1), the magnitude of flux

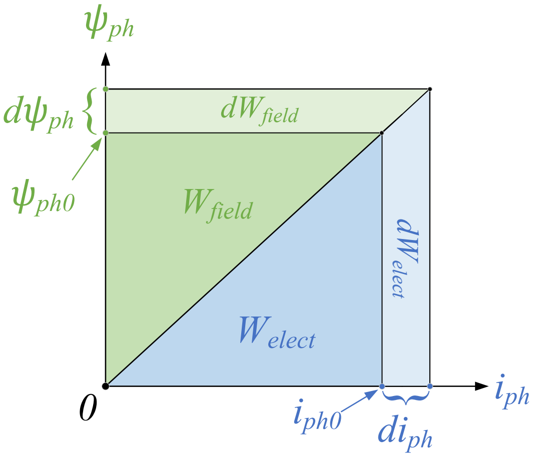

Figure 2.2: Field energy

linkage for a constant value of $i_{ph} = i_{ph1}$ is highest for $\theta_e = \theta_{eu}$ designated by the point B and corresponding maximum value of flux linkage $= \psi_{ph4}$. For $\theta_e = \theta_{eu}$, the flux-linkage versus phase current characteristics is represented by the curve, $O - A' - B$. The curved nature of the this characteristics is a consequence of saturation in the magnetic circuit. Under saturation, the apparent reluctance is larger as compared to that in unsaturated condition. This increase in the reluctance at saturated condition is often modelled in the form of the widened air-gap: $g_{ip}(i_{ph})$.

For sufficiently small θ_e $(< \theta_{eu})$, The flux-linkage versus current characteristics is represented by the curve: $O - A$ with maximum value of flux-linkage: ψ_{ph1}. For a constant value of $i_{ph} = i_{ph1}$, as the rotor electrical position approaches θ_{eu}, the flux linkage magnitude changes from, ψ_{ph1} to ψ_{ph3}. It is important to note here that the path taken by the magnetisation characteristics between points, A and B depends upon the operating speed. During this this process, the supplied electrical energy is calculated as,

$$W_{elect} = i_{ph1}(\psi_{ph3} - \psi_{ph1}) = area(ABCDA) \tag{2.6}$$

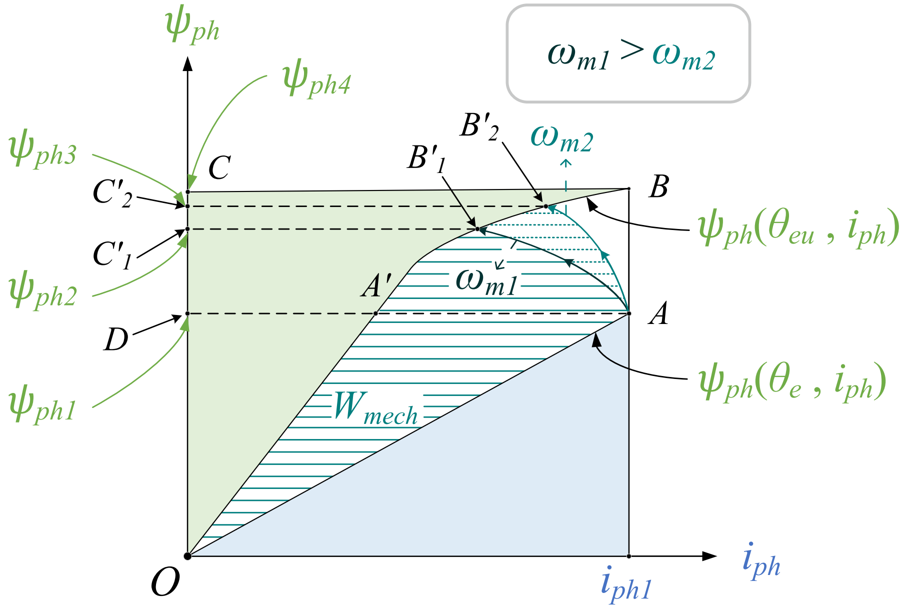

Figure 2.3: Electro-mechanical energy conversion

The magnitude of the filed energy from at position A is represented by $area(OADO)$ whereas $OABA'O$ represents the magnitude of field energy at position B. For $\omega_m = \omega_{m1}$ The change in the magnetisation characteristics follows the curve: $A - B'$. Thus, $area(OAB_1'A'O)$ represents the mechanical work done during the displacement of the rotor until $\theta_e = \theta_{eu}$. This mechanical work is performed partially at the expense of the filed energy:$area(OAA'O)$ while the rest is supplied by electrical energy:$AB_1'A'A$.

Similarly, for $\omega_m = \omega_{m2}$, the mechanical work done is obtained as: $area(OAB_2'A'O)$. During this process, the expended electrical energy is: $area(AB_2'A'O)$ while the supplied field energy is represented by: $area(OAA'O)$. If the rotor remains stationary at position $\theta_e = \theta_{eu}$, the electrical energy begins to store in the field, following the curves, $B_1' - B_2' - B$ for $\omega_m = \omega_{m1}$ and $B_2' - B$ for $\omega_m = \omega_{m2}$.

From above discussion, it is clear that the contribution of electrical energy towards mechanical work diminishes as the rotor speed increase. The primary cause of this phenomenon is the 'magnetic inertia' of the circuit know as inductance. This effect becomes more prominent as the speed of the rotor increases.

Electromagnetic Torque

In an SRM, the electromagnetic characteristics are governed by the following equation.

$$v_{ph}(t) = r_{ph} i_{ph}(t) + \frac{d\psi_{ph}(\theta_e, i_{ph})}{dt} \tag{2.7}$$

By substitution of Eq.(2.1) in Eq.(2.7), a distinction between field energy and mechanical energy components is obtained as,

$$v_{ph}(t) = r_{ph} i_{ph}(t) + l_{ph}(\theta_e, i_{ph}) \frac{di_{ph}(t)}{dt} + i_{ph}(t) \frac{dl_{ph}(\theta_e, i_{ph})}{dt}$$

$$\Rightarrow v_{ph}(t) = r_{ph} i_{ph}(t) + l_{ph}(\theta_e, i_{ph}) \frac{di_{ph}(t)}{dt} + i_{ph}(t) \frac{dl_{ph}(\theta_e, i_{ph})}{d\theta_e} \omega_m \tag{2.8}$$

The rate of accumulation of the field energy in the magnetic circuit as a result of supplied electrical energy, is obtained by reorienting Eq.(2.7) and multiplying both sides by $i_{ph}(t)$ as shown below [Bimbhra (2010)].

$$v_{ph}(t) i_{ph}(t) - r_{ph} i_{ph}^2(t) = i_{ph}(t) l_{ph}(\theta_e, i_{ph}) \frac{di_{ph}(t)}{dt} + i_{ph}^2(t) \frac{dl_{ph}(\theta_e, i_{ph})}{d\theta_e} \omega_m$$

$$\Rightarrow d(W_{elect} - W_{cu}) = dW_{field} + dW_{mech} \tag{2.9}$$

From Eq.(2.9), the components of the mechanical power can be identified as: $dW_{mech} = T_e\omega_m$ yielding the following torque expression.

$$T_e = i_{ph}^2(t)\frac{dl_{ph}(\theta_e, i_{ph})}{d\theta_e} \tag{2.10}$$

For SRM geometries with more than one pair of stator poles per phase as apposed to the one depicted in Fig.(2.1), the relation between the rotor electrical and mechanical speeds is defined as,

$$\omega_e = N_r\omega_m \tag{2.11}$$

Where, N_r represents the number of rotor poles. Thus, total mechanical power becomes:

$$dW_{mech} = i_{ph}^2(t)\frac{dl_{ph}(\theta_e, i_{ph})}{d\theta_e}\omega_e = i_{ph}^2(t)N_r\frac{dl_{ph}(\theta_e, i_{ph})}{d\theta_e}\omega_m \tag{2.12}$$

Torque in Motoring and Generating Modes

For a positive value of ω_e, the sign of the electromagnetic torque determines whether the SRM is being operated in motoring or generating mode. The most straightforward approach in determining this requires the knowledge of inductance slope. According to the discussion provided in the beginning of this section, Eq.(2.10) can be expanded as below,

$$T_e = i_{ph}^2(t)\frac{dl_{ph}(\theta_e, i_{ph})}{d\theta_e} = i_{ph}^2(t)\frac{d}{d\theta_e}\left(\frac{N_{ph}^2}{\mathscr{R}_l(\theta_e, i_{ph})}\right) \tag{2.13}$$

By substituting Eq.(2.2) in Eq.(2.13). The torque equation appears as a function of geometric parameters as,

$$T_e = i_{ph}^2(t)\frac{d}{d\theta_e}\left(\frac{\mu_0\mu_r N_{ph}^2}{2g_{ip}(i_{ph})}A_{ov}(\theta_e)\right) = \frac{\mu_0\mu_r N_{ph}^2 i_{ph}^2(t)}{2g_{ip}(i_{ph})}\frac{dA_{ov}(\theta_e)}{d\theta_e} \tag{2.14}$$

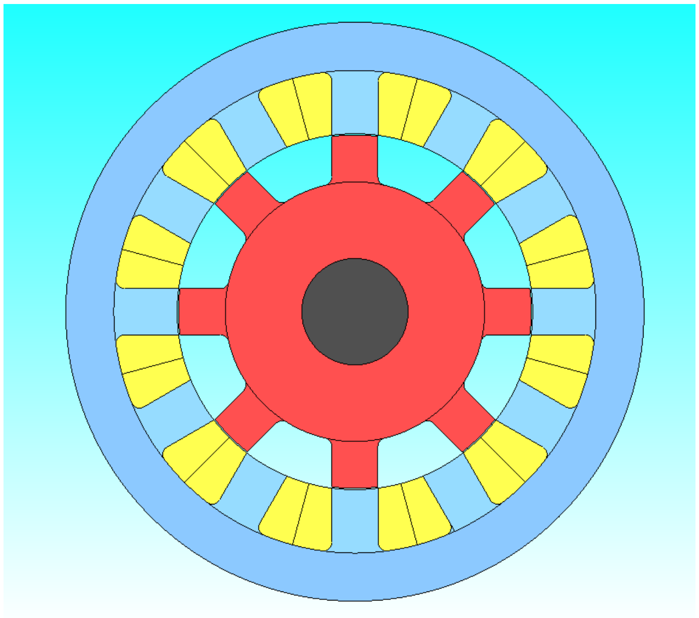

Figure 2.4: Geometry of 12-8 switched reluctance machine

Evidently, from Eq.(2.14), the rate of change in overlap area is the primary source of change in the reluctance. By decomposing $A_{ov}(\theta_e)$ into its components: $A_{ov}(\theta_e) = P_w h_{ov}(t) = P_w R_l \theta_e(t)$, the torque equation becomes,

$$T_e = \frac{\mu_0 \mu_r N_{ph}^2 i_{ph}^2(t)}{2 g_{ip}(i_{ph})} \left(P_w R_l\right) \tag{2.15}$$

Static Characterisation

The evaluation of control principles developed in this thesis is performed over a 3-phase, 1kW 100V 12-8 (12 Stator poles - 8 Rotor poles) SRM drive. The geometry of this machine is shown in Fig.(2.4). The electromagnetic characteristics of the SRM are identified via Finite Element Analysis (FEA). For this purpose, a static characterisation simulation is performed in JMAG$^{®}$ Designer [JMA (2018)]. The static characterisation is performed for a constant speed of 1000RPM and incremental

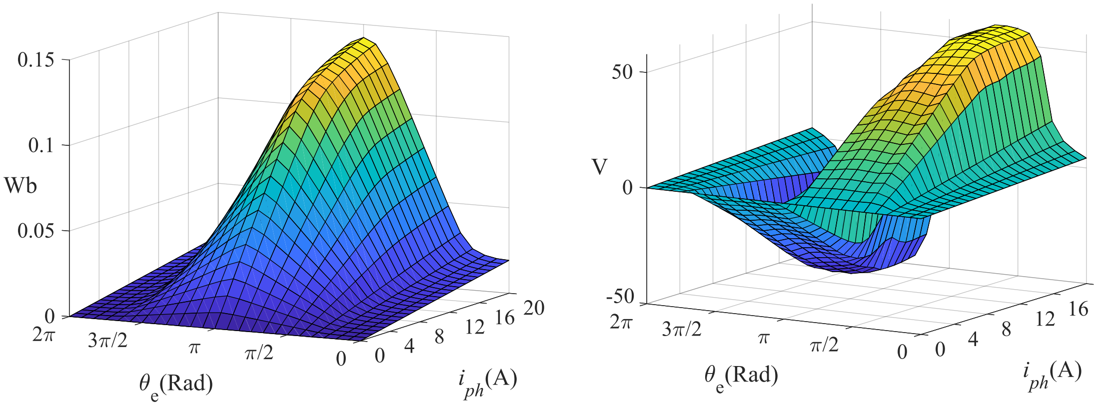

(*a*) flux-linkage characteristics

(*b*) induced EMF characteristics (ω_m = 104.72 rad/sec)

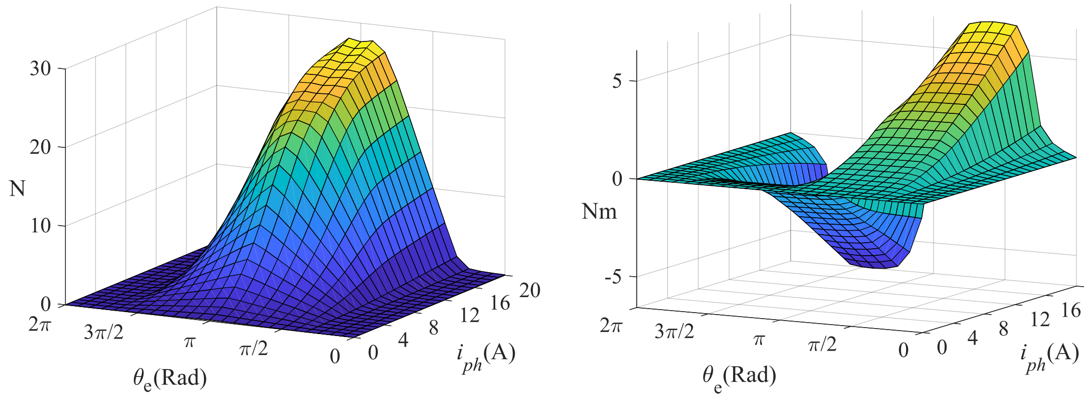

(*c*) Radial force characteristics (*Center of the stator pole*)

(*d*) Torque characteristics

Figure 2.5: Static characterisation of 12-8 SRM via FEA

levels of phase currents in the range of 0A to 21A, where 21A represents the peak phase current magnitude.

The output of the static characterisation tests consist of 3-D flux-linkage, torque and induced EMF characteristics to with breakpoints in θ_e and i_{ph}. A 3-D mode-0 radial force characteristics is also obtained at the centre of the stator pole as shown in Fig.(2.5(c)).

2.3 SRM Drive

In SRM, a consistent unidirectional torque is obtained by sequential excitation of the phases as a function of rotor mechanical position. As discussed in the previous section, unidirectional torque can only be maintained if the phases are excited exclusively during either positive or negative slope of their respective inductances. Therefore, the power converter should be capable of sequentially magnetize and de-magnetize each phase independently. For the simulation and experimental studies in this thesis, an asymmetric-bridge power converter is used as shown in Fig.(2.6).

The asymmetric bridge power converter is capable of realising three voltage levels, viz. $+V_{dc}$, $-V_{dc}$ and 0, where the latter is a realised with an additional redundant switching state. These switching states are shown in Fig.(2.7). The states (a) and (d) are implemented to obtain $+V_{dc}$ and $-V_{dc}$ respectively, whereas the stats (c) and (d) are implemented for the realisation of $0V$ at the phase terminals.

A carrier based phase apposition disposition (APOD) PWM scheme is utilised for implementation of a fixed switching frequency operation of the power converter. The phase voltage realisation using this scheme is shown in Fig.(2.8). The $+V_e$ side carrier is responsible for PWM operation on the top switch (S_U) while keeping the

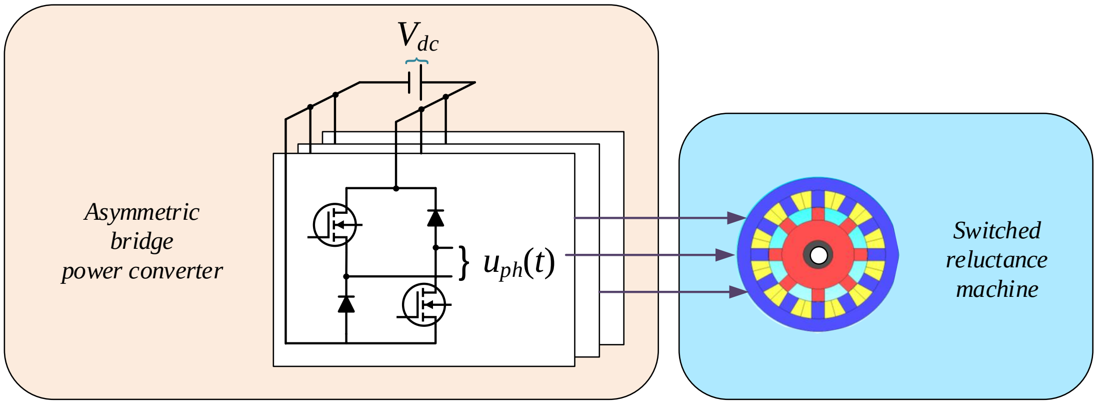

Figure 2.6: Asymmetric bridge power converter fed 3-phase 12/8 SRM drive

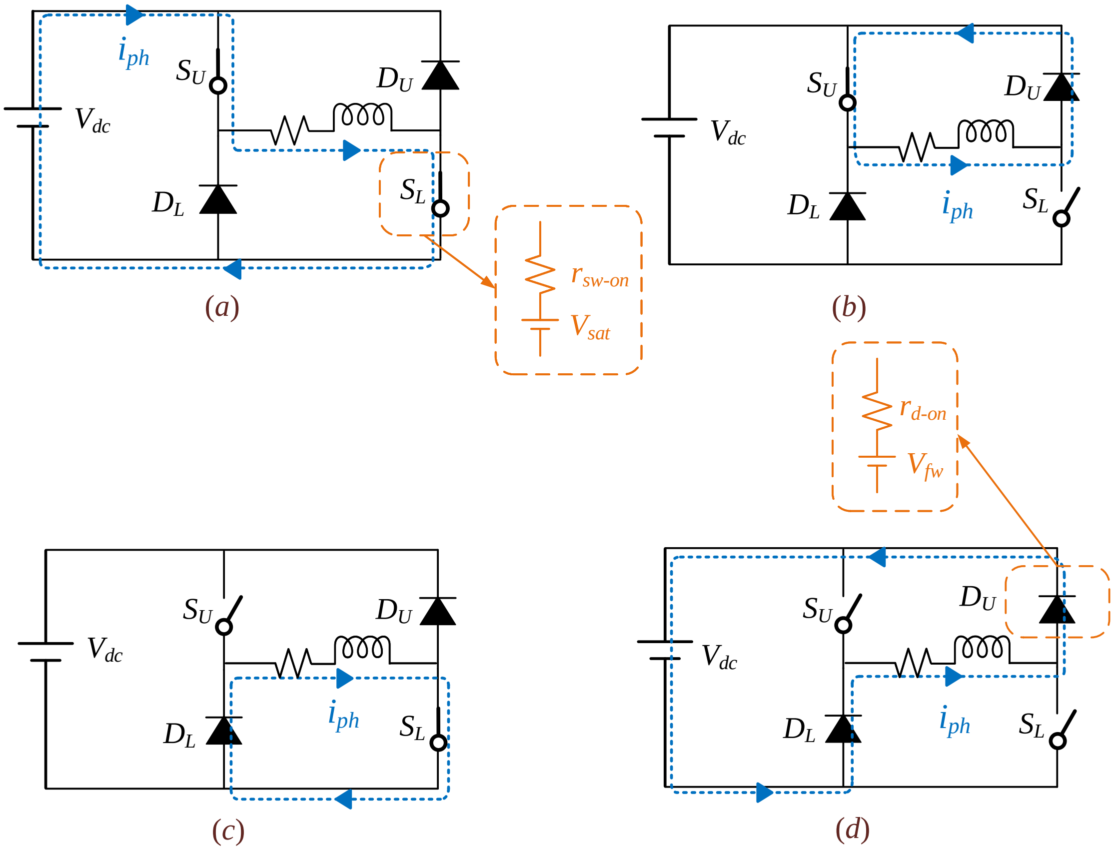

Figure 2.7: Converter switching states

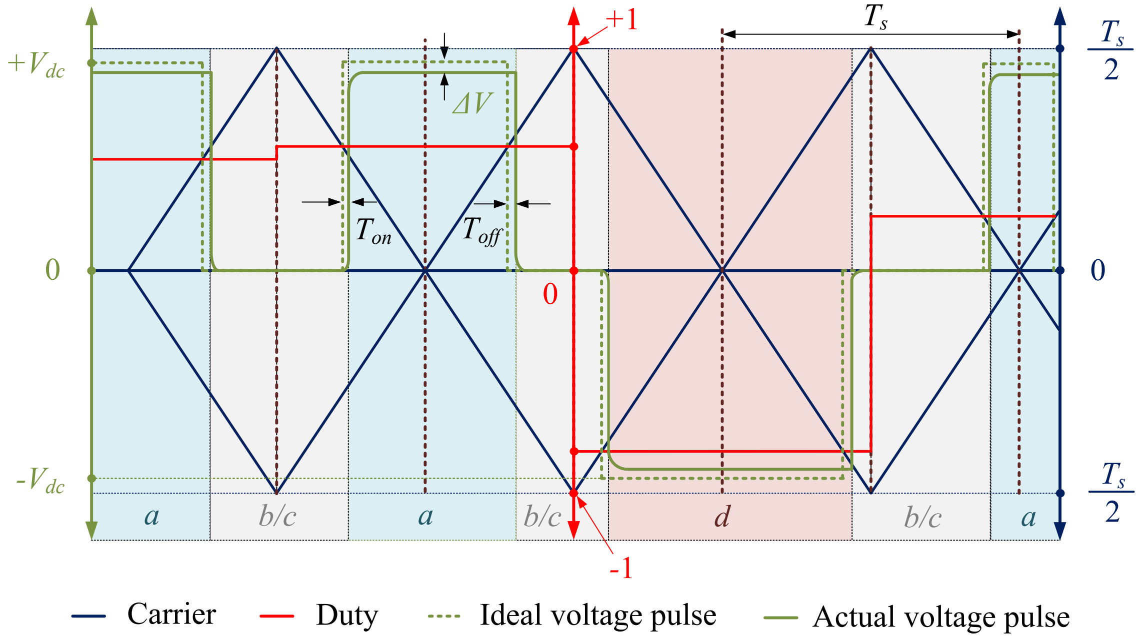

Figure 2.8: PWM implementation process

low side switch (S_L) on. The $-V_e$ side switch is responsible for the PWM operation on the low side switch while keeping the top switch off. It should be noted here, that $-V_{dc}$ is applied across the phase when both the top and bottom side switches are off (state:d). Thus, the applied duty ratio to the bottom side switch is the complement of the real duty ratio. The assignment of the states: a through d using APOD PWM scheme is shown in Fig.(2.8).

In practice, the power electronic switch does not exhibit ideal switching behaviour. The non-ideal behaviour consists of delays during turning-on and turning-off operations as well as the saturation and forward voltage drops in the switches and diodes respectively. During $+V_e$ voltage pulse, this voltage drop is calculated as,

$$\Delta V = V_{sat-U} + V_{sat-L} = 2V_{sat} \tag{2.16}$$

Whereas, during $-Ve$ voltage pulse, this voltage drop is calculated as,

$$\Delta V = V_{fw-U} + V_{fw-L} = 2V_{fw} \tag{2.17}$$

The turn-on (T_{on}) and turn-off (T_{off}) time delays are the functions of the device characteristics used in the power converter.

2.4 Operating Principles of SRM Drives

Following the discussion in the previous sections, a consistent unidirectional torque can be generated through sequential excitation of the phases for either positive or negative slopes of the inductance profiles. In a real world SRM drive, the main challenges arise from the nonlinear variations in this slope. The performance of an SRM drive can be greatly influenced by optimizing this slope through machine design [Jiang *et al.* (2015); Wu *et al.* (2003)] or through control as discussed ahead.

2.4.1 Operation of an Ideal SRM Drive

The principle of unidirectional torque generation in an ideal SRM drive is demonstrated in Fig.(2.9). For a positive direction of rotation represented by increasing magnitude of θ_e, a steady motoring torque is generated by supplying DC currents only during positive inductance slopes. Following Eq.(2.10), the magnitude of electromagnetic torque is obtained as,

$$\begin{aligned} T_{ph} &= K_T i_{ph}^2 \\ \text{Where,} \quad K_T &= \frac{dl_{ph}}{d\theta_e} \end{aligned} \tag{2.18}$$

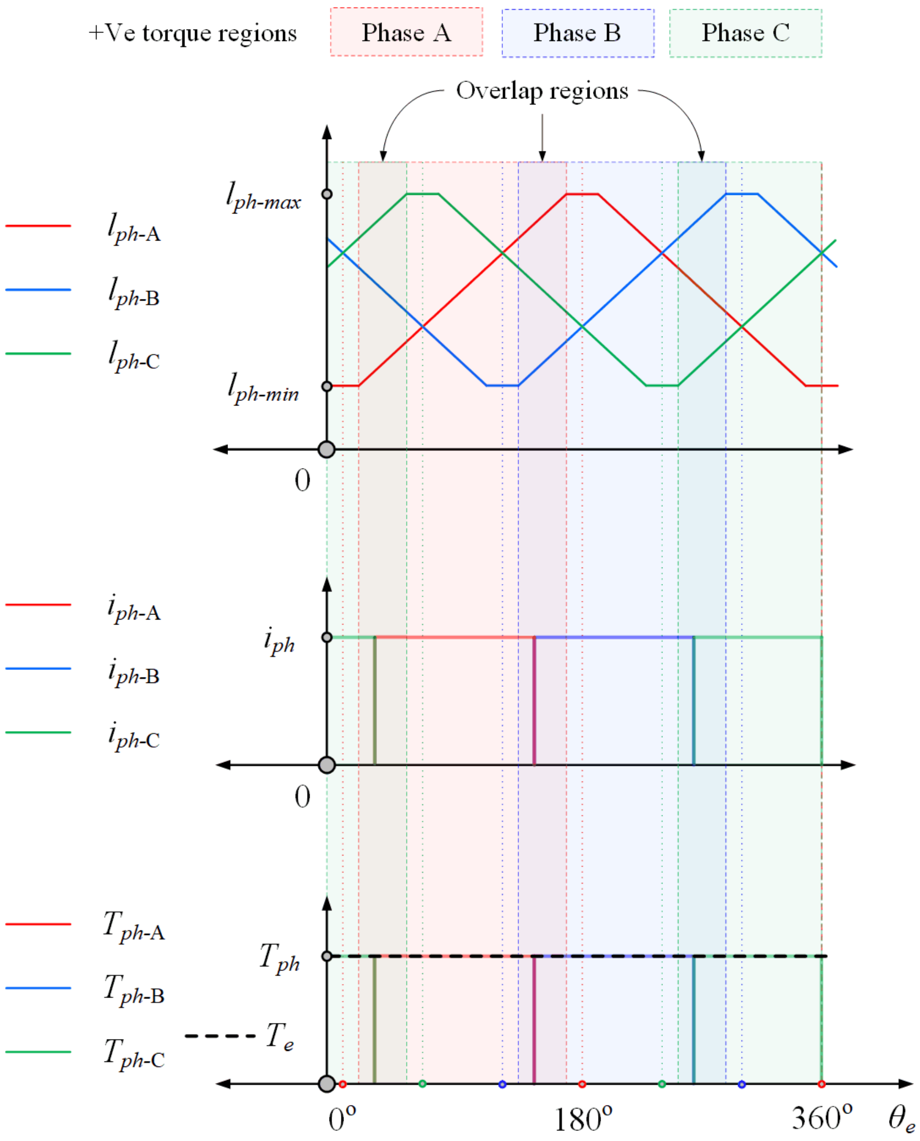

Figure 2.9: Motoring torque generation in an ideal SRM drive

Since the magnitude of $\frac{dl_{ph}}{d\theta_e}$ is constant throughout the conduction period, the torque due to each phase remains constant. This results into generation of steady torque at the shaft which can be sustained by sequencing a controlled application of the currents through phases as shown in Fig.(2.9). This sequential application of the phase currents is performed by controlling the conduction angles (θ_{on} and θ_{off}) for each phase known as conduction period. The values of θ_{on} and θ_{off} define the width the overlap regions. In the overlap region, more than one phases are capable of generating unidirectional torque. Thus, a steady torque at the output shaft can be maintained by performing commutations in these regions.

2.4.2 Operation of a Real SRM Drive

From the discussion in the previous sub-section, it becomes clear that for achieving a constant torque at the shaft, following two conditions are important.

- Constant rate of change of inductance during conduction period
- Smooth transition of phase torque during overlap period

For operation of a practical 3-ph SRM shown in Fig.(2.10), the rate of change of inductance during conduction period is never constant. Moreover, this inductance slope is highly nonlinear for $\theta_e \approx \theta_{on}$ & $\theta_e \approx \theta_{off}$. Due to limited DC-link voltage and considerably large value of inductance near θ_{off}, it is not possible to achieve a steep rate of change in current. Therefore, the commutation characteristics shown in Fig.(2.9) are very difficult to realize. Owing to these reasons, significant torque ripple appears during the phase overlap regions. As shown in Fig.(2.10), large value of torque ripple is also responsible for reducing the average motor torque. This issue

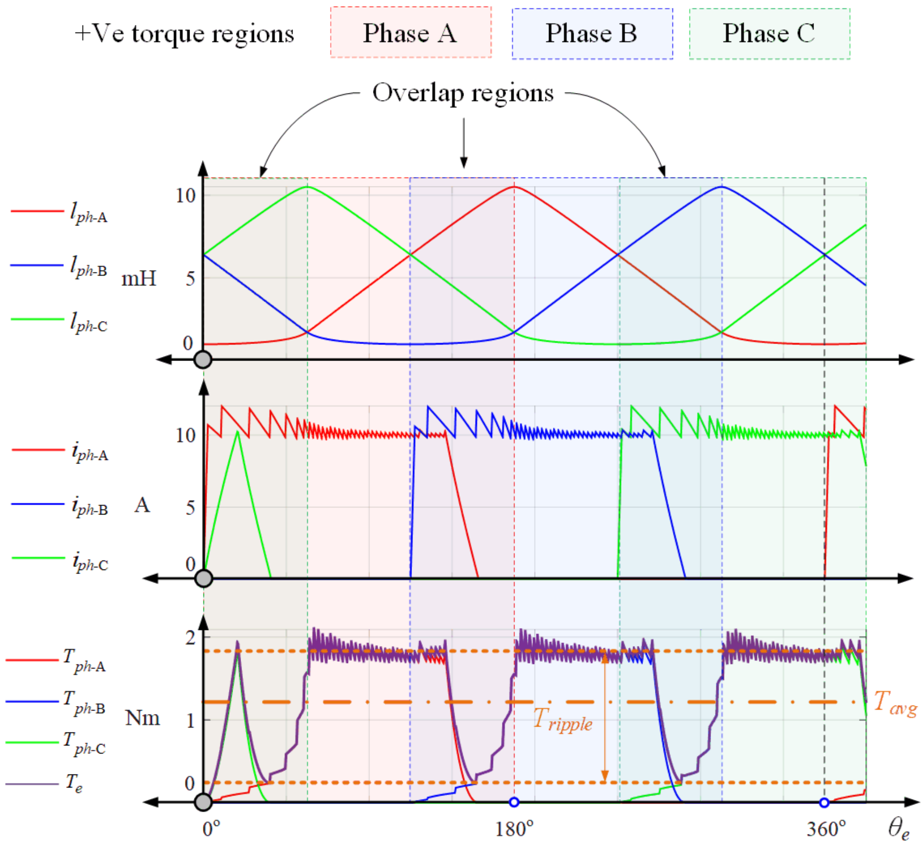

Figure 2.10: Motoring torque generation in a real SRM drive

can be partially resolved by increasing the commutation region for each phase.

2.5 Challenges in Performance Optimization Using Control

Although the optimization of conduction periods for each phase aids to the reduction of torque ripple, it does not fully resolve this issues. Moreover, it also comes with corresponding drawbacks such as aggravation in mode-0 vibrations, copper-loss and reduction in base speed. These phenomena can be explained in greater detail by extending the analysis presented in the previous subsection to include the consequences of widening the conduction periods on mode-0 radial force and DC-link voltage utilization to sustain the necessary current magnitude.

2.5.1 Torque Ripple and Average Torque

Following the process of conduction angle optimization, further reduction in torque ripple is achieved as the turn-off angle (θ_{off}) gets closer to the fully aligned position for rotor and stator poles ($\theta_e = 180^o$). This principle is depicted in Fig.(2.11).

A significant torque ripple is generated for $\theta_{on} = 0^o$ and $\theta_{on} = 160^o$ while it is substantially reduced through further advancement of θ_{off} up to 177^o. Considering finite time required by the phase current to reduce to zero, it is not advisable to further advance the turn-off angle. It is also worth noting here that the advancement in the turn off angle also improves the magnitude of the average torque.

Fig.(2.11) reveals that it is not possible to entirely remove the torque ripple through advancement of the turn-off angle and a significant magnitude of which still

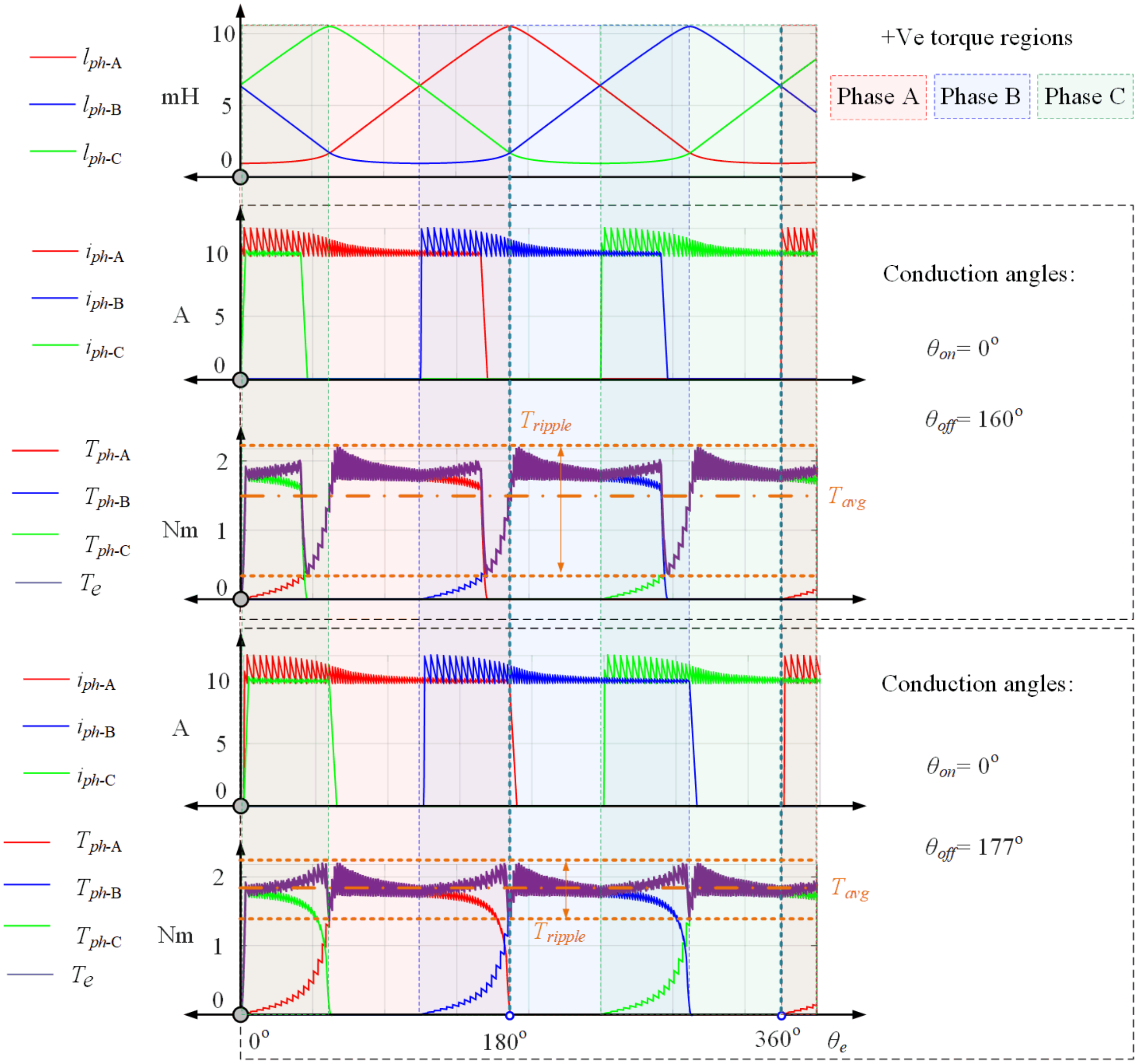

Figure 2.11: Torque ripple minimization through conduction angle control

appears in the $+V_e$ torque overlap region.

2.5.2 Control Limitations Due to Speed

The torque ripple reduction achieved through advancement of θ_{off} in previous subsection is performed at a very low speed of 100RPM. As the operating speed increases, the rate of magnetization/de-magnetization reduces due to increased induced-EMF. Since the magnitude of DC-link voltage is fixed, the ability of the power converter to magnetize/de-magnetize phases reduces. Therefore, larger θ_{off} can not provide desired reduction in torque ripple. This phenomenon is depicted in Fig.(2.12).

2.5.3 Mode-0 Radial Force

The extension of θ_{off} closer to 180^o also results into increased magnitude of the radial force (F_{ph}) at the centre of the stator pole. As shown in Fig.(2.13), extension in θ_{off} by 32^o results in 5N increase in F_{ph}.

The direct consequence of this increase in F_{ph} is aggravation in mode-0 vibrations which is the most Dominant among the vibration modes generated during normal operation of an SRM [Fiedler *et al.* (2006); Hofmann *et al.* (2013)]. The reduction of these vibrations while maintaining the desired torque quality is one of the important challenges to be met for improving the performance of the SRM drives.

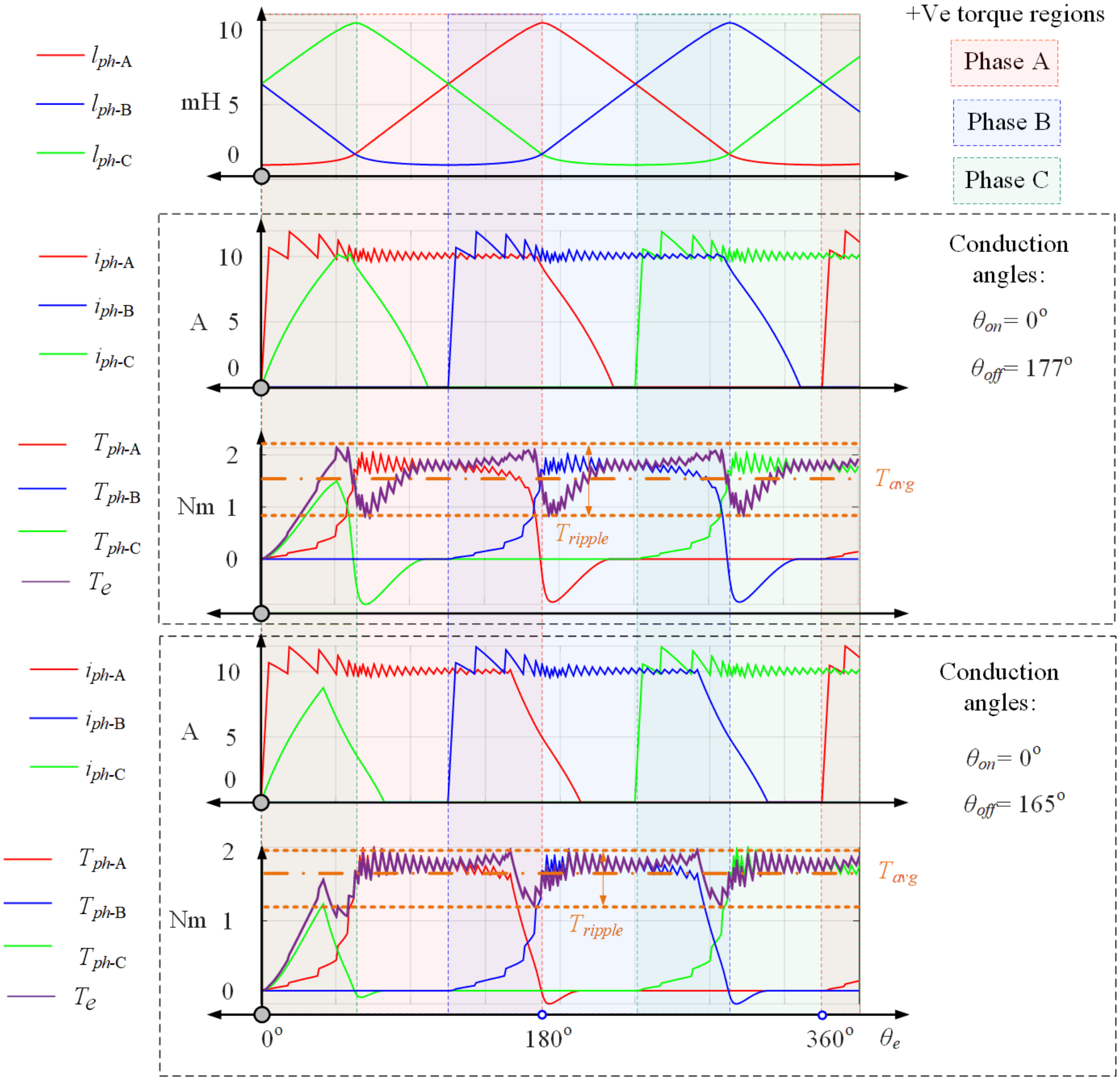

Figure 2.12: Torque control at 1000RPM

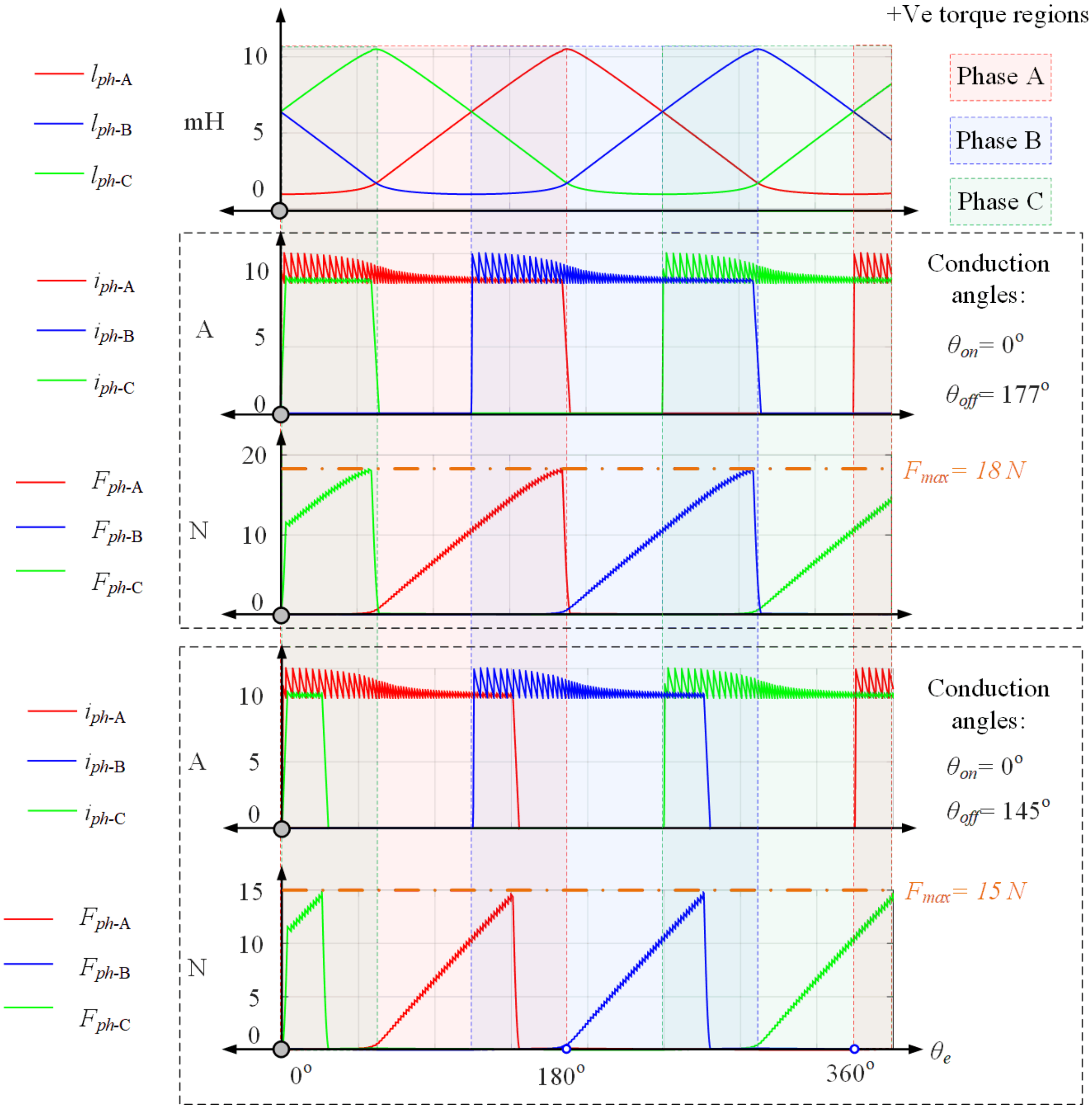

Figure 2.13: Variation in peak Redial force due to the extension of turn-off angle

2.6 Summary

By the virtue of the doubly salient geometry of SRM, the electromagnetic torque is generated as a function of varying phase inductance profile. The primary source of torque ripple is the non-linear variation in phase inductance yielding varying phase torque magnitude as a function of rotor position.

The conventional approach of conduction angle control with fixed magnitude of phase current per conduction period, is capable of reducing the torque ripple by advancing the turn-off angle closer to the fully aligned position. However, this approach is not applicable over a wide speed range and it lead to rise in mode-0 radial vibrations.

Optimizing the width and the instant of the conduction period allows for minimization of copper loss however this relationship is highly non-linear and the fixed nature of the current over a conduction period yields a very limited improvement in performance.

Considering these challenges, the next chapter presents the proposed discrete-time domain framework for efficient torque control of the SRM drives.

Chapter 3

Discrete-Time Domain Framework for Torque Ripple Reduction

3.1 Introduction

This chapter presents a discrete-time domain torque control framework addressing the challenges discussed in the previous chapter.

The next Section 3.2 provides a detailed exposition of the torque control problem, corresponding challenges, and the avenues for achieving the objectives outlined in the previous chapter. The subsequent Section 3.3 introduces the optimization problem for identification of optimum current references for achieving the secondary objectives. This section also defines the constraints and the approach which will be followed in the rest of this thesis.

The discrete-time domain characteristics of SRM electromagnetic model are presented in section 3.4. Using these characteristics a performance evaluation criteria is developed for comparative analysis of the digital current control techniques.

3.2 Torque Control Problem and its Dynamics

The nonlinear SRM dynamics with the torque as an output is represented as following,

$$\begin{bmatrix} \dot{i}_{ph-A}(t) \\ \dot{i}_{ph-B}(t) \\ \dot{i}_{ph-C}(t) \end{bmatrix} = A_{tc} \begin{bmatrix} i_{ph-A}(t) \\ i_{ph-B}(t) \\ i_{ph-C}(t) \end{bmatrix} + B_{tc} \begin{bmatrix} u_{ph-A}(t) \\ u_{ph-B}(t) \\ u_{ph-C}(t) \end{bmatrix} \tag{3.1a}$$

$$T_e = C_{tc} \begin{bmatrix} i^2_{ph-A}(t) \\ i^2_{ph-B}(t) \\ i^2_{ph-C}(t) \end{bmatrix} \tag{3.1b}$$

Where the matrices A_{tc}, B_{tc} and C_{tc} are defined as,

$$A_{tc} = \begin{bmatrix} -\left(\frac{r_{ph}}{l_{ph-A}} + \frac{dl_{ph-A}}{d\theta_e}\omega_e\right) & 0 & 0 \\ 0 & -\left(\frac{r_{ph}}{l_{ph-B}} + \frac{dl_{ph-A}}{d\theta_e}\omega_e\right) & 0 \\ 0 & 0 & -\left(\frac{r_{ph}}{l_{ph-B}} + \frac{dl_{ph-A}}{d\theta_e}\omega_e\right) \end{bmatrix}$$

$$B_{tc} = \begin{bmatrix} \frac{1}{l_{ph-A}} & 0 & 0 \\ 0 & \frac{1}{l_{ph-B}} & 0 \\ 0 & 0 & \frac{1}{l_{ph-C}} \end{bmatrix}$$

and

$$C_{tc} = \begin{bmatrix} \frac{dl_{ph-A}}{d\theta_e} & \frac{dl_{ph-B}}{d\theta_e} & \frac{dl_{ph-C}}{d\theta_e} \end{bmatrix}$$

The phase current dynamics described in Eq.(3.1) can be regarded as a 'Linear Time-Varying'(LTV) system. Considering highly nonlinear nature of the torque equation, a generalised version of the torque dynamics are represented as,

$$\begin{aligned} \dot{I_{ph}}(t) &= F(P_{ph}, I_{ph}) + L_{inv}U_{ph}(t) \\ T_e &= H(p_{ph}, I_{ph}) \end{aligned} \tag{3.3}$$

Where, the current, voltage, and the parameter vectors are defined as,

$$I_{ph} = \begin{bmatrix} i_{ph-A} & i_{ph-B} & i_{ph-C} \end{bmatrix}^T$$

$$U_{ph} = \begin{bmatrix} u_{ph-A} & u_{ph-B} & u_{ph-C} \end{bmatrix}^T$$

$$P_{ph} = \begin{bmatrix} \left(\frac{r_{ph}}{l_{ph-A}} + \frac{dl_{ph-A}}{d\theta_e}\omega_e\right) & \left(\frac{r_{ph}}{l_{ph-B}} + \frac{dl_{ph-B}}{d\theta_e}\omega_e\right) & \left(\frac{r_{ph}}{l_{ph-C}} + \frac{dl_{ph-C}}{d\theta_e}\omega_e\right) \end{bmatrix}^T$$

$$L_{inv} = \begin{bmatrix} \frac{1}{l_{ph-A}} & \frac{1}{l_{ph-B}} & \frac{1}{l_{ph-C}} \end{bmatrix}^T$$

$$L_{ph} = \begin{bmatrix} l_{ph-A}, l_{ph-B}, l_{ph-C} \end{bmatrix}$$

Following Eq.(3.3), a further simplification of the torque dynamics are obtained as,

$$\begin{aligned} \dot{T_e} &= \frac{\partial H}{\partial I_{ph}}\dot{I_{ph}}(t) = \frac{\partial H}{\partial I_{ph}}(F(P_{ph}, I_{ph}) + L_{inv}U_{ph}(t)) \\ &\implies \dot{T_e} = \mathcal{L}_F H + \mathcal{L}_G H U_{ph}(t) \end{aligned} \tag{3.4}$$

In Eq.(3.4), the function: $\mathcal{L}$ represents the 'Lie operator'. The necessary conditions for the objective of torque ripple minimization can be defined through the following equation of the desired torque dynamics.

$$\dot{T}_e = -\Lambda T_e + \Lambda T_{ref} \tag{3.5}$$

Where, T_{ref} denotes the steady state value of the reference torque, and Λ represents desired bandwidth. Using substitution from Eq.(3.4) in Eq.(3.5), and $T_e = H(p_{ph}, I_{ph})$, the desired torque dynamic equation can be expanded as,

$$\Lambda T_{ref} = \Lambda H + \mathcal{L}_F H + \mathcal{L}_G H U_{ph} \tag{3.6}$$

In theory, any combination of the control vector U_{ph} satisfying Eq.(3.6) is capable of keeping the torque ripple to zero. Therefore, the family of such control inputs is defined as,

$$\mathbf{U}_{ph} = \{U_{ph} : U_{ph} - (\mathcal{L}_G H)^{-1}(\Lambda T_{ref} - \Lambda H - \mathcal{L}_F H) = 0\} \tag{3.7}$$

3.3 Secondary Objectives and Torque Contributions

In the view of the analysis presented so far, it is possible to achieve Eq.(3.6) using any control input satisfying Eq.(3.7). In an SRM drive operated below rated condition, i.e. $T_{ref} < T_{rated}$ an operating point can be achieved by multiple combinations of input voltage. i.e. $n(\mathbf{U}_{ph}) > 1$. Therefore, it is possible to further optimize the torque control performance by addressing the secondary objectives.

The secondary objectives: copper loss minimization and mode-0 radial force reduction are defined in the form of optimization problems. In these problems, Eq.(3.7) represents equality constraint while the inequality constraints are defined in the form of phase current limits. Since U_{ph} is the optimization variable, the phase current limits are expressed in the form of limit on flux linkage as,

$$\psi_{ph-max}(\theta_e) = i_{max} l_{ph}(\theta_e, i_{ph-max}) \tag{3.8}$$

Neglecting the resistance and power converter voltage drops, the approximate relation between the phase flux linkage and control voltage input is obtained,

$$\int_0^t u_{ph}(t)dt \approx \psi_{ph}(t) \tag{3.9}$$

Consequently, the flux linkage vector is defined as,

$$\Psi_{ph}(\theta_e, I_{ph}) = \begin{bmatrix} \psi_{ph-A}(\theta_{e-A}, i_{ph-A}) & \psi_{ph-B}(\theta_{e-B}, i_{ph-B}) & \psi_{ph-C}(\theta_{e-C}, i_{ph-C}) \end{bmatrix} \tag{3.10}$$

Using Eq.(3.8) and Eq.(3.9) the optimization problems for satisfying the secondary objectives are defined as,

Copper loss minimization

$$\min_{U_{ph}} \quad I_{ph}^T I_{ph} \tag{3.11a}$$

$$\text{subject to} \quad (\mathcal{L}_G H)^{-1}(\Lambda T_{ref} - \Lambda H - \mathcal{L}_F H) - U_{ph} = 0, \tag{3.11b}$$

$$0 \leq \int_0^t U_{ph}(t)dt \leq \Psi_{max}(\theta_e, I_{ph}) \tag{3.11c}$$

Copper loss and radial force minimization

$$\min_{U_{ph}} \quad I_{ph}^T I_{ph} + W_w \|F_r\| \tag{3.12a}$$

$$\text{subject to} \quad (\mathcal{L}_G H)^{-1}(\Lambda T_{ref} - \Lambda H - \mathcal{L}_F H) - U_{ph} = 0, \tag{3.12b}$$

$$0 \leq \int_0^t U_{ph}(t)dt \leq \Psi_{max}(\theta_e, I_{ph}) \tag{3.12c}$$

In Eq.(3.11) and Eq.(3.12), the objective of torque ripple reduction is embedded in the equality constraint on U_{ph} while the secondary objectives appear as main optimization targets. in case of dual-objective optimization, a weighing constant W_w is used to priorities between the conflicting objectives of copper loss and radial force reduction.

In literature, there are several approaches taken to identify the solution for the optimization problem discussed above. Among the online solution methods, the two most popular approaches are, ‘Online Torque Sharing Functions’ (OLTSFs) and ‘Predictive PWM Control’. These two approaches are mentioned here, due to their suitability for fixed switching frequency control and ability to respond dynamic variations in torque reference.

As seen from the static characterization maps in Fig.(2.5), the electromagnetic characteristics of SRM are mostly represented as 2-D functions with highly nonlinear behaviour. Highly complicated algebraic equations are required to model the nonlinear electromagnetic characteristics of SRM to attain sufficient accuracy. Evidently from Eq.(3.12) and Eq.(3.11), it also very difficult to manage the constraints with U_{ph} as an optimization variable. These issues are the genesis of the investigation into further simplification of the torque control problem yielding the torque control methods discussed in Chapter 1.

The different combinations of the input vector U_{ph} dictate possible combinations of the torque contributions from the phases. The advantage of switching the optimization variable from input voltage to torque is the simplification in the constraints (Eq.(3.11b), and Eq.(3.12b)). On the other hand, the output of the optimization process is a torque vector which is required to be converter into an appropriate control voltage signal. This stage is significantly complected when implemented under a fixed switching frequency framework and it is addressed in the subsequent chapters in greater detail.

When torque is considered as optimization variable, the original problems in Eq.(3.11) and Eq.(3.12) are simplified to the following form.

Copper loss minimization

$$\min_{T_{ph}} \quad I_{ph}^T I_{ph} \tag{3.13a}$$

$$\text{subject to} \quad |T_{ph}| - T_e = 0, \tag{3.13b}$$

$$0 \leq \|T_{ph}(\theta_e)\|_\infty \leq T_{max}(\theta_e) \tag{3.13c}$$

copper loss and radial force minimization

$$\min_{T_{ph}} \quad I_{ph}^T I_{ph} + W_w \|F_e\| \tag{3.14a}$$

$$\text{subject to} \quad |T_{ph}| - T_e = 0, \tag{3.14b}$$

$$0 \leq \|T_{ph}(\theta_e)\|_\infty \leq T_{max}(\theta_e) \tag{3.14c}$$

The inequality constraint in Eq.(3.13) and Eq.(3.14) are realised through the limit on torque as a function of rotor position as,

$$T_{max}(\theta_e) = \begin{bmatrix} T_{ph}(\theta_{e-A}, i_{ph-max}) & T_{ph}(\theta_{e-B}, i_{ph-max}) & T_{ph}(\theta_{e-C}, i_{ph-max}) \end{bmatrix}^T \tag{3.15}$$

The optimal torque vector thus obtained from the solution of the above optimization is converted into the reference current vector through the torque-current characteristics as,

$$I_{ref} = \mathcal{F}_{T-I}(\theta_e, T_{ph}) \tag{3.16}$$

Through Eq.(3.16), the torque control problem is reduced to a simpler current control problem. In the view of this advantages, this thesis approaches the primary and secondary torque control objectives by splitting it into two steps as mentioned below.

1 Online identification of the optimum current references satisfying the primary and secondary objectives

2 Current reference tracking control

The first step involves the identification of solution to the optimization problems Eq.(3.13) and Eq.(3.14), while the second step consists of accurate tracking of these reference. Considering the need of fixed switching frequency modulation, the proposed torque control mechanism discussed in the rest of this thesis is depicted in Fig.(3.1).

3.4 Current Control

A good estimate of the model dynamics and corresponding disturbances is essential while implementing a fixed switching frequency based current control. By principle, the electromagnetic model of SRM is a highly nonlinear dynamical system. The

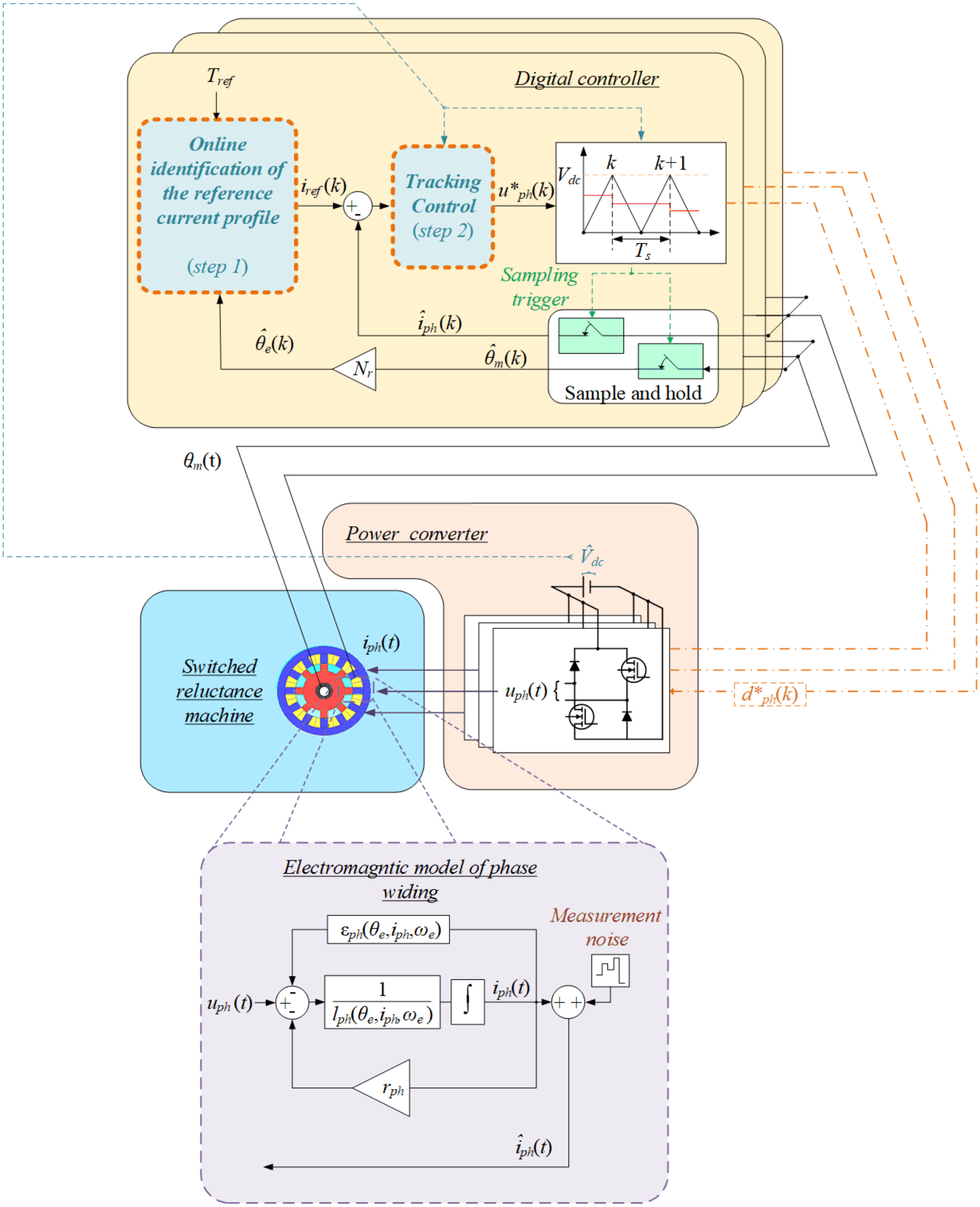

Figure 3.1: Proposed discrete-time domain framework for torque control

nonlinear variation in inductance profile over conduction period results into nonlinear flux linkage, torque, radial force, and induced EMF characteristics. Consequently, the output of the nonlinear optimization process described in the previous section exhibit large dynamic variations in the reference currents demanding high dynamic response and effective disturbance rejection performance from the controller.

The consequences of variation in the dynamic response due to change in operating conditions and corresponding controller response under fixed sampling frequency is a critical aspect which needs a through analysis to quantify and predict, the phase current dynamics for different operating conditions as well as to enable the identification the possible avenues for further enhancement in the control performance.

In the light of the above discussion, rest of this chapter presents a set of evaluation criteria developed on the account of the distinctive electromagnetic characteristics of SRM and from the perspective of the control hardware limitations.

3.4.1 The Control Performance Evaluation Criterion

The current reference profiles optimised for achieving improved performance in SRM drives consist of sharp variations as a function of rotor electrical position [Xue *et al.* (2009)]. Consequently, these variations get further sped up as mechanical speed increases. Typically for most of the applications, the sampling and switching frequencies are kept constant devoid of the variations in operating speed. Therefore, number of sampling and switching instances per conduction period reduce as the speed increases.

The matched disturbance in the form of induced EMF also grows proportionally with respect to the speed. Although smooth, the induced EMF characteristics is also highly nonlinear which becomes increasingly challenging to reject due to reduced

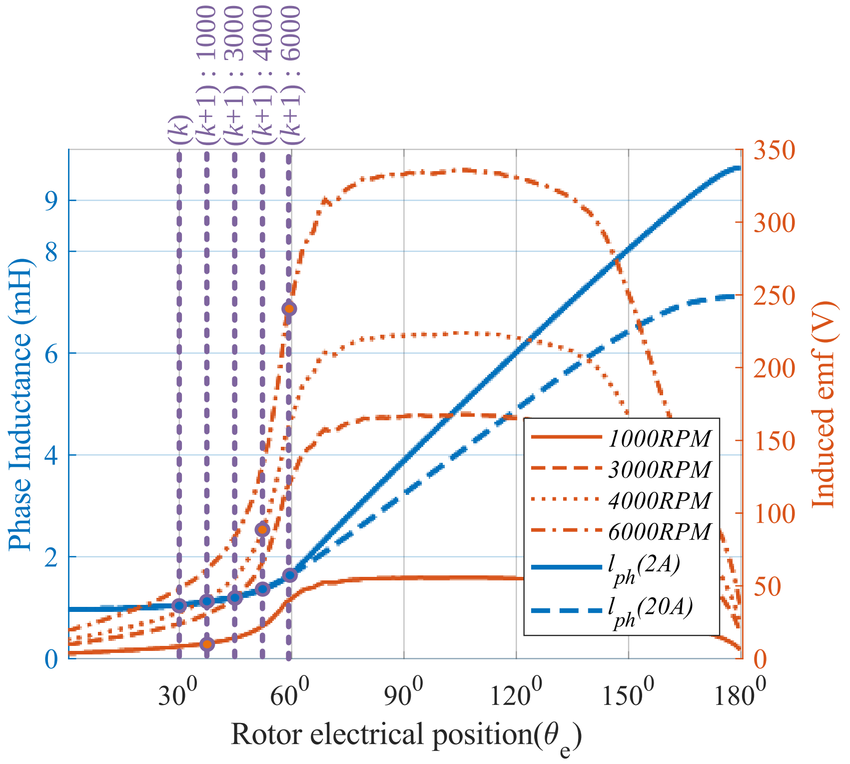

Figure 3.2: Inductance and induced EMF characteristics of a 12-8 SRM for different operating speeds and sampling span at 10kHz frequency

sampling frequency at higher speeds as the bandwidth of the controller gets severely limited. The first order representation of electromagnetic characteristics leads to a linear time varying plant, where the time varying nature comes due to the variation in the inductance profile as a function of rotor position. This variation often results into increasingly slower current dynamics in motoring mode and increasingly faster current dynamics in generating mode. Hence, it becomes necessary to adapt the control efforts over conduction period to maintain a consistent dynamic response. Intuitively, this effect also gets exacerbated for higher operating speed. The above mentioned phenomena are demonstrated ahead with greater clarity by analysing the model dynamics in discrete-time domain.

Discrete-Time Domain Dynamics of SRM Phase Current Model

As shown in Fig.(3.2), the continuous-time domain current dynamics of SRM can be modelled in the form of a first-order nonlinear dynamical system as,

$$\dot{i_{ph}}(t) = \frac{-\hat{r}_{ph}}{\hat{l}_{ph}(\theta_e, i_{ph})} i_{ph}(t) + \frac{1}{\hat{l}_{ph}(\theta_e, i_{ph})} u^*_{ph}(t) \\ - \frac{1}{\hat{l}_{ph}(\theta_e, i_{ph})} \hat{\epsilon}_{ph}(\theta_e, i_{ph}, \omega_e) - \zeta(t) \quad (3.17)$$

The mismatched disturbance $\zeta(t)$ in (3.17) mainly consists of power converter non-linearities, parameter information error, and current measurement noise. The former acts as a discriminant between the voltage commanded by the controller and the phase terminal voltage. Due to the unidirectional nature of the phase current in SRM, the disturbance due to the power converter non-linearities appears as a constant voltage drop [Choi and Sul (1996)] and pose no adverse effect on the controller dynamic response. Considering this, the effect of inverter generated disturbance is not considered in the analysis. Accordingly, the controller output voltage is treated to be same as the phase voltage $\left(u^*_{ph}(t) \approx u_{ph}(t)\right)$ and the dynamics of the mismatched disturbance appears only as a lumped sum of the disturbances due to errors in the knowledge of parameters and induced EMF as well as the measurement noise.

For the analysis presented ahead in this chapter, the errors in inductance, resistance, and induced EMF profile are respectively defined as following,

$$\tilde{l}_{ph} = l_{ph}(\theta_e, i_{ph}) - \hat{l}_{ph}(\theta_e, i_{ph})$$

$$\tilde{r}_{ph} = r_{ph} - \hat{r}_{ph}$$

$$\tilde{\epsilon}_{ph} = \epsilon_{ph}(\theta_e, i_{ph}) - \hat{\epsilon}_{ph}(\theta_e, i_{ph})$$

Accordingly, unmodelled dynamics can be expressed as,

$$\zeta(t) = \left[\tilde{r}_{ph} - \hat{r}_{ph}\left(\frac{\tilde{l}_{ph}}{\hat{l}_{ph}(\theta_e, i_{ph})}\right)\right]\frac{i_{ph}}{l_{ph}(\theta_e, i_{ph})} + \frac{\tilde{l}_{ph}}{l_{ph}(\theta_e, i_{ph})}(u_{ph}(t) - \hat{\epsilon}_{ph}(\theta_e, i_{ph}) - \frac{\tilde{l}_{ph}}{l_{ph}(\theta_e, i_{ph})}\tilde{\epsilon}_{ph} + \eta \quad (3.18)$$

For a fixed sampling frequency (ω_s), the discrete-time domain counterpart of the current dynamics in (3.17) becomes:

$$i_{ph}(k+1) = A(k)i_{ph}(k) + B(k)(u_{ph}(k) - \epsilon_{ph}(k)) - \zeta'(k) \quad (3.19)$$

In (3.19), the $[1 \times 1]$ state transition and input matrices A and B are:

$$A(k) = e^{-\frac{\hat{r}_{ph}}{\hat{l}_{ph}(k)}T_s}$$

$$B(k) = \frac{\hat{r}_{ph}}{\hat{l}_{ph}(k)}\int_{kT_s}^{(k+1)T_s} e^{\left(1-\frac{\hat{r}_{ph}}{\hat{l}_{ph}(k)}\right)\lambda}\, d\lambda \quad (3.20)$$

While $\hat{l}_{ph}(k)$ and $\zeta'(k)$ represent the averaged values of phase inductance and unmodelled dynamics over a sampling period: $kT_s - (k+1)T_s$. In (3.20), $\hat{l}_{ph}(k)$ is calculated as,

$$\hat{l}_{ph}(k) = \frac{1}{T_s}\int_{kT_s}^{(k+1)T_s} \hat{l}_{ph}(\theta_e, i_{ph})d\lambda \quad (3.21)$$

Visual examination of Eq.(3.20) and Eq.(3.21) reveals that the matrices A and B vary as functions of sampling instant, the phase current magnitude and speed. The variation in $\hat{l}_{ph}(k)$ is a function of phase current magnitude as well as rotor position. The effect of magnetic saturation and variation in span of inductance profile being covered per sampling period due to different operating speeds causes the system matrices

(Eq.(3.20)) vary as a function of operating condition. This phenomenon is depicted in Fig.(3.2). The first direct implication of this variation in the system matrices is on the dynamic response consistency. In essence, The increasing inductance profile dictates the need for increasingly large control effort to maintain the desired bandwidth throughout the conduction period and this effect gets further aggravated at higher speed.

Disturbances and Unmodelled Dynamics

The induced EMF profile $\hat{\epsilon}_{ph}(\theta_e, i_{ph}, \omega_e)$ and the mismatched disturbance $(\zeta(t))$ appear in discrete-time domain as,

$$\hat{\epsilon}_{ph}(k) = \frac{1}{T_S}\int_{kT_s}^{(k+1)T_s} \hat{\epsilon}_{ph}(\theta_e, i_{ph}, \omega_e)\, d\lambda$$

$$\zeta'(k) = \frac{1}{T_s}\int_{kT_s}^{(k+1)T_s} \zeta(t) d\lambda \tag{3.22}$$

As described in Eq.(3.19), $\hat{\epsilon}_{ph}(k)$ appears through the same channel as the input. Therefore, its effect is considered as 'matched'. On the other hand the mismatched disturbance $\zeta(t)$ is not entirely known. However, its nature can be considered smooth and predictable as Eq.(3.18). As depicted in the Fig.(3.2), the magnitude of $\hat{\epsilon}_{ph}(k)$ grows as a function of speed, whereas the magnitude of $\zeta(t)$ depends entirely upon the modelling errors and measurement noise. Both of these factors pose detrimental effect on control performance and demand effective compensation.

Table 3.1: Evaluation criteria for control performance assessment

No.	Criterion	Category
1	Compensation of inductance variation over conduction period	dynamic response consistency
2	Induced EMF decoupling	Matched disturbance rejection
3	compensation of un-modelled dynamics	Robustness towards mismatched disturbance
4	Frequency warping effect	Performance at high speed
5	Memory utilization	Processor requirements
6	Computational burden	

Frequency Warping Effect and Near Base Speed Performance

The controller synthesis in continuous-time domain is often approximated for digital implementation by a rule of thumb: $\omega_s \geq 5(\omega_e)$. This approximation helps in identification of maximum controllable electrical speed [Kim *et al.* (2019)]. This effect grows gradually as the operating speed increases. Therefore, it is essential to verify the consistency in control performance near base speed.

In the view of above discussion, six criteria are established as shown in Table 3.1. The order of appearance of each criterion is determined according to the priority: dynamic response consistency, robustness towards disturbances and parameter variation and processing requirements.

This criteria forms the basis of the comparative analysis of the control techniques presented in the next chapter.

3.5 Summary

This chapter presents the proposed torque control framework for switched reluctance machines. Initially, the torque control system in SRM drives is presented in the form of a nonlinear optimization problem and the challenges related to its implementations are described. Subsequently, the proposed approach of splitting this problem into two sub-problems, viz. identification of current references and current control is presented.

The identification of current references is performed through an optimization problem targeted at minimization of torque ripple and the secondary objectives viz, copper loss and mode-0 radial force minimization. For implementation over a digital microcontroller at a fixed switching frequency modulation, the electromagnetic model of SRM is discussed in discrete-time domain. Based on this analysis a criterion is developed to evaluate the performance of the current controllers reviewed in the next chapter.

Chapter 4

Fixed Switching Frequency Current Control Techniques and Comparative Analysis

4.1 Introduction

In literature, a myriad of methods is proposed to tackle the SRM current control challenges presented in the previous chapter. These methods can be broadly classified as, model-based and observer-based. The model-based systems make use of the knowledge of machine dynamics in the form of phase inductance or flux linkage profile and induced EMF profiles, stored in the microprocessor memory. On the other hand, the observer-based systems rely on online identification of the machine dynamics. The main advantage of the model-based systems is the immunity towards noise which allows calculation of numerical derivatives and enables feed-forward compensation of disturbances. However, the discrepancies in the model information and large memory requirement are the main drawbacks of the model-based systems.

The observer-based systems are more robust to the plant variation. Thanks to their ability to identify changes in the model characteristics online, they can also be used to improve fault tolerance. Consequently, these systems do not need large microprocessor memory. However, online identification process often involve more computational efforts as compared to model-based systems. Also, the identifiablity of the plant can not be ensured in all the operating conditions and the estimation quality is heavily affected by the noise content in the measurement.

Table 4.1 provides the classification of the widely implemented control techniques from literature along with their corresponding implementation strategies, specific to the current control of an SRM drive. The purpose of this chapter is to provide a sufficiently thorough theoretical analysis of the unique dynamic response of the SRM drive presented earlier in the previous chapter, when subjected to the distinct operating principle of each control technique. Although this list is not exhaustive, the control techniques covering in the scope of this chapter mainly differ on account of their governing principles and often serve as foundation for advanced versions.

Accordingly, almost all the approaches proposed for fixed switching frequency current control in the literature involve modifications in terms of plant modelling and/or involve combination of one or more control techniques enlisted in Table 4.1 to achieve improved performance for a specific application.

In this chapter, a comprehensive analysis of these control techniques is presented using the control evaluation criteria established in the previous chapter followed by a comparative analysis and recommendations for performance improvement.

Table 4.1: Candidate control techniques under review

Category	Application framework	Controller
Linear	Fixed gain and dynamic gain scheduling	PI
	Fixed and variable structure	H_2 and H_∞
	Linear Quadratic Regulator	Model predictive control
	Linear Quadratic Gaussian	
	Dead beat	
	Feedback linearizing control	Proportional Controller
Non-linear	Conventional	Sliding mode
	Integral compensation	
	Higher order(≥ 2)	
	Stability based	Adaptive
	Passivity based	

4.2 Feedback Linearizing Control

The precursor of most of the SRM control technologies can be traced back up to the work by Spong *et al.* [Ilic *et al.* (1987); Ilic-Spong *et al.* (1987)] addressing the instantaneous torque control of SRM with the help of torque sharing functions and using feedback linearizing (FL) control.

The SRM flux linkage characteristic is a nonlinear function of phase current as well as rotor electrical position. In FL control, linearization is achieved using the knowledge of flux linkage gradient in both current and rotor position. For this purpose, a Fourier series based model is proposed in [Ilic *et al.* (1987)]. According to this model, the phase flux linkage characteristic is represented as,

$$\psi_{ph}(i_{ph}, \theta_e) = \psi_s \left[1 - e^{-i_{ph} f_{ph}(\theta_e)}\right] \tag{4.1}$$

In Eq.(4.1), the nonlinear relation between the phase flux linkage and rotor electrical position is modelled using a strictly positive Fourier series function: $f_{ph}(\theta_e)$ and saturation due to current is modelled by the combination of saturated value of phase flux linkage: ψ_s and an exponential function.

The nonlinear model presented in Eq.(4.1), is continuously differentiable in i_{ph} and θ_e. Thus the phase current dynamics can be readily calculated by taking the partial derivatives of Eq.(4.1) with respect to phase current, $\left(\dfrac{\partial\psi_{ph}}{\partial i_{ph}}\right)$ as well as the rotor electrical position: $\left(\dfrac{\partial\psi_{ph}}{\partial\theta_e}\right)$ and stored in microprocessor memory. These functions are utilised to model the phase current dynamics as,

$$\frac{di_{ph}(t)}{dt} = -\left(\frac{\partial\psi_{ph}}{\partial i_{ph}}\right)^{-1}\left[r_{ph}i_{ph}(t) + \frac{\partial\psi_{ph}}{\partial\theta_e}\omega_e\right] + \left(\frac{\partial\psi_{ph}}{\partial i_{ph}}\right)^{-1} u_{ph}(t) \tag{4.2}$$

Continuous differentiability of $\left(\dfrac{\partial\psi_{ph}}{\partial i_{ph}}\right)$ and $\left(\dfrac{\partial\psi_{ph}}{\partial\theta_e}\right)$ functions also ensures the existence of 'diffeomorphism' which enables stable feedback linearization [Isidori (2013)]. However, this principle also imposes following constraint:

$$\frac{\partial\psi_{pm}}{\partial i_{ph}} > 0 \tag{4.3}$$

Intuitively, from Eq.(4.2), a state-feedback linearization can be achieved as [Ilic *et al.* (1987)]:

$$u_{ph}(t) = r_{ph}i_{ph}(t) + \frac{\partial\psi_{ph}}{\partial\theta_e}\omega_e + \frac{\partial\psi_{ph}}{\partial i_{ph}}v_{ph}(t) \tag{4.4}$$

The linearization achieved using Eq.(4.4) transforms Eq.(4.1) into a linear system. Thus, a constant gain controller is sufficient to achieve necessary dynamic response.

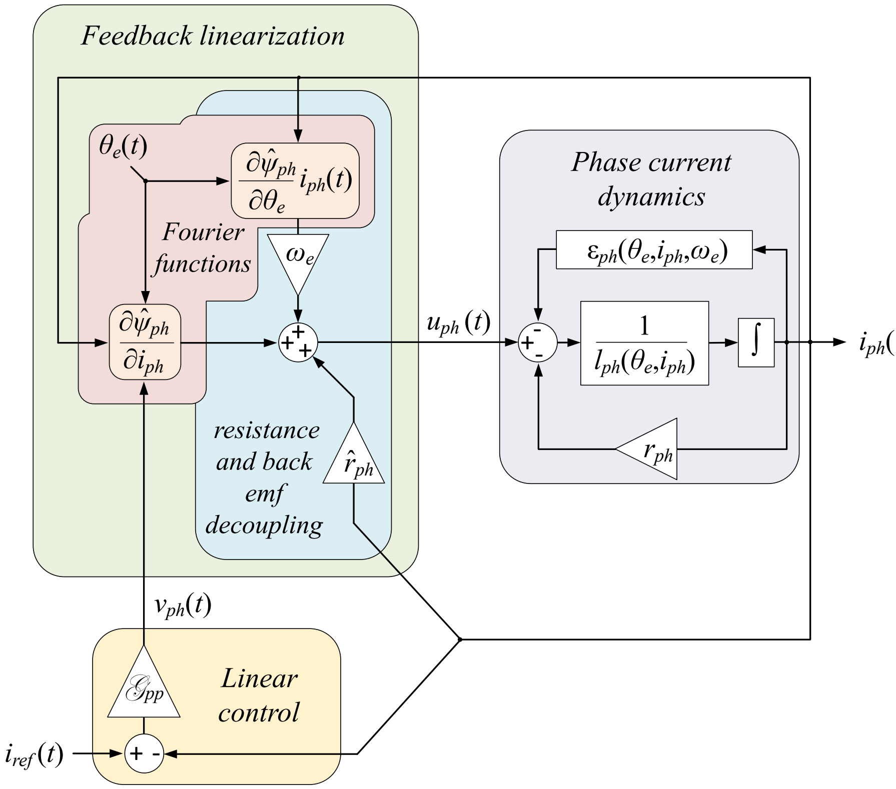

Figure 4.1: Feedback linearizing control

The control law $v_{ph}(t)$ in Eq.(4.4) can be obtained via simple pole placement design:

$$v_{ph}(t) = \mathscr{G}_{pp} e_i(t) \tag{4.5}$$

The overall FL current control scheme is shown in Fig.(4.1). Evidently from Eq.(4.4), The control performance of FL control depends heavily upon the accuracy of the linearizing functions, $\left(\frac{\partial\psi_{ph}}{\partial i_{ph}}\right)$ and $\left(\frac{\partial\psi_{ph}}{\partial\theta_e}\right)$. It is important to note here that, the condition in (4.3) becomes much more stricter due to finite sampling frequency and DC-link voltage limit and a minimum safe value of $\left(\frac{\partial\psi_{ph}}{\partial i_{ph}}\right)$ should be identified experimentally.

Due to the parametric nature of Eq.(4.1), the errors in parameter information leads

Table 4.2: Control performance evaluation of FL control

Criteria	Mechanism
inductance variation	Fourier function: $\left(\dfrac{\partial \psi_{ph}}{\partial i_{ph}}\right)$
Induced EMF decoupling	Fourier function: $\left(\dfrac{\partial \psi_{ph}}{\partial \theta_e}\right) \omega_e$
Compensation of parameter variation	Adaptive estimation
Frequency warping effect	Compensation not possible
Memory requirement	Moderate size to store the coefficients of the Fourier series
Computational burden	Very large due to 2-D Fourier series calculations and matrix computation in adaptive estimation

to deterioration in control law, Eq.(4.4). To address this issue, online adaptation is proposed in [Amor *et al.* (1993); Panda and Dash (1996)] and [Jacobson *et al.* (1995)]. In [Amor *et al.* (1993)] the authors proved that for use of nonlinear model in feedback linearization control, the number of parameters to be identified becomes unrealistically high which eventually limits the utility of this method for practical applications.

To reduce the number of parameter, [Taylor (1990)] proposed a linear model with reduced number of parameters. However, this provision hampers the control performance for heavy load conditions.

Based on this discussion, the complete performance evaluation of the FL control is presented in the Table 4.2.

4.3 Fixed and Dynamic Gain Scheduling PI Controller

The use of PI controllers for current control of switched reluctance machines with fixed gains [Bae *et al.* (2000); Cardenas *et al.* (2005); Gan *et al.* (2016)] and [Hannoun *et al.* (2011a); Lin *et al.* (2010); Schulz and Rahman (2003)] with dynamic gain scheduling are some of the main contributions in this area. Several other contributions also include, fuzzy PI controllers [Chowdhuri *et al.* (2006); Wang and Liu (2010)] and artificial neural network [Karakas and Vardarbasi (2007)].

The dynamic performance required by the industrial drives can not be achieved by the linear control techniques such as PI or PID with fixed gains over whole conduction period [Panda and Dash (1996)]. A study of fixed PI controller design by Ahmad and

Narayanan [Ahmad and Narayanan (2016)] presents design of linear controllers in four operating conditions: aligned ($\theta_e = 0$ radians) and unaligned ($\theta_e = \pi$ radians) for saturated and unsaturated conditions. It is concluded that the controller design for fully saturated unaligned condition is the best choice to obtain stable performance in all the remaining operating conditions. However, due to fixed nature of controller gain, the consistency in the dynamic response can not be ensured.

Intuitively, if sufficiently accurate feed-forward decoupling of induced EMF is possible, an analytical equation for inductance profile as a function of current and rotor position can be used to adopt proportional and integral gains. Under this approach, Shulz and Rahman [Schulz and Rahman (2003)] proposed a pole cancellation process neglecting the resistance drop. Therefore, the phase current dynamics reduce to the following form:

$$\frac{di_{ph}(t)}{dt} = \frac{u_{ph}(t)}{l_{ph}(\theta_e, i_{ph})} \tag{4.6}$$

It is worth noting here that Eq.(4.6) is a small signal representation appearing as a consequence of local linearization. In [Lin *et al.* (2010)], resistance is also included in the gain adaptation process. Under this approach, the integral gain remains fixed at $r_{ph}\omega_{bw}$ and the proportional gain follows the function: $l_{ph}(\theta_e, i_{ph})\omega_{bw}$.

Similar to [Lin *et al.* (2010)], Hannoun and Hilairet [Hannoun *et al.* (2011a)] proposed dynamic adaption in PI gains to maintain a consistently linear 2^{nd} order dynamic response. This approach is more insightful and provides greater flexibility in terms of dynamic performance shaping.

The utility of 'gain scheduling' discussed above, can be demonstrated by analysing the current error dynamics under PI control law:

$$\dot{e}_i(t) + \frac{K_p}{l_{ph}(\theta_e, i_{ph})} e_i(t) + \frac{K_i}{l_{ph}(\theta_e, i_{ph})} \int_0^t e_i(t)dt = 0 \tag{4.7}$$

For the sake of simplicity, the effect of $\zeta(t)$ is excluded from Eq.(4.7) and the variation in current reference profile is considered slow in comparison with phase current. $(\dot{i_{ph}}(t) >> \dot{i_{ref}}(t))$. Thus, a linear 2^{nd} order convergence of in the error dynamics at desired bandwidth: ω_{bw} can be achieved with the following gain scheduling scheme [Hannoun *et al.* (2011a)]:

$$\begin{aligned} K_p &= 2\omega_n l_{ph}(\theta_e, i_{ph}) \\ K_i &= \omega_n^2 l_{ph}(\theta_e, i_{ph}) \end{aligned} \tag{4.8}$$

With this provision, a consistent error convergence is ensured irrespective of the rotor position as,

$$e_i(t) = e_i(0)(1 + \omega_{bw} t)e^{-\omega_{bw} t} \tag{4.9}$$

The parameter information necessary to realise PI control law using Eq.(4.8), is stored in the microprocessor memory in the form of 2-D LUTs with breakpoints in rotor position and phase current as shown in Fig.(4.2). Under practical conditions, the parametric error appearing due to errors in current and position measurement and modelling imperfections, the unmodelled dynamics (Eq.(3.18)) appear in the form of damped oscillations due to asymptotic nature of disturbance compensation by PI controller. By principle, the effectiveness of compensation provided by PI controller is inversely proportional to oscillation frequency of $\zeta(t)$. Thus, at higher speed, the compensation also reduces significantly which eventually threaten the control loop

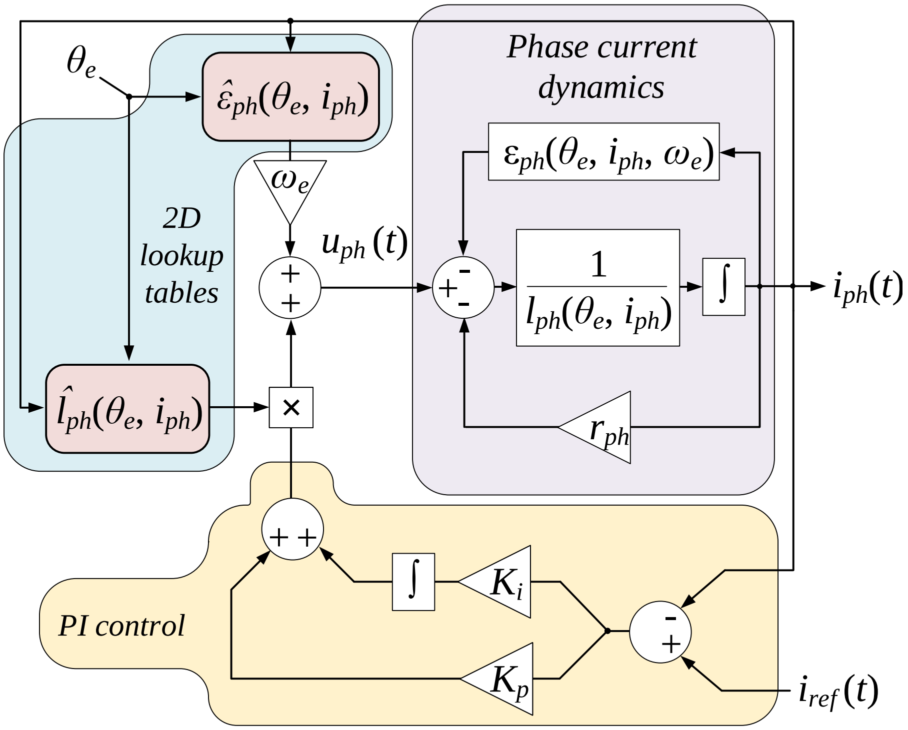

Figure 4.2: PI control with dynamic gain scheduling

Table 4.3: Control performance evaluation of PI control

Criteria	Mechanism
inductance variation	Dynamic gain scheduling Using inductance LUT
Induced EMF decoupling	Feed-forward compensation using induced EMF LUT
compensation of parameter variation	Controller effort aided by active damping
Frequency warping effect	significant due to Jacobi linearization
Memory requirement	large memory requirement for the storage of inductance and induced EMF LUTs
Commputational burden	Moderate, mainly due to interpolation over 2-D LUTs

stability. In such case, an artificial damping effect is generated by virtually dissipating the control energy [Dannehl *et al.* (2010)].

Unlike FL control, PI control is developed using 'Jacobi linearization' which employs local linearization of the machine dynamics instead of a transform. A detailed account on this difference can be found in [Frobenius (1895)]. The inductance lookup table used for dynamic adaptation in the controller gain represents locally linearized model of phase winding. This approach is effective when the difference in the model information for successive sampling instances is sufficiently small. As the speed increases, increasingly large variations in the inductance profile causes deterioration in the control performance. This phenomenon is essentially the origin of the frequency warping effect discussed in Section 3.4.1.

The above discussion is summarised under control performance evaluation criterion in Table 4.3.

4.4 H_2/H_∞ Control

One of the most reliable feedback optimisation methods, H_2/H_∞ synthesis is classified as a robust control technique. This approach involves identification of an optimum control structure which provides desired closed-loop characteristics over a wide frequency range. One of the main advantages of H_∞ control lies in its suitability for multi-input, multi-output systems with considerable cross-coupling. However, for a fixed structure application, the system order becomes impractically large and approximate reduction becomes necessary which often comes at the expense of performance degradation. Moreover, sufficient care should be taken for application in the sampled data systems with signification sampling delays. In switched reluctance machines, the H_2/H_∞ control techniques have found application for speed control [Rajendran and Padma (2012); Rigatos *et al.* (2019)] and specifically for current control [Fadhel *et al.* (2017); Ouddah *et al.* (2014)].

Two main approaches for H_2/H_∞ controller design are: fixed structure synthesis and normalisation of co-prime factorisation [Francis (1987)]. Both of these approaches involve normed minimisation of the closed-loop transfer function. In particular, for H_∞ design, a supremum norm minimisation is performed:

$$\min_{W_{pre}(s),K_h,W_{post}(s)} \left\| \frac{G_p(s)}{1+G_p(s)W_{pre}(s)K_hW_{post}(s)} \right\|_\infty \tag{4.10}$$

Whereas, an H_2 design is obtained via minimisation of a Euclidean norm:

$$\min_{W_{pre}(s),K_h,W_{post}(s)} \left\| \frac{G_p(s)}{1+G_p(s)W_{pre}(s)K_hW_{post}(s)} \right\| \tag{4.11}$$

In Eq.(4.10) and Eq.(4.11), $G_p(s)$ represents the open-loop transfer function of SRM

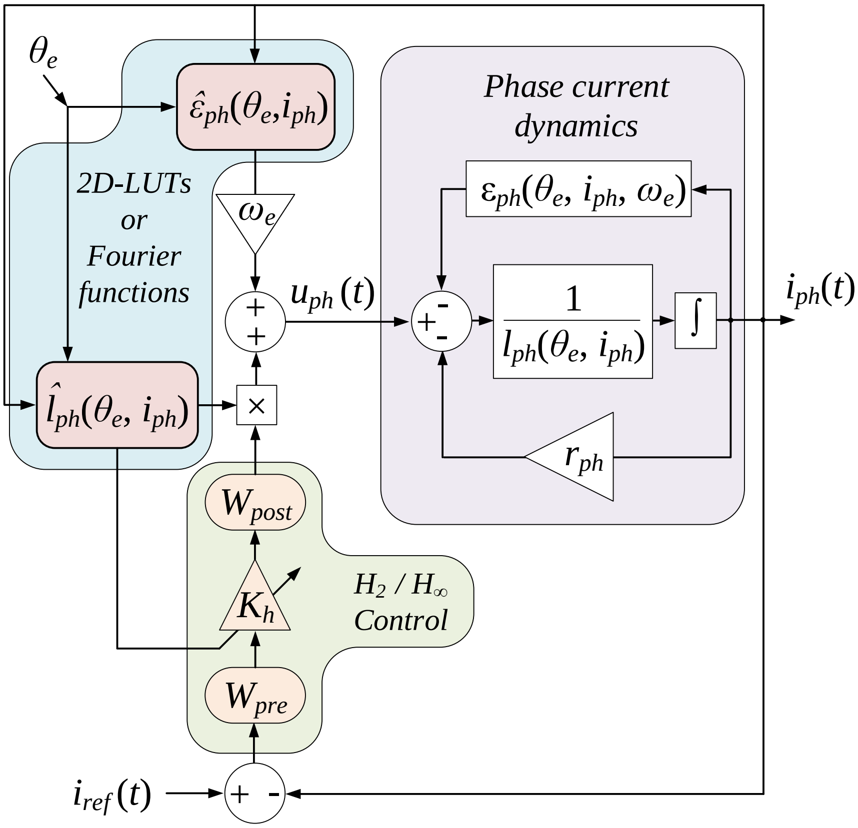

Figure 4.3: H_2/H_∞ control

phase winding and K_h is the controller gain. Similar to the FL and PI control designs, gain adaptation as a function of the inductance profile and induced EMF decoupling can be employed to simplify the design process [Fadhel *et al.* (2017); Ouddah *et al.* (2014)]. The resultant control realisation thus obtained, is shown in Fig.(4.3). It is perceivable from (4.10) and (4.11) that H_∞ is more conservative approach as compared to H_2 and should be preferred under noisy measurement conditions.

In the above discussed structure of H_2/H_∞ control, the value of K_h is defined to maintaining desired bandwidth while the post filter W_{pre} is used as a compensator to improve stability margins. As discussed earlier, the switched reluctance machine

Table 4.4: Performance evaluation of H_2/H_∞ Control

Criteria	Mechanism
inductance variation	Adaptation in K_h using inductance LUT
Induced EMF decoupling	Feed-forward compensation using induced EMF LUT
compensation for unmodelled dynamics	Lead compensation using W_{pre}
Frequency warping effect	significant due to Jacobi linearization
Memory requirement	Large memory is required for the storage of 2-D inductance and Induced EMF LUTs
Commputational burden	Moderate, mainly due to the interpolation over 2D LUTs

is a nonlinear plant hence, K_h is varied as a function of rotor position while W_{post} resembles a PI controller.

All the approaches in the literature present continuous-time domain designs. In addition to the bandwidth limitation arising due to the post filter, the tracking capability of H_2/H_∞ controllers deteriorate as the operating speed increases and similar to the PI control, the limitations arising due to frequency warping effect are also persistent.

Although the H_2/H_∞ synthesis is readily applicable for multi-input multi-output systems, for SRM current control, it is sufficient to consider independent Single-Input Single-Output (SISO) systems per phase, unless there is a significant effect of mutual coupling.

In a nutshell, the H_∞ control synthesis provides additional flexibility over PI control design in terms dynamic response shaping and disturbance rejection. Especially under the effect of phase margin degradation due to aggressive control effort, the lead compensator or saturation, (W_{pre}) becomes very useful. Moreover, as opposed to PI design alone, the compensation of the unmodelled dynamics described in Eq.(3.18) is far more effective in H_2/H_∞ control.

A summary of the performance analysis of H_2/H_∞ control discussed in this section is presented in Table 4.4.

4.5 Quadratic Regulators:(LQR/LQG)

The LQR design is considered as a breakaway from the conventional stability margin-based designs discussed in the previous sections. Under this approach, an optimal state estimator is often employed to achieve greater noise immunity, resulting into an LQG design.

A typical LQR/LQG design involves identification of an optimum sequence of the control input over a desired number of future sampling instances, known as control horizon (H_c). For a strictly linear SISO system, a Controlled Auto-Regressive Integrated Moving-Average (CARIMA) model is employed to identify the state dynamics for a span of future sampling instances know as prediction horizon ($H_p > H_c$):

$$\begin{bmatrix} x(k+1) \\ \vdots \\ x(k+H_c) \\ \vdots \\ x(k+H_p) \end{bmatrix} = \begin{bmatrix} B & \cdots & 0 & \cdots & 0 \\ \vdots & \ddots & \vdots & \ddots & \vdots \\ A^{H_c-1}B & \cdots & 0 & \cdots & 0 \\ \vdots & \ddots & \vdots & \ddots & \vdots \\ A^{H_p-1}B & \cdots & A^{H_c-1}B & \cdots & B \end{bmatrix} \begin{bmatrix} u(k) \\ \vdots \\ u(k+H_c-1) \\ \vdots \\ u(k+H_p-1) \end{bmatrix} + \begin{bmatrix} A \\ \vdots \\ A^{H_c} \\ \vdots \\ A^{H_p} \end{bmatrix} x(k) \quad (4.12)$$

While, the cost function is defined on the basis of a trade-off between the control accuracy and the effort as:

$$J = \frac{1}{2}\left[e_{H_c}^T Q e_{H_c} + u_{H_C}^T R u_{H_c}\right] \tag{4.13}$$

In Eq.(4.12), the magnitudes of the $[H_c \times H_c]$ positive symmetric matrices Q and R act as weighing functions. For Constant A and B matrices, the entire control sequence can be identified by obtaining an offline solution for the 'Algebraic Riccati Equation' (ARE) corresponding to the model Eq.(4.12) and cost function J. As described in the previous chapter, the switched reluctance machine does not exhibit a linear dynamical behaviour. Hence, the approach presented above, cannot be directly utilised to ensure a reliable tracking performance and a fixed gain structure is sufficient only for the development of a stable sub-optimal controller. In literature, this issue is addressed from the modelling point of view. Except [Sadeghzadeh and Araabi (2006)], the model information is stored in the form of locally linearized flux-linkage or inductance lookup tables [Ahmad and Narayanan (2018); Li and Shamsi (2015a,b)]. The main advantage of this approach is that, it ensures the validity of algebraic approximation of the differential Riccati equation [Kalman (1960)]. With augmentation of parameter estimation mechanism the complete LQR/LQG control loop can be represented as shown in the Fig.(4.4).

In optimal control theory, the SRM current control design is classified as a servo control problem [Alharkan *et al.* (2020)]. Under this approach, for a given control horizon of H_c, the quadratic performance index at a sampling instant k is defined as,

$$V(k) = \sum_{i=k}^{k+H_c} (e_i(i)^2 Q + u_{ph}^2(i) R) \tag{4.14}$$

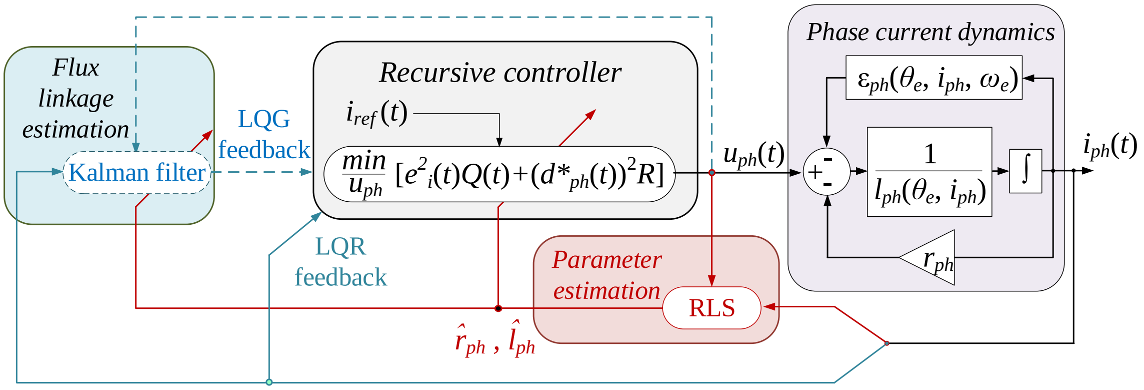

Figure 4.4: LQR/LQG control

Due to its simple structure, almost all the LTV approaches presented in literature involve a flux linkage based model as opposed to the inductance based model. The relation between these models can be described as,

$$\psi_{ph}(t) = i_{ph}(t)l_{ph}(t) \Rightarrow \frac{d\psi_{ph}(t)}{dt} = l_{ph}(t)\frac{di_{ph}(t)}{dt} + \epsilon_{ph}(t) \tag{4.15}$$

By substitution of Eq.(4.15) in Eq.(3.17), an LTV state space representation of the tracking control problem is obtained as,

$$X_\psi(k+1) = A(k)X_\psi(k) + Bu_{ph}(k) \tag{4.16}$$

Where, $A(k) = \begin{bmatrix} \left(1 - \dfrac{\hat{r}_{ph}}{\hat{l}_{ph}(k)}\right) & 0 \\ 0 & F(k) \end{bmatrix}$ is a state transition matrix and $B = \begin{bmatrix} T_s & 0 \end{bmatrix}^T$ is an input matrix. The reference profile model, $i_{ref}(k+1) = F(k)i_{ref}(k) + i_c$ is an LTV system whose dynamics are well known. Consequently, the new quadratic performance index becomes [Anderson and Moore (2007)]:

$$\mathscr{V}(k) = \sum_{i=k}^{H_c} \left[X_{\psi}^{T}(k)Q'(k)X_{\psi}(k) + u_{ph}^{2}(k)R\right] \tag{4.17}$$

Where, the new performance index responsible for current regulation accuracy is a time varying function defined as,

$$Q'(k) = \begin{bmatrix} \dfrac{Q}{l^2(k)} & \dfrac{-Q}{l(k)} \\ \dfrac{-Q}{l(k)} & Q \end{bmatrix} \tag{4.18}$$

This provision stipulates necessary adaptation in the current controller gain to maintain a constant bandwidth over entire conduction period. In [Alharkan *et al.* (2020); Li and Shamsi (2015a,b)], the optimisation variable Q for locally linearized model is stored in the form of an LUT to be utilised for online computation of optimum controller gain. Noticeably, this scheme assumes availability of accurate parameter information. Thus, optimum trajectory can be split into its constituents, each spanning over a sampling period [Kirk (2004)]:

$$\begin{aligned} X_{\psi}^{T}(k)P(k)X_{\psi}(k) = X_{\psi}^{T}(k)Q'(k)X(\psi)(k) + u_{ph}^{2}(k)R \\ + X_{\psi}^{T}(k+1)P(k)X_{\psi}(k+1) \end{aligned} \tag{4.19}$$

Where, $P(k)$ is a positive symmetric matrix to be identified in each sampling instant, from a ‘Hamiltonian’ function given below.

$$\begin{aligned}\mathscr{H}(k) = X_\psi^T(k)Q'(k)X_\psi(k) - X_\psi^T(k)P(k)X_\psi(k) \\ + X_\psi^T(k)\Big[\mathscr{K}(k)^T R\mathscr{K}(k) + A(k)^T P(k)A(k)\Big]X_\psi(k) \\ + X_\psi^T(k)\Big[A(k)^T P(k)B\mathscr{K}(k) + \mathscr{K}(k)^T B^T P(k)A(k) \\ + \mathscr{K}(k)^T B^T P(k)B\mathscr{K}(k)\Big]X_\psi(k) \quad (4.20)\end{aligned}$$

The convexity of Eq.(4.20) is ensured by considering linear nature of the machine model over a sampling period. Therefore, the optimum control voltage for a sampling instant, k can be defined as $u_{ph}(k) = \mathscr{K}(k)X_\psi(k)$ where, $\mathscr{K}(k)$ is constant over a sampling period. The solution of this Hamiltonian results into $u_{ph}(k)$ as a function of $\psi_{ph}(k)$ feedback and $i_{ref}(k+1)$ feed-forward terms [Kiumarsi-Khomartash *et al.* (2013)].

$$u_{ph}(k) = \frac{P_{11}(k)\left(1 - \frac{\hat{r}}{\hat{l}(k)}\right)T_s}{(R + T_s^2)}\psi_{ph}(k) + \frac{P_{12}(k)T_s}{(R + T_s^2)}i_{ref}(k+1) \quad (4.21)$$

For some systems, the dc link voltage is measured with the help of a voltage sensor and inductance and resistance are identified using either least square or adaptive parameter estimation. A least square based estimation algorithm tries to fit a the nonlinear SRM model into a linear LTI system as,

$$\psi_{ph}(k) = \phi^T(k-1)p \quad (4.22)$$

In SRM however, the parameter vector: $p(k) = \left[\left(1 - \dfrac{r}{l(k)}\right) \quad T_s\right]^T$ is a time varying quantity being modelled using the input vector: $\phi^T(k-1) = [\psi_{ph}(k-1) \quad u_{ph}(k-1)]$. Intuitively, an assumption on insignificant variation in parameters over successive sampling instances is inevitably involved in this process [Li and Shamsi (2015b)]. In the view of time varying nature of the parameters, a 'Recursive Least Square' (RLS) algorithm naturally becomes the best choice thanks to its computational economy and fast response [Eweda and Macchi (1987)]. Assuming sufficiently low noise in current sensing, two sampling instances can be considered sufficient to obtain accurate parameter information. Accordingly, following equation is implemented recursively.

$$\begin{aligned} p(k) \approx p(k-1) = \left[\phi(k-1))(\phi^T(k-1)) + \phi(k-2))(\phi^T(k-2))\right]^{-1} & \\ \times \left[\phi(k-1)\psi_{ph}(k) + \phi(k-2)\psi_{ph}(k-1)\right] & \quad (4.23) \end{aligned}$$

The identified parameters via Eq.(4.23) at a sampling instant are averaged over two preceding instances. Thus incurring a delay of 1.5 samples. This value can be reduced very close to 1 by addition of an exponential forgetting factor [Johnstone *et al.* (1982)]. However, it comes at the cost of higher reliance over the latest samples. Considering accurate DC link voltage measurement and its constant nature, the knowledge of second parameter can be considered very well known and its contribution to the overall error being negligibly minimum. The estimated parameters appear as inverse of the inductance. Considering this effect, if the multiplicative uncertainty is defined as, $\delta a(k) = \dfrac{1}{1+\frac{\tilde{l}(k)}{l(k)}}$, the corresponding deterioration in the control accuracy performance index becomes:

$$\Delta Q'(k) = \begin{bmatrix} \dfrac{(\delta a(k)-1)Q}{l^2(k)} & -\dfrac{(\delta a(k)-1)Q}{l(k)} \\ -\dfrac{(\delta a(k)-1)Q}{l(k)} & 0 \end{bmatrix} \quad (4.24)$$

Along with the error in the estimated state transition matrix, the error in Hamiltonian becomes:

$$\begin{aligned}\delta\mathscr{H}(k) = x_{\psi}(k)^{T}\delta A^{T}P(k)X_{\psi}(k) \\ + X_{\psi}^{T}(k)\delta A(k)P(k)BX_{\psi}(k) \\ + X_{\psi}^{T}(k)^{T}B^{T}P(k)\delta A(k)X(k)\end{aligned} \quad (4.25)$$

The dynamics of Eq.(4.25) are exactly the same as the discrete-time domain counterpart of unmodelled dynamics represented in Eq.(3.18). As the speed increases, the magnitude of $\delta\mathscr{H}(k)$ grows which further deteriorates the control performance.

Based on the this discussion, it becomes clear that the error in parameter information is the primary source of control performance deterioration for the quadratic regulators. Nevertheless, the utility of this control technique has been proved in the literature with good tracking accuracy for reasonable magnitude of switching frequency. Based on the above discussion, the control performance assessment of quadratic regulators is summarised in Table 4.5.

4.6 Sliding-Mode Control

The proven robustness characteristics of the sliding mode control (SMC) technology have inspired several applications in SRM control. Due to very fast dynamics of the electromagnetic model, the classical discontinuous switching function based sliding mode control alone becomes infeasible for current control application due to limited sampling and switching frequencies. However, PI aided hybrid [Haiqing *et al.* (1996)] and integral compensation [Shang *et al.* (2009); Ye *et al.* (2014)] have been successfully implemented with good tracking performance. The loss of finite time convergence

Table 4.5: Performance evaluation LQR/LQG control

Criteria	Mechanism
inductance variation	Scheduling of control accuracy performance index(Q)
Induced EMF decoupling	Estimation of flux linkage dynamics using state estimator (LQG) or inductance information alone (LQR)
compensation of parameter variation	Online estimation of inductance using RLS
Frequency warping effect	Significant due to Jacobi linearized models used in state and parameter estimation
Memory requirement	Moderate, storage of Q function or inductance map is required
Computational burden	Very large due to recursive-nature of the algorithms involved in solving Hamiltonian at each time step

in these methods led to further investigation in higher order sliding-modes such as second order [Ben Salem *et al.* (2020); Rafiq *et al.* (2012)] and terminal [Divandari *et al.* (2020)].

The phase current dynamics of all the electrical machines including SRM are classified as relative degree 1 systems since the control voltage term appears as a function of 1^{st} derivative of phase current. Therefore, the desired dynamic response can be defined as:

$$\sigma(t) = \dot{e}_i(t) + \gamma |e_i(t)|^{\frac{1}{\upsilon}} sign(e_i(t)) \tag{4.26}$$

The parameters γ defines the overall control effort which is analogous to the desired closed-loop pole in classical control terminology, whereas tuning υ helps in optimising control effort near $e_i(t) = 0$. A good engineering judgement prescribes consideration of robustness towards measurement noise while maintaining fast dynamic response while choosing γ and υ. Perhaps the most important aspect of sliding mode control design is the balance between equivalent control and disturbance rejection terms [Shtessel *et al.* (2014)]. This principle can be demonstrated by analysing the control design process described ahead.

With *a priori* knowledge of the reference and phase current dynamics, Eq.(3.17) the optimum control voltage can be obtained by equating the sliding surface, Eq.(4.26) to zero. However, due to presence of $\zeta(t)$, it is not possible to accurately realise optimum $u_{ph}(t)$ which can effectively achieve and maintain $\sigma(t) = 0$. In an ideal sliding mode control design, this issue can is tackled by defining the control input into its known and unknown components: $u_{ph}(t) = u_{1ph}(t) + u_{2ph}(t)$ where $u_{1ph}(t)$ constitutes known part of $\sigma(t)$ dynamics and called as equivalent control law:

$$u_{1ph}(t) \;=\; \hat{l}_{ph}(\theta_e, i_{ph})\dot{i}_{ref}(t) + \hat{r}_{ph} i_{ph}(t) + \hat{\epsilon}_{ph}(\theta_e, i_{ph}) - \gamma |e_i(t)|^{\frac{1}{v}} sign(e_i(t)) \quad (4.27)$$

The second component of the input voltage: $u_{2ph}(t)$ is designed to compensate for the effect of $\zeta(t)$ and attain $\sigma(t) = 0$ also called as the reaching phase. By minimisation of a candidate Lyapunov energy function: $\mathscr{V}_i(t) = \dfrac{\sigma^2(t)}{2}$ with respect to $u_{ph}(t)$ and substitution: Eq.(4.27), the disturbance compensation term $u_{2ph}(t)$ is obtained as,

$$u_{2ph}(t) = \rho sign(\sigma(t)) \quad (4.28)$$

Where, the amplitude of the discontinuous switching term (ρ)in (4.28) is determined considering a conservative bound on unmodelled dynamics and desired rate of descend for $|\sigma(t)| = \alpha(\alpha > 0)$.

$$\rho = \|\zeta(t)\|_{\infty} + \frac{\alpha}{\sqrt{2}} \quad (4.29)$$

Fig.(4.5) depicts SRM phase current control using above formulation of sliding-mode

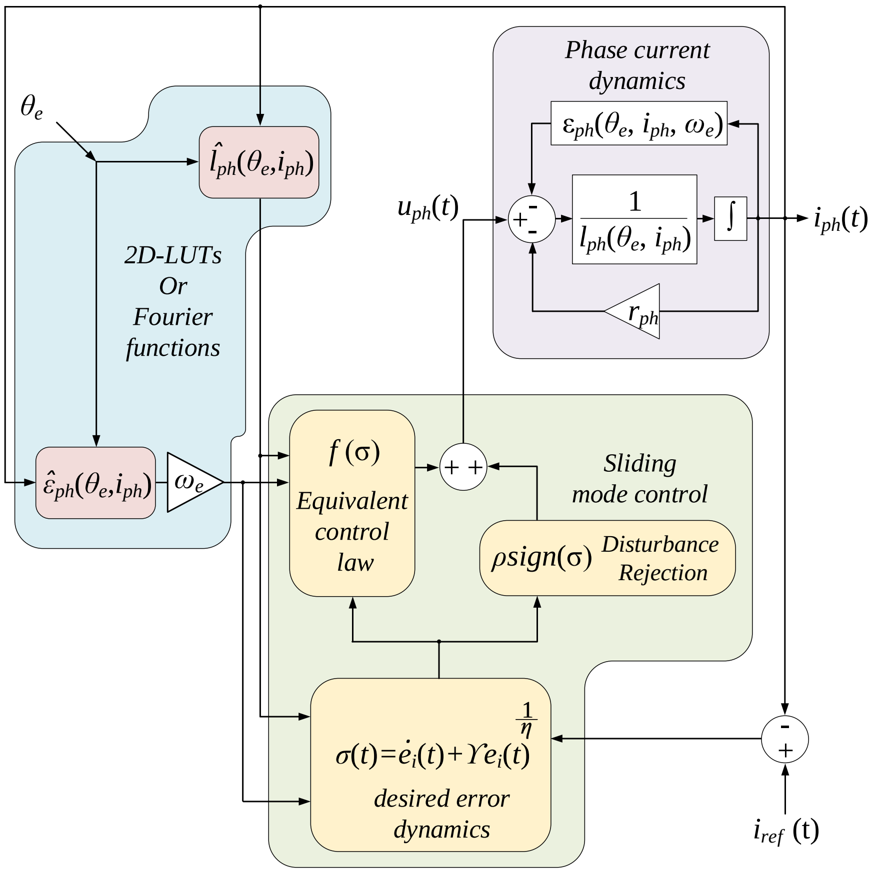

Figure 4.5: Sliding mode control

control.

An optimum control design demands minimum magnitude of the discontinuous switching while maintaining necessary rate of convergence during reaching phase. This can be achieved by maximising utilisation of a priory model information and reference current dynamics. This principle is very well demonstrated in [Ye *et al.* (2014)]. However, $\dot{i_{ref}}(t)$ is still considered unknown. This exclusion results into additional increase in magnitude of ρ.

It is also worth noting here that, the designs proposed in the literature and in

Table 4.6: Performance evaluation of sliding-mode current control

Criteria	Mechanism
inductance variation	Gain adaptation in equivalent control law using inductance profile
Induced EMF decoupling	Feed-forward decoupling using induced EMF profle
Compensation of unmodelled dynamics	High frequency approximation using discontinuous switching control
Frequency warping effect	Accuracy of equivalent control law reduces at high speed which is compensated by discontinuous switching control
Memory requirement	Induced EMF and inductance profile
Computational burden	Low due to non iterative process. However, calculation of υ^{th} root of current tracking error is expensive

this section belong to continuous-time domain which stipulates a strict limit on the frequency content of unmodelled dynamics for effective high frequency approximation of $\zeta(t)$ during sliding phase.

The performance evaluation of sliding mode control based on above discussion is summarised in Table 4.6.

4.7 Adaptive Control

The time varying nature of phase inductance profile in SRM pose a great challenge in terms of adaptive control synthesis for the SRM phase model Eq.(3.17). However, tracking accuracy improvement has been reported by augmenting parameter adaptation mechanism with feedback linearization by Taylor *et al*. [Taylor (1991)] and Bortoff [Bortoff *et al.* (1998)] while Peng [Peng *et al.* (2015)] and Szamel [Szamel (2002)] employed adaptive parameter estimation in dead-beat control. A more traditional approach of model reference adaptive control(MRAC) is demonstrated in [Naitoh and Ishikawa (2010)].

The adaptive control mechanisms introduced above are performed using stability based designs [Åström (1991)], while the passivity based control realisation can be found in [Espinosa-Pérez *et al.* (2004)] and [Isfahani *et al.* (2011)]. Both approaches operate on the principle of energy function shaping. For SRM current control however, the methods proposed in the literature can be classified as model reference based and parameter estimation based. The control implementation using both the approaches is depicted in Fig.(4.6).

The performance of these methods can be evaluated by analysing the control implementation processes for each of these techniques. Under MRAC approach, the control objective is to follow the current reference profile model:

$$\dot{i}_{ref}(t) = F(t)i_{ref}(t) + i_c(t) \tag{4.30}$$

Eq.(4.30) is a continuous-time equivalent of the reference profile model introduced in Section 4.5. By treating the induced EMF $\epsilon_{ph}(t)$ as a part of the $[1 \times 1]$ state matrix, following control and adaptation laws can be defined:

$$u_{ph}(t) = \hat{p}(t)\phi(t) \quad , \quad \dot{p}(t) = \begin{bmatrix} -\Gamma & \Gamma \end{bmatrix}^T e_i(t)\phi(t) \tag{4.31}$$

Where, $\hat{p}(t) = \begin{bmatrix} \hat{p}_1(t) & \hat{p}_2(t) \end{bmatrix}^T$ and $\phi(t) = \begin{bmatrix} i_c & -i_{ph}(t) \end{bmatrix}^T$. The performance of the control action described in (4.31) can be evaluated by analysing its corresponding class K

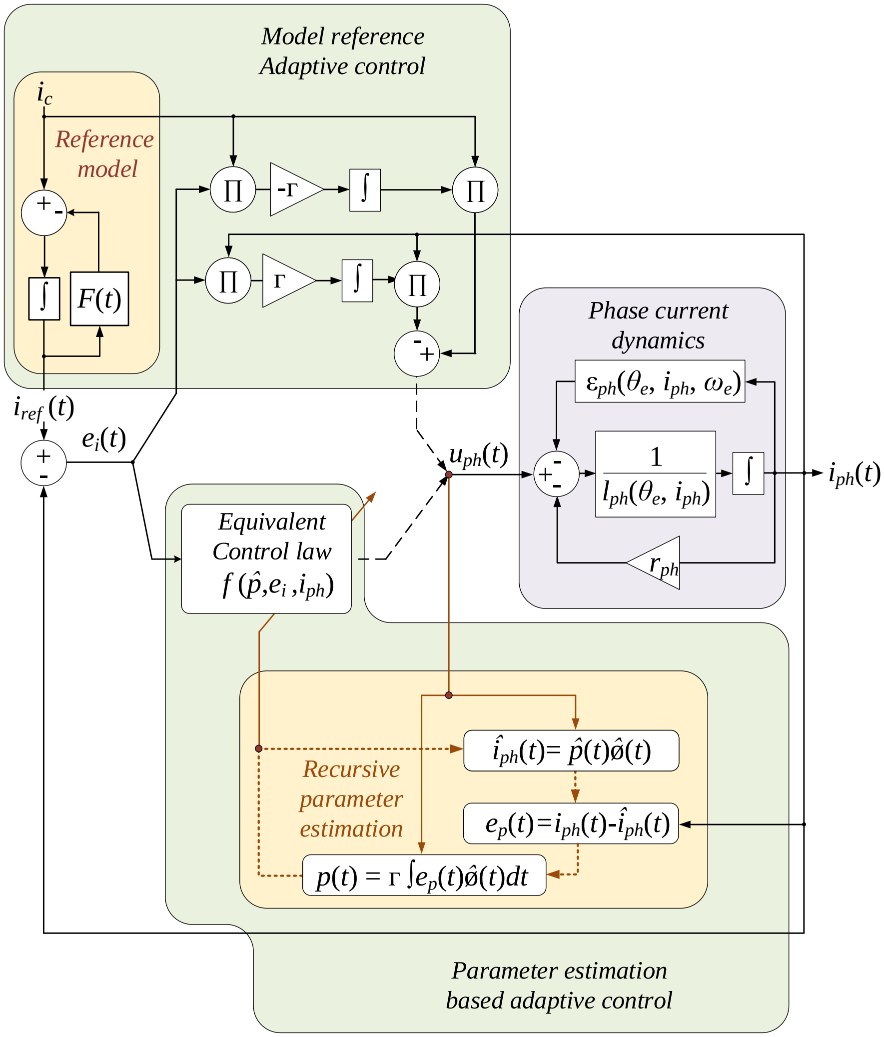

Figure 4.6: Adaptive Control

Lyapunov energy function:

$$\mathscr{V}(k) = \frac{1}{2}\left[e_i^2(t) + (p(t) - \hat{p}(t))^T Q\,(p(t) - \hat{p}(t))\right] \tag{4.32}$$

Where, $Q = \Gamma^{-1} I_{[2\times 2]}$ and the parameter vector becomes,

$$p(t) = \left[F(t) - \frac{r_{ph}}{l_{ph}(\theta_e, i_{ph})} - \frac{1}{l_{ph}(\theta_e, i_{ph})}\frac{dl_{ph}(\theta_e, i_{ph})}{dt} \qquad l_{ph}(\theta_e, i_{ph})\right]^T$$

On the other hand, for an equivalent control law based realisation, the parameter and input vectors are defined according to (4.22). Similar to MRAC, a well justified candidate Lyapunov function: $\mathscr{V}(t) = \dfrac{e_p^2(t)}{2}$ yields following adaptation law:

$$\dot{\hat{p}}(t) = -\frac{\partial \mathscr{V}}{\partial p} = \Gamma e_p(t)\phi(t) \tag{4.33}$$

In both MRAC as well as equivalent control based formulation, the real parameter vectors are highly non-linear functions of time. Therefore, it is very difficult to perform adaptation in $\hat{p}(t)$ with sufficient accuracy. However, for MRAC, any combination of $\hat{p}(t)$ which results into minimisation of $\mathscr{V}$(t) in Eq.(4.32) at a reasonable rate is sufficient. Whereas, the conditions on $\hat{p}(t)$ are more stringent for equivalent control law based realisation since it is required to attain the real values of parameters only. This condition also inevitably calls for sufficient ‘richness’ in the frequency content of the input: $u_{ph}(t)$ [Boyd and Sastry (1986)]. Naturally, it is not possible to satisfy this constraint in every operating condition.

Considering the above discussion, the approach in [Naitoh and Ishikawa (2010)] appears to be more reasonable. However, in equivalent control law based control, the initiation of $\hat{p}(t)$ can be performed in the neighbourhood of the real parameters

Table 4.7: Performance evaluation of adaptive control

Criteria	Mechanism
inductance variation	Inductance LUT and parameter estimation(for equivalent control law) control parameter adaptive (for MRAC)
Induced EMF decoupling	Incorporation of induced emf dynamics in state matrix
compensation of parameter variation	online estimation
Frequency warping effect	rate of adaptation can be optimised to adjust for faster change in parameters.
Memory requirement	Inductance LUT for equivalent control law
Commputational burden	Moderate due to matrix multiplication involved in the parameter adaptation process

where the energy function: Eq.(4.22) is convex. A successful demonstration of this concept using a flux linkage LUT is presented in [Peng *et al.* (2015)]. The overall performance evaluation of adaptive control is presented in Table 4.7. On account of time varying nature of the real parameter vector, assuming the necessary condition on input vector($\dot{\hat{p}}(t) >> \dot{\phi}(t)$) being satisfied, the actual dynamics of the cost function becomes:

$$\dot{J}(t) = -\Gamma e_p^2(t)\phi^2(t) + e_p(t)\dot{p}(t)\phi(t) \tag{4.34}$$

The second term in Eq.(4.34), is the main source of possible deterioration in the control performance. Two possible solutions for this issue are: a) Use of model information for initial value of the parameters and b) Use of higher order model. The former has been successfully implemented in [Peng *et al.* (2015)] with good tracking performance whereas the latter has not been explored yet.

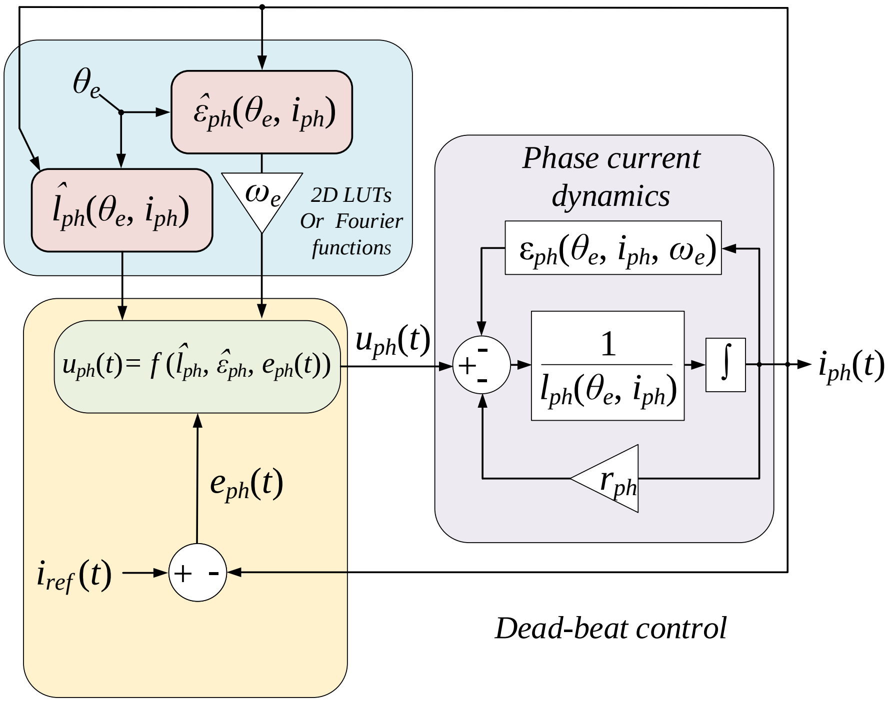

Figure 4.7: Dead-beat control

4.8 Dead-Beat Control

Due to their fast dynamic response and, simple structure, the dead-beat controllers have been widely implemented for current control problems. The major contributions include, predictive: [Ahmad and Narayanan (2018); Mikail *et al.* (2014)] predictive with parameter adaptation [Peng *et al.* (2015)], using iterative learning control [Sahoo *et al.* (2004)] and using torque sharing functions [Zhang *et al.* (2019b)]. A typical application process using dead-beat control is shown in Fig.(4.7).

Except the asymptotic convergence type techniques, the remaining control techniques mentioned in proceeding sections can produce deadbeat type of performance, such as, the LQR/LQG with $R = 0$, [Li and Shamsi (2015a); Zhao *et al.* (2019)]

and sliding mode control with manifold $\sigma(t) = \dot{e}_i(t)$. In a nutshell, the deadbeat control determines the optimum control voltage to achieve the desired current reference within a sampling period using the knowledge of the measured current feedback and available model information.

Intuitively, the very large gain of deadbeat controller makes the control loop highly susceptible to the measurement noise. Use of optimal state estimation becomes very promising in this scenario. Except large magnitude of the gain, the behavior of a dead-beat controller is similar to the previously mentioned control techniques and the performance evaluation can be considered based on the application framework.

4.9 Comparative Analysis of Control Techniques

The analysis of the candidate control techniques presented in previous sections illustrates their operating principles in the context of the performance criterion enlisted in Table 3.1 and provides corresponding elucidations. On account of these discussions, this section presents a comparative analysis of these control techniques adhering to the same evaluation criterion.

As shown in Fig.(4.8), the control techniques with identical design processes and implementation frameworks are grouped on a single spider-plot for comparison. It is worth noting here that the immunity towards measurement noise is not expressed exclusively as a comparison criterion in this section. However, its effect is considered over the attributes: dynamic response consistency, induced EMF decoupling and robustness towards parameter variation. The ratio, switching to electrical frequency: $\frac{\omega_f}{\omega_e}$ essentially expresses the physical implication of the frequency warping effect discussed in Section 3.4.1. The assessment metric for each comparison criterion is kept the same across all the spider-plots shown in Fig.(4.8) enabling uniformity for the purpose of analysis. Thus, all the control techniques shown in Fig.4.8(a-e) can be analyzed in relation to each other. The rest of this section provides a discussion on the comparative analysis of the control techniques.

Fig.(4.8(a)) Shows the comparison among the fixed gain PI, and robust control techniques: H_2 and H_∞. Due to fixed nature of its gain, the PI controller is not capable of maintaining a consistency in the dynamic response. Moreover, its ability to counter the disturbance due to back EMF is also inconsistent across the operating conditions. H_2 and H_∞ demonstrate a trade-off between dynamic response consistency and the ability to reject matched (induced EMF) and mismatched disturbances. As discussed in Section 4.4, the conservative nature of H_∞ design also performs better at higher speed owing to its better disturbance reject ability. Due to the relatively low phase margin, the PI controller alone exhibits the performance inferior in compared to H_2 and H_∞ designs. Whereas, due to implementation simplicity, it has the best computational and memory efficiency.

The use of model information allows dynamic adaptation of the PI controller gain as a function of rotor position. FL control also emulates similar adaptation in the closed loop gain with the help of $\frac{\partial\psi_{ph}}{\partial i_{ph}}$ and $\frac{\partial\psi_{ph}}{\partial\theta_e}\omega_e$ functions introduced in Section 4.3.

Thanks to the integral action, the PI controller provides better noise rejection thus improving the dynamic response, induced EMF decoupling and parameter insensitivity. However, the corresponding drop in phase margin reduces its performance at higher speeds than pole placement design based FL control. Highly parametric nature of the Fourier series functions in FL control demands relatively large processing

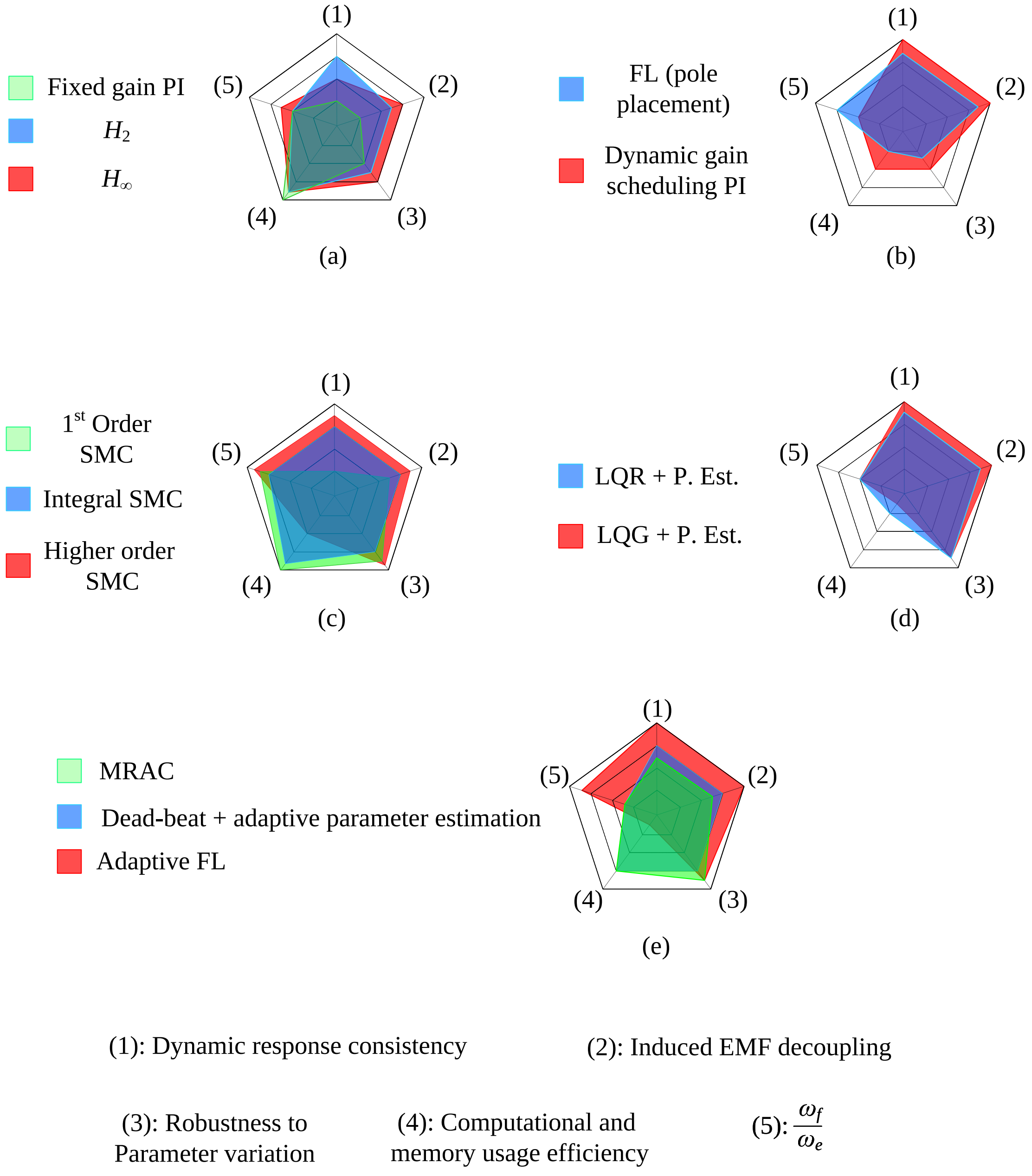

Figure 4.8: Performance comparison of the control techniques

efforts and suffers from performance degradation due to parameter drift.

Sliding mode approach provides the most robust control design among the techniques reviewed in this chapter. Due to its discontinuous switching action, the 1^{st} order sliding mode control exhibits inconsistency in the dynamic response as it is not possible to perform a high-frequency approximation of the disturbances in digital applications. The magnitude of the discontinuous switching function is optimal for the worst-case condition only and hence results in chattering about the sliding surface. Consequently, the phase current also suffers large ripple about the reference. On the other hand, SMC with integral compensation attains a good compromise between corrective and disturbance rejection efforts. However, the integral compensation does not allow finite-time convergence, limiting its performance at higher speeds. Elimination of the discontinuous switching while maintaining a finite time convergence can be achieved with the help of higher-order SMC. However, due to the large computational burden imposed by the calculation of fractional powers of the tracking error, all higher-order SMC designs (≥ 2) suffer from low computational efficiency.

Among the optimal control techniques presented in the literature, the linear regulators with augmented parameter estimation mechanisms have demonstrated excellent tracking performance. As detailed in Section 4.5, both LQR and LQG design approaches discussed in the literature employ 1^{st} order model of phase winding. Due to the time-varying nature of the SRM inductance profile, the parameter estimation mechanism suffers a unit time step delay in estimated parameters resulting in performance degradation at higher speeds. In terms of dynamic response consistency, and disturbance rejection ability, LQG performs better than LQR due to its better noise immunity. On the other hand LQG is more computationally expensive owing to the presence of an optimal state estimator.

As described in Section 4.7, due to fast time-varying nature of 1^{st} order models, the adaptive control becomes very challenging. On the other hand, constant parameter based Fourier series models exhibit slow time varying nature, which is more suitable for adaptive estimation. However, large number of parameters adds to the computational burden and memory usage.

4.10 Summary

This chapter focuses on the important aspects pertaining to fixed switching frequency current control of SRM. The need for high dynamic response due to fast varying current reference command, compensation of nonlinear induced EMF and inductance variation over a conduction period are considered for evaluation of control technique performance. The frequency warping phenomenon is also considered to predict the performance at high speed.

Due to highly nonlinear electromagnetic characteristics of SRM, use of model information in the form of inductance or flux linkage profile for maintaining consistency in dynamic performance is seen prevalent thorough the literature. Similarly, the highly nonlinear induced EMF is compensated for using an induced EMF lookup table. These techniques, although pragmatic, need large storage in micro controller memory and suffer from model mismatch due to interpolation issues as well as variation in the parameters during regular operation. The latter constitutes unmodelled dynamics, the effect of which is also analysed.

On account of this study, the rest of this section, presents several recommendations for further improvement in the performance of the control techniques discussed in this chapter.

4.10.1 Recommendations for Performance Improvement

Non-Linear Modelling

The first order Jacobi linearized model with inductance lookup table based scheduling rely on the assumption that the Euler's approximation of discretization remains fairly accurate. As discussed in Section 3.4.1, the validity of this assumption gradually reduces as a function of speed. This phenomenon is one of the reasons for performance deterioration at high speed. Thus, replacing the constant value of the inductance over a sampling period with a function can potentially improve the performance.

As a consequence of the non-liner modelling, the formulation of LQR/LQG problem becomes more complex and more efficient algorithms for solving the Hamiltonian function Eq.(4.20) deserve further exploration.

For MRAC realisation, the non-linear modelling helps in transformation of SRM model from a 'fast LTV' to a 'Slowly Time Varying(TV)' plant [Tsakalis and Ioannou (1987)]. Although the slowly TV plant has more parameters, their rate of change is slower is comparison to their fast TV counterparts. Greater fidelity can be achieved with higher order parametric functions which yield more numerous and increasingly slower parameters. Considering the exponential rate of rise in the number of calculations to be performed as a function of parameters, a good compromise should be achieved by considering the available processing power and desired control accuracy. A very good demonstration of this principle can be found in [Amor *et al.* (1993)] with FL control.

Digital Sliding-Mode Control

As described in Section 4.6, sliding mode control offers great flexibility in defining the nature of the desired dynamic response. Yet, similar to other techniques, the equivalent control law in sliding mode control can not be realised without model information. For lower fidelity models, the contribution of disturbance rejection term is improved which also results into sub-optimal control performance. A very effective solution to this issue is presented in the form of a 'digital sliding mode control design' in [Drakunov and Utkin (1990)]. Under this approach a part of unmodelled dynamics can be calculated in the form of a unit sample delayed disturbance. Thus, net magnitude of the discontinuous switching term can be greatly reduced.

Hybrid Control Techniques

Although the fixed gain PI control is insufficient in terms of maintaining consistency in dynamic response throughout the conduction period, it is very inexpensive in terms of computation and memory requirement. A combined solution of PI+delta modulation [Gallegos-López and Rajashekara (2002)] have proved to be a practically viable solution. This concept can promisingly yield a more robust controller with incorporation of the principles of sliding mode control in the design process.

Chapter 5

Digital Sliding-Mode Based Robust Model-Free Current Control

5.1 Introduction

In an SRM drive, the efficacy of a control technique operating at a fixed switching frequency is governed by its ability to predict the phase current dynamics and compensation of the corresponding disturbances for at least one sample time step. Due to their highly nonlinear nature, the electromagnetic characteristics of SRM exhibit large variations in dynamic response as a function of operating conditions. Therefore, it becomes necessary to address the following two aspects of control design, viz. robustness to non-linear disturbances and consistency in closed-loop dynamic performance.

Among the current control methods proposed in the literature, the former is ensured via worst-case design [Ahmad and Narayanan (2016)]. At the same time, the latter is addressed by adopting the controller gain using the a-priori knowledge of the electromagnetic model either, in the form of a Fourier series in feedback linearization (FL) [Amor *et al.* (1992); Ilic'-Spong *et al.* (1987); Panda and Dash (1996)], inductance LUT based dynamic gain scheduling [Hannoun *et al.* (2011b); Lin *et al.* (2010); Schulz and Rahman (2003)] or flux-linkage LUT [Mikail *et al.* (2014); Peng *et al.* (2016)]. Evidently, these techniques are susceptible to modeling errors. To improve the robustness of these techniques, the effect of inexact pole-zero cancellation in dynamic gain scheduling is compensated by using an additional discontinuous switching control action [Shang *et al.* (2009); Ye *et al.* (2015)] as well as online model adaptation [Namazi *et al.* (2016); Peng *et al.* (2016)].

Several intelligent control designs include fuzzy logic [Chowdhuri *et al.* (2006); Wang and Liu (2011)], and data-driven algorithms such as artificial neural networks [Karakas and Vardarbasi (2007)] and iterative learning control [Sahoo *et al.* (2005)] where the model information is generated via online training. Although these techniques are pragmatic, it is not easy to evaluate their stability and ensure reliable tracking performance in every operating condition. Moreover, a considerable memory is required to store the model information.

The optimal control approach has recently been successfully utilized to realize the current controller with excellent tracking performance [Alharkan *et al.* (2020); Li and Shamsi (2015b)]. The effect of modeling error on control performance is reportedly reduced through the augmentation of an online parameter estimator. However, the algorithms employed for the identification of the solution to the nonlinear optimal control problem are of iterative nature which imparts high computational cost along with considerable memory needed for the storage of model information.

Compared to the linear pole placement approach, The sliding mode control design provides greater flexibility in terms of dynamic response shaping. For fixed switching frequency PWM application, an integral sliding mode control design is presented in [Ye *et al.* (2015)], where the identification of desired dynamics is entirely performed online with model information. A higher-order sliding mode has been implemented for torque control in [Sun *et al.* (2020b)], where the direct instantaneous control is realised yielding a variable switching frequency. A second order sliding mode control is implemented in [Ben Salem *et al.* (2020)] only for speed control which is significantly slower compared to current control.

In summary, the effective fixed switching current control strategies presented in the literature for SRM drives utilize the knowledge of electromagnetic model information aided by online parameter estimation for robust tracking performance. The most prominent drawbacks of these methods are the significant microprocessor memory requirement and high computational burden.

In a practical SRM drive, considering the contribution of the voltage distortion due to the power converter nonlinearity and measurement noise, the electromagnetic model of the phase winding can be characterized as a nonlinear stochastic system. Along with the nonlinearities in the phase current dynamics, the aforementioned quantities can be treated in a lumped form as one or more extended states. The advantages of this approach are twofold, viz. the combined effort of identification and utilization of model information is saved and the effect of disturbances inherent to a practical drive system is also accounted for [Spall and Cristion (1998)]. Thus, robust control can be realized if accurate knowledge of this extended state is available. This approach, popularly known as disturbance rejection control, has found successful applications in induction [Alonge *et al.* (2017)] as well as synchronous machines [Sira-Ramírez *et al.* (2014)].

In light of this discussion, a digital sliding mode control [Utkin and Drakunov (1989)] is investigated in this chapter for fixed switching frequency current control of SRM drives. Initially, an extended state model of phase current dynamics is developed by defining the nonlinear phase current dynamics of SRM in the form of an unknown extended state. Subsequently, an equivalent control law is derived for maintaining the closed-loop dynamics in the subspace closed to the sliding surface. For this purpose, the estimation of the extended state is performed using a delayed-disturbance approximation [Wu-Chung Su *et al.* (2000)]. To alleviate the effect of deterioration in control performance due to inexact compensation of the extended state, an auxiliary control law is developed via Lyapunov stability analysis. The effectiveness of the proposed control technique is validated with the help of simulation study in MATLAB/Simulink® environment as well as over experimental test setup.

5.2 Extended State Model of SRM

A linearized version of SRM current dynamics is obtained by splitting it into its linear and nonlinear components as described by the following equations.

$$\dot{i}_{ph}(t) = -r_{ph}l_{ph}(\theta_e, i_{ph})^{-1}i_{ph}(t) + l_{ph}(\theta_e, i_{ph})^{-1}(u_{ph}(t) - \epsilon_{ph}(t)) + \zeta(t) \tag{5.1}$$

As shown in Fig.(5.1), the inductance profile is a function of rotor electrical position (θ_e) and phase current. From Eq.(5.1), the linearized current dynamics with extended

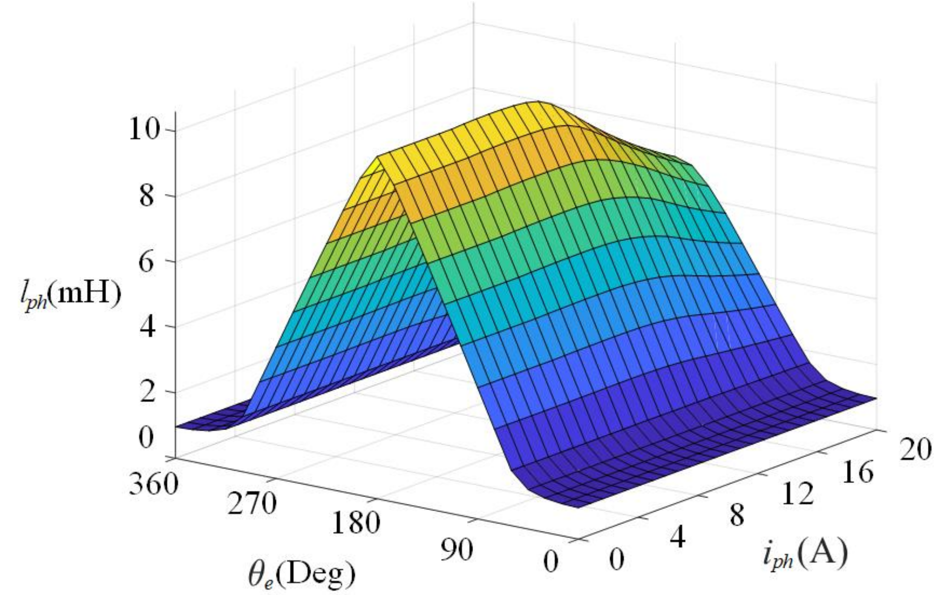

Figure 5.1: SRM phase inductance profile

state are derived as,

$$\dot{i}_{ph}(t) = hu_{ph}(t) + f_{ph}(t) \tag{5.2}$$

Where, h represents the reference model, and $f_{ph}(t)$ stands for the extended state, encapsulating the model nonlinearities. For the sake of simplicity in analysis, the effect of $\zeta(t)$ is neglected in the derivation of Eq.(5.2). Subsequently, the dynamic equation of extended state in continuous-time domain is obtained from Eq. (5.1) and (5.2) as,

$$f_{ph}(t) = g_{ph}(\theta_e, i_{ph})u_{ph}(t) - l_{ph}(\theta_e, i_{ph})^{-1}(r_{ph}i_{ph}(t) + \epsilon_{ph}(t)) \tag{5.3}$$

where, $g_{ph}(\theta_e, i_{ph})$ is related to $l_{ph}(\theta_e, i_{ph})$ and h via following equation:

$$l_{ph}(\theta_e, i_{ph})^{-1} = g_{ph}(\theta_e, i_{ph}) + h \tag{5.4}$$

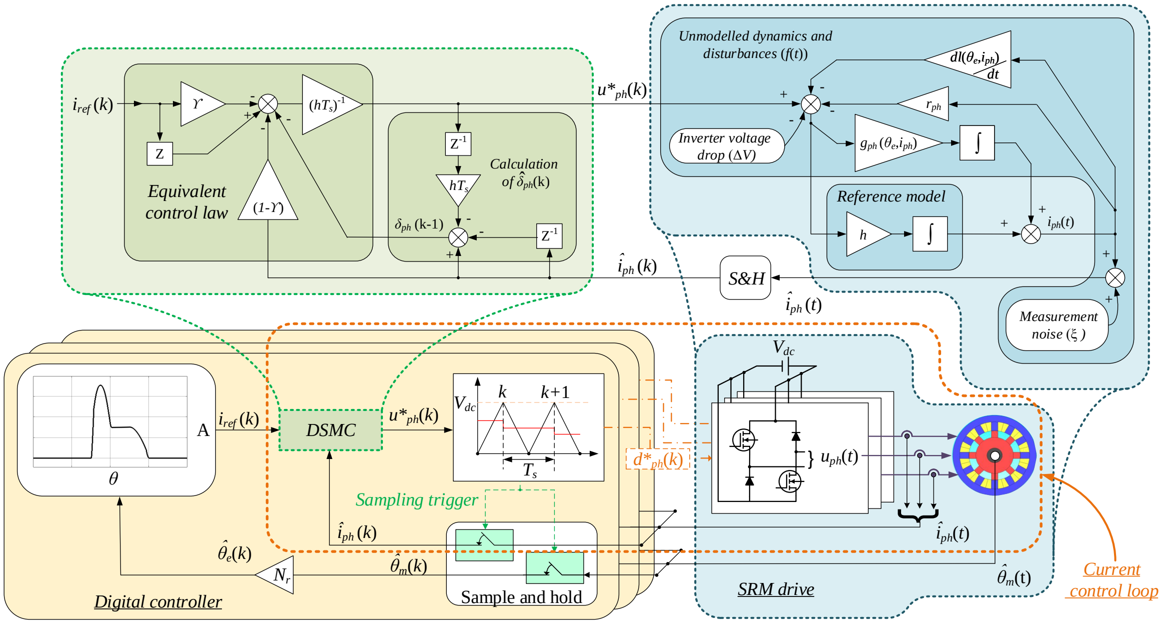

Figure 5.2: Closed-loop current control of SRM drive using delayed-disturbance based digital sliding mode control

Since the controller output voltage remains constant over a sampling period (T_s), a discretized version of Eq.(5.2) is obtained as follows:

$$i_{ph}(k+1) = i_{ph}(k) + hT_s u_{ph}(k) + \delta_{ph}(k) \tag{5.5}$$

Where,

$$\delta_{ph}(k) = \int_{kT_s}^{(k+1)T_s} f_{ph}(t)dt \tag{5.6}$$

Throughout the analysis presented in this chapter, the integral expansion is performed by 1^{st} order (Euler) approximation, leading to the following equation of extended state in discrete-time domain.

$$\delta_{ph}(k) = g_{ph}(k)u_{ph}(k)T_s - i_{ph}(k)\left(\frac{r_{ph}}{l_{ph}(k)} + \frac{1}{l_{ph}(k)}\frac{dl_{ph}(k)}{d\theta_e}\omega_e\right)T_s \tag{5.7}$$

Where, T_s and ω_e represent sampling time and rotor electrical speed respectively. In a sampling instant k, the extended state $\delta_{ph}(k)$ emulates the non-linear variation in dynamic response through $g_{ph}(k)T_s$, while the process disturbance as well as time constant variation are represented by $\left(\frac{r_{ph}}{l_{ph}(k)} + \frac{1}{l_{ph}(k)}\frac{dl_{ph}(k)}{d\theta_e}\omega_e\right)T_s$.

5.3 Digital Sliding Mode Control

5.3.1 Equivalent Control Law

Since the relative degree of the dynamic model described by Eq. (5.1) and Eq.(5.5) is one, the desired dynamics of reference current tracking error: $e_i(t)$ can be defined in the form of a first order sliding surface: $\sigma(t)$ as shown below.

$$\sigma(t) = \dot{e}_i(t) + \gamma' e_i(t) \quad ; \quad \gamma' > 0 \tag{5.8}$$

Where γ' represents the desired rate of convergence. For application in a digital controller, the discrete-time domain equivalent of $\sigma(t)$ is derived as [Utkin and Drakunov (1989)],

$$\sigma(k) = \int_{(k-1)T_s}^{kT_s} \sigma(t)dt \approx e_i(k) - \gamma e_i(k-1) \quad ; \quad \gamma = (1 - \gamma' T_s) \tag{5.9}$$

Intuitively, the choice of γ is can be performed as a trade-off between the corrective effort and noise sensitivity. It is worth noting here that the reference current profile is a smooth continuous function of time having magnitude zero in the beginning of the conduction period. Moreover, in practical situations, it is desirable to have torque response as a smooth asymptotic function varying at a specific fixed rate to avoid excessive stress on mechanical structure. This is ensured by a applying the torque references through either first or second-order filters eliminating the possibility of discontinuous variation in the reference current profile, popularly known as set-point jump [Han (2009)]. Therefore, additional considerations of reaching phase in the design of control law can be neglected conveniently.

In the control problem discussed in this paper, the real challenge is to maintain $\sigma(k+1) = 0$ amid unknown dynamics of $\delta_{ph}(k)$. In an ideal case, if full information of $\delta_{ph}(k)$ is available, an equivalent control law can be derived as follows:

$$u_{ph}(k) = (hT_s)^{-1}(i_{ref}(k+1) - i_{ph}(k) - \gamma e_i(k) - \delta_{ph}(k)) \tag{5.10}$$

Due to the unavailability of exact information of $\delta_{ph}(k)$, the realization of Eq.(5.10) in real-time becomes impossible. Unlike continuous-time domain sliding mode control, the compensation of $\delta_{ph}(k)$ can not be realized with the help of high frequency switching in the discrete-time domain. Amongst the available solutions in the literature, the most basic approach consists of delayed disturbance approximation [Wu-Chung Su *et al.* (2000)] where the estimate of disturbance $\hat{\delta}_{ph}(k)$ at current sampling instant is obtained by a unit sample delayed approximation:

$$\hat{\delta}_{ph}(k) \approx \delta_{ph}(k-1) \tag{5.11}$$

Where the delayed disturbance $\delta_{ph}(k-1)$ is estimated from the measured quantities in successive sampling instances as,

$$\delta_{ph}(k-1) = i_{ph}(k) - i_{ph}(k-1) - hT_s u_{ph}(k-1) \tag{5.12}$$

Thus, the equivalent control law (Eq.(5.10)) is modified as,

$$u_{ph}(k) = (hT_s)^{-1}(i_{ref}(k+1) - i_{ph}(k) - \gamma e_i(k) - \hat{\delta}_{ph}(k)) \tag{5.13}$$

The closed-loop current control realization of SRM using Eq.(5.10) is shown in Fig.(5.2).

5.3.2 Control Performance and Stability Analysis

The equivalent control law, Eq.(5.10), attempts to achieve the collapse of the closed-loop dynamics to $\sigma(k)$ by online compensation of the extended state: $\delta_{ph}(k)$. Considering $\delta_{ph}(k)$ as input, the closed-loop dynamics are represented as,

$$\begin{aligned}\begin{bmatrix} i_{ph}(k+1) \\ u_{ph}(k+1) \end{bmatrix} &= \begin{bmatrix} 1 & hT_s \\ -\dfrac{(1-\gamma)}{hT_s} & -(1-\gamma) \end{bmatrix} \begin{bmatrix} i_{ph}(k) \\ u_{ph}(k) \end{bmatrix} \\ &+ \begin{bmatrix} 0 & 0 & 1 \\ \dfrac{1}{hT_s} & -\dfrac{\gamma}{hT_s} & -\dfrac{2-\gamma}{hT_s} \end{bmatrix} \begin{bmatrix} i_{ref}(k+2) \\ i_{ref}(k+1) \\ \hat{\delta}_{ph}(k) \end{bmatrix}\end{aligned} \tag{5.14}$$

Eq.(5.14) dictates that, with accurate estimation of $\delta_{ph}(k)$, the equivalent control law is capable of maintaining the closed-loop poles at 0, γ and remains unaffected by the choice of h. However, due to the approximation in Eq.(5.11), the closed-loop dynamics differ from Eq.(5.14) and takes the following form.

$$\begin{bmatrix} i_{ph}(k+1) \\ u_{ph}(k+1) \end{bmatrix} = A \begin{bmatrix} i(k) \\ u_{ph}(k) \end{bmatrix} + B \begin{bmatrix} i_{ref}(k+2) \\ i_{ref}(k+1) \end{bmatrix} \tag{5.15}$$

Where,

$$A = \begin{bmatrix} 1 - \left(\dfrac{r_{ph}}{l_{ph}(k)} + \dfrac{1}{l_{ph}(k)} \dfrac{dl_{ph}(k)}{d\theta_e} \omega_e \right) T_s & \dfrac{T_s}{l_{ph}(k)} \\ -\dfrac{1-\gamma}{hT_s} + \dfrac{2-\gamma}{hT_s} \left(\dfrac{r_{ph}}{l_{ph}(k)} + \dfrac{1}{l_{ph}(k)} \dfrac{dl_{ph}(k)}{d\theta_e} \omega_e \right) T_s & -(1-\gamma) - (2-\gamma) \dfrac{g_{ph}(k)}{h} \end{bmatrix}$$

and

$$B = \begin{bmatrix} 0 & 0 \\ \dfrac{1}{hT_s} & -\dfrac{\gamma}{hT_s} \end{bmatrix}$$

The eigenvalues of the closed-loop system Eq.(5.15) displace from their ideal position as a function of the operating point, as shown in Fig.(5.3). In the worst case condition (3000RPM, $\theta_e = 72^o$), the closed-loop control remains stable for $h = 0.1$. However, it fails to maintain $\sigma(k) = 0$. A Similar effect can be observed at lower speed (500RPM) with reduced deterioration in control performance due to the lower magnitude of the induced EMF.

5.3.3 Identification of Reference Model

As demonstrated earlier, due to inexact compensation of $\delta_{ph}(k)$, the closed-loop dynamics under the equivalent control law, Eq.(5.13) no longer remain unaffected by choice of the reference model: h. As described in Eq.(5.15), the magnitude of h essentially influences the control efforts. Hence, it is important to approach its design from the stability point of view.

Fig.(5.4) shows the displacement in the closed-loop poles as a function of h for $\theta_e = 0^o$ at 3000RPM mechanical speed. Evidently, the control effort is large for smaller magnitude of h and vice-versa. For $h < 500$, the phase current suffers large oscillations and the closed-loop system operates dangerously close to instability. On the other hand, for $h > 1000$, the dynamics response is very slow. Thus, a trade-off is made by identifying the optimum magnitude of h for which the closed-loop poles are placed at the closest possible locations from the ones defined by the sliding surface.

In a physical sense, this choice also mandates that the value of inductance assumed in the reference model be smaller than the smallest value of the phase inductance, $l_{ph}(\theta_e = 0^o)$. Hence dictating a pessimistic estimate of the control effort. At the same time, the lower limit of h is constrained by desired dynamic response and closed-loop stability.

5.3.4 Sliding Surface Dynamics Under Inexact Compensation of Extended State

Due to the delayed disturbance approximation as given in Eq.(5.11), the sliding mode can only exist within a boundary layer of magnitude $\sigma(k)$ also known as existences subspace determined as:

$$|\sigma(k)| = |\delta_{ph}(k) - \delta_{ph}(k-1)| \tag{5.16}$$

The estimation of $\hat{\delta}_{ph}(k)$ is also highly affected by current measurement noise. Therefore, it is not recommended to utilize the value of estimated $\delta_{ph}(k)$ fully. In the

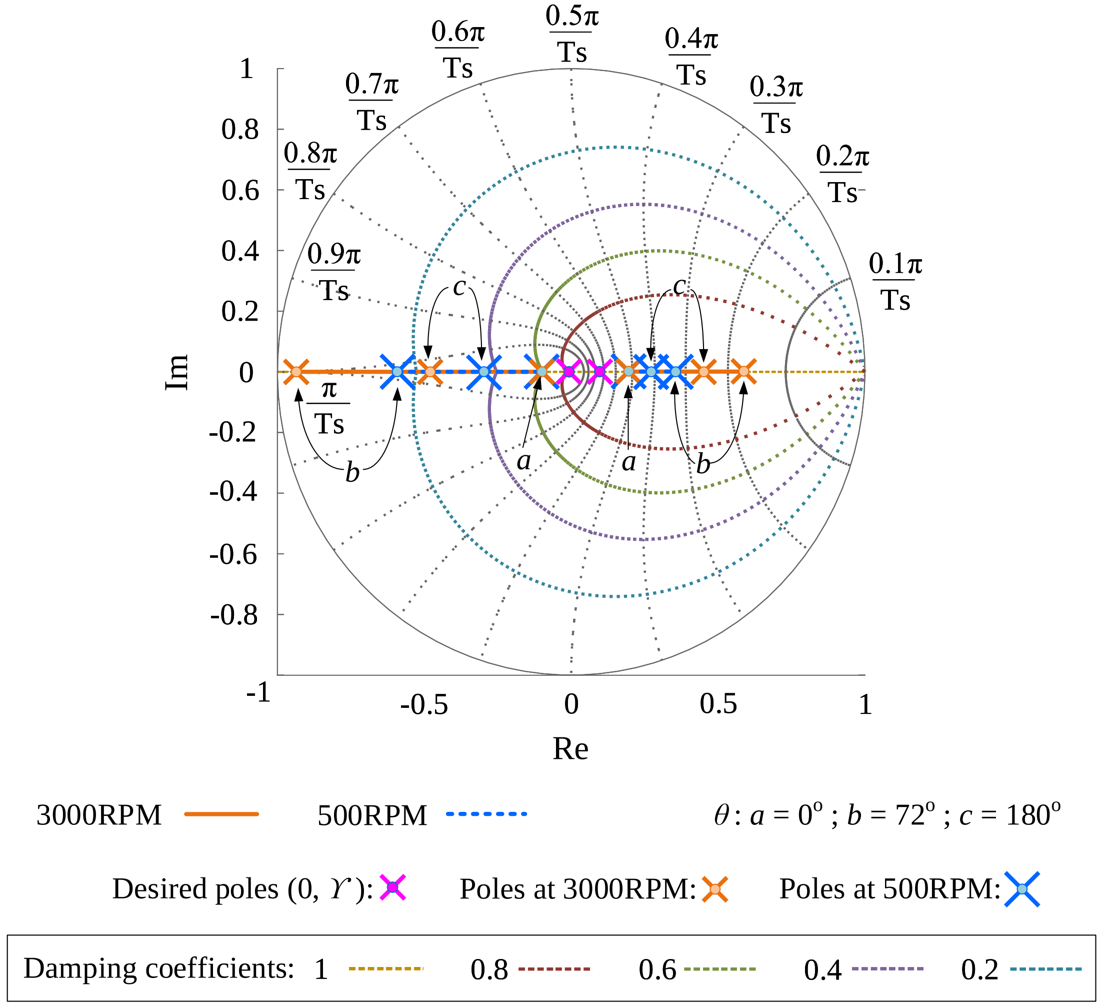

Figure 5.3: Closed-loop dynamics with delayed disturbance compensation: Variation in the eigenvalues due to change in operating condition at $h = 0.1$

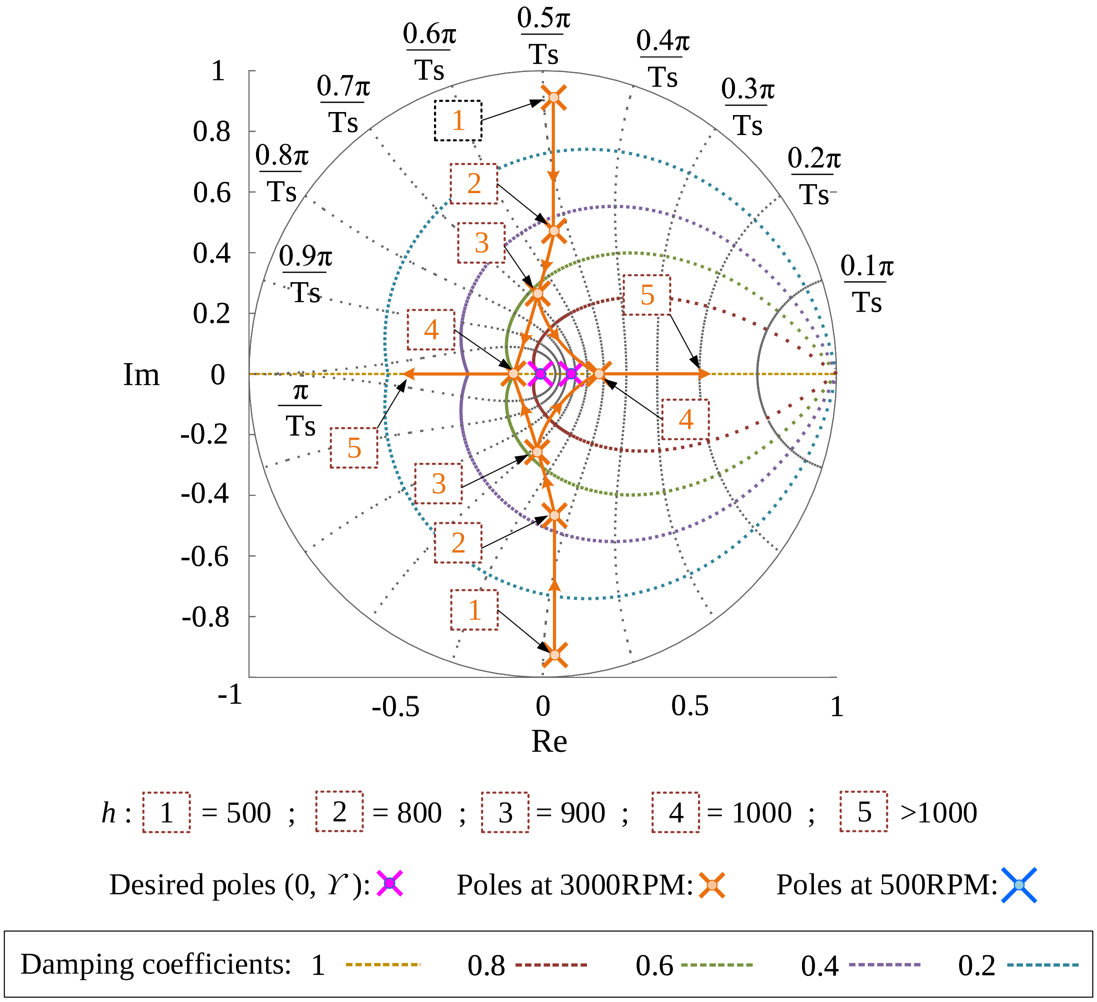

Figure 5.4: Closed-loop dynamics with delayed disturbance compensation: Variation in eigenvalues as a function of h at $\theta = 0^o$ and 3000RPM

presented study, a fraction $\mu\hat{\delta}_{ph}(k)$ is used where the value of $\mu(< 1)$ is determined experimentally. Although this provision helps to achieve improved robustness towards measurement noise, it also exacerbates the effect of inexact compensation, further widening the existence subspace.

In the view of above discussion, an auxiliary control voltage term is introduced in the equivalent control law, Eq.(5.13) as,

$$u_{ph}(k) = (hT_s)^{-1}(i_{ref}(k+1) - i_{ph}(k) - \gamma e_i(k) - \mu\delta(k-1) + v_{comp}(k)) \tag{5.17}$$

The control voltage component $v_{comp}(k)$ is introduced for minimisation of the magnitude: $|\delta_{ph}(k)|$ resulting from inexact compensation of $\hat{\delta}(k)$. The composition of $v_{comp}(k)$ is determined via Lyapunov stability analysis presented in the next section.

5.4 Identification of Auxiliary Controller via Lyapunov Stability Analysis

The necessary conditions for ensuring the stability of the control law, Eq.(5.17) are determined by evaluating the candidate Lyapunov energy function: $\mathscr{V}(k) = \dfrac{\sigma^2(k)}{2}$. For this purpose, a 1^{st} order derivative of $\sigma(k)$, is defined as,

$$\dot{\sigma}(k) = \frac{\sigma(k+1) - \sigma(k)}{T_s} \tag{5.18}$$

To ensure a stable performance, the necessary rate of descend for $\mathscr{V}(k)$ is defined via following negative semi-definite function.

$$\dot{\mathscr{V}}(k) \leq -\frac{\alpha}{\sqrt{2}}|\sigma(k)| \tag{5.19}$$

Using Eq.(5.9) and Eq.(5.19), $v_{comp}(k)$ can be obtained by solving following inequality,

$$\begin{aligned} -\frac{\alpha}{\sqrt{2}}|\sigma(k)| &\geq \sigma(k)\dot{\sigma}(k) \\ = \frac{\sigma(k)}{T_s}&\left[\mu\delta_{ph}(k-1) - \delta_{ph}(k) - v_{comp}(k) - \sigma(k)\right] \end{aligned} \tag{5.20}$$

Eq.(5.20) reveals that, stability can be ensured by defining the compensation voltage as, $v_{comp}(k) = v_{1comp}(k) + v_{2comp}(k)$, Where,

$$v_{1comp}(k) = \sigma(k)$$
$$v_{2comp}(k) = Jsign(\sigma(k))$$

The magnitude (J) of the discontinuous switching function, $v_{2comp}(k)$ is determined by following inequality,

$$J \geq \frac{\alpha}{\sqrt{2}} + \frac{\delta_{ph}(k) - \mu\delta_{ph}(k-1)}{T_s} \tag{5.21}$$

Where, a conservative bound 'L' is defined as.

$$L = \left\| \frac{\delta_{ph}(k) - \mu\delta_{ph}(k-1)}{T_s} \right\|_{\infty} \tag{5.22}$$

It is possible to predict the sign of L as a function of tracking error and reference current dynamics. However, in the presented study, it was found that it is not necessary

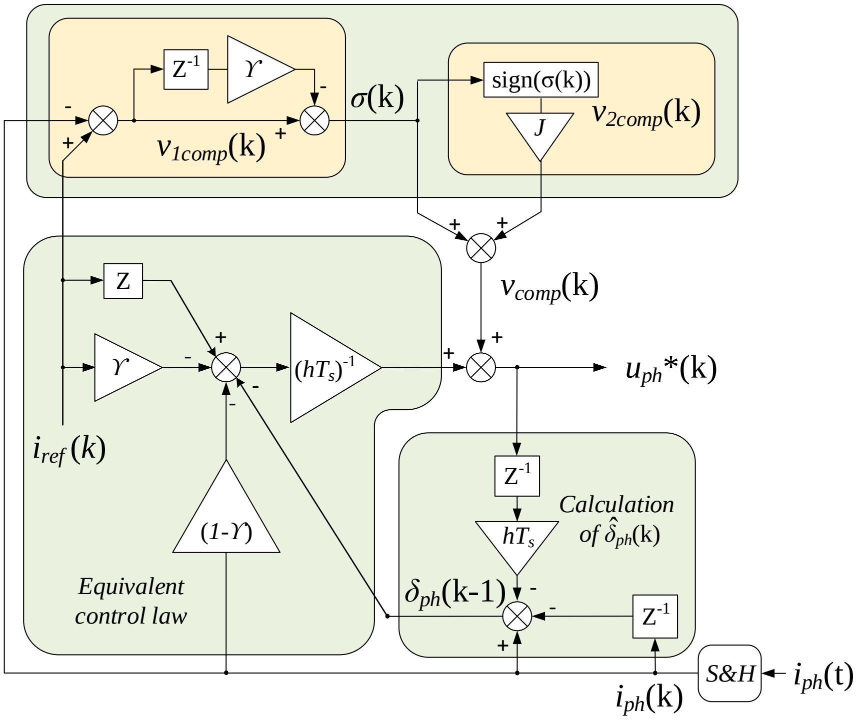

Figure 5.5: Control logic with compensation

for large enough value of α. Thus, the magnitude of J is determined as,

$$J \geq \frac{\alpha}{\sqrt{2}} + L \tag{5.23}$$

The complete structure of the proposed controller is shown in Fig.(5.5).

5.5 Simulation and Experimental Study

In practice, the control is implemented using a digital signal processor operating at a finite sampling frequency. During PWM implementation, the control voltage calculated from quantities sampled in an instant, can only be applied in a successive

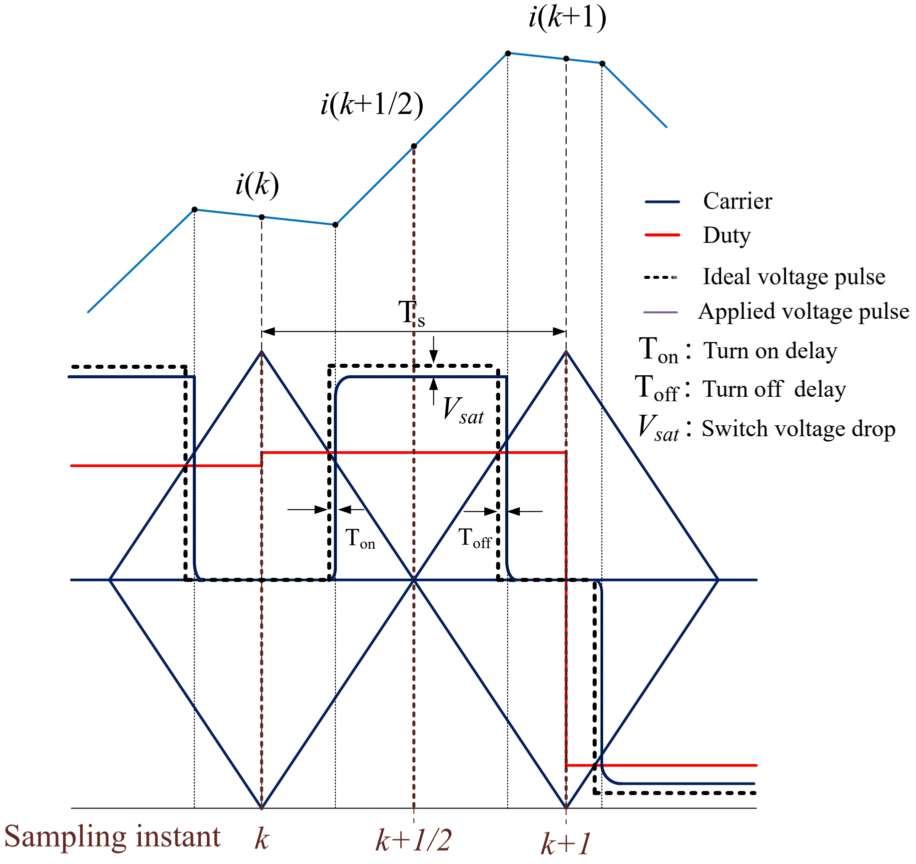

Figure 5.6: PWM implementation

instant due to considerable calculation delay in the processor. This phenomenon known as PWM delay has been investigated thoroughly for SRM drives. In [Blaabjerg *et al.* (1999)], it was demonstrated that the effect of PWM delay can be reduced by performing current sampling at the middle of the PWM period. In this case, the current sampled at $(k+1)^{th}$ sampling instant is approximated by a sample at $(k+1/2)^{th}$ instant. This is achieved by implementing the control routine at twice the frequency of the PWM carrier frequency and performing sampling and duty ratio update at alternate instances as shown in Fig.(5.6). This technique helps halve the PWM delay and provides a half of the PWM period for calculation of control voltage.

Parameter	Value
winding resistance	0.5Ω
dc link voltage	100V
switching frequency	10kHz
sampling frequency	20kHz
rated speed	2500RPM
no. of phases	3
peak phase current	21A
stator poles/phase	4

Table 5.1: parameters of SRM drive

In the presented study, the above discussed PWM compensation technique is utilized to implement the proposed control law. Soft chopping is implemented using phase opposed carriers to obtain PWM pulses corresponding to +Ve and -Ve duty ration at a fixed switching frequency as shown in Fig.(5.6).

At sampling instant k, the current reference at $k+1$ is derived by approximately predicting the rotor position as [Peng *et al.* (2016)]:

$$\theta_e(k+1) \approx \theta_e(k) + \omega_e(k)T_s$$

Where, $\omega_e(k)$ represents rotor electrical speed at a sampling instant, k.

5.5.1 Simulation Study

The simulation study for a 12/8 SRM is performed in Matlab/Simulink® environment. The machine model consists of a flux linkage profile generated from FEA electromagnetic analysis. This profile is used to emulate the electromagnetic behaviour of the experimental SRM. The drive parameters used in the simulation study

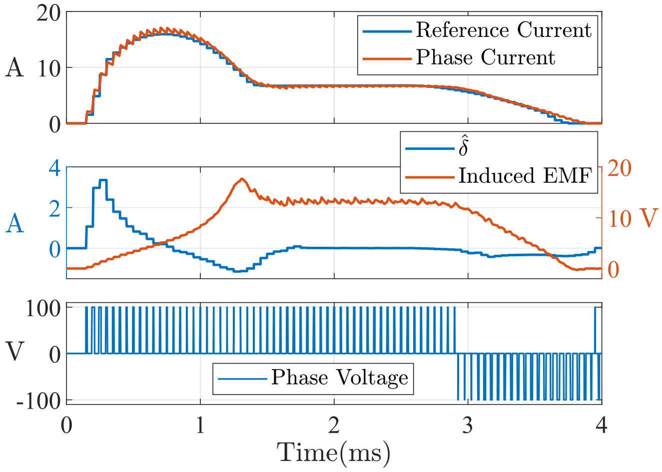

Figure 5.7: Simulation Study: Reference current tracking performance at 500RPM

are shown in Table 5.1.

The reference current profile is generated using a cubic torque sharing function applied over a static torque characteristics also generated using FEA.

The dynamic simulation study is performed for the reference current profile generated for 1Nm torque. Fig.(5.7) and Fig.(5.8) shows the current tracking performance of the proposed controller for a low speed of 500RPM and base speed (2500RPM) respectively. The controller parameters are presented in Table 5.2. $\hat{\delta}_{ph}(k)$ attains large magnitudes as well as undergoes greater variations in the beginning of the conduction period. This is mainly due to fast dynamic changes in reference profile instigating large dynamic variations in controller output voltage. In the middle of the conduction period, the constant nature of the reference profile and the induced EMF allows $\delta_{ph}(k-1) = \delta_{ph}(k)$. Thus, the equivalent control law is sufficient to maintain a low steady state-error. Since $\mu < 1$, a small magnitude of J is necessary. At the base speed, large magnitude of $\sigma(k)$ is caused due to, greater magnitude of induced EMF,

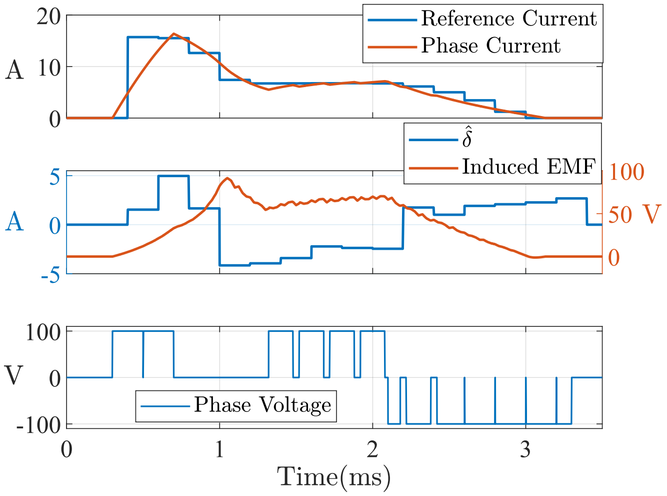

Figure 5.8: Tracking performance at 2500RPM

reduced number of sampling and switching instances per conduction period as well as faster variations in reference profile. Therefore, the significance of $v_{comp}(k)$ is larger at base speed.

5.5.2 Experimental Study

The experimental verification of the proposed controller is performed using a back-to-back coupled dyno-motor setup shown in Fig.(5.9). In the setup, the dyno consists of a 5kW 3-ph IPMSM driven by an IGBT inverter. The experimental 12-8 SRM under

Parameter	Value
h	0.1
γ	0.05
μ	0.7
J	5

Table 5.2: Controller parameters

test is driven by an asymmetric bridge power converter supplied by a 100V DC power supply. A Texas Instruments F28377D floating point DSP operating at 200MHz clock frequency is used for controlling the SRM drive. Similar to the simulation study, a reference current profile with peak value of 4A generated using a cubic torque sharing function implemented over a wide conduction period (5^o to 170^o electrical) is used as reference to obtain a comprehensive evaluation of the control performance.

As shown in the inductance profile in Fig.(5.1), for the test SRM, the effect of saturation at rated current is not significant. Since online estimation of the extended state is involved, a low magnitude highly dynamic reference current profile pose greater challenge due to its low signal to noise ration (SNR).

The control performance of the proposed SMC is shown in Fig.(5.10) and Fig.(5.11). Thanks to online identification of $\hat{\delta}_{ph}(k)$, and the auxiliary control action, the proposed control law is capable of effectively rejecting the disturbances due to all the unmodelled dynamics. Moreover, a single combination of the control parameters shown in Table 5.3 is found to be sufficient to obtain a good tracking performance. As described earlier, the calculation of $\delta_{ph}(k)$ is highly influenced by the effect of measurement noise. This effect is more significant when the current sample is obtained at the middle of the voltage pulse or $(k+1/2)^{th}$ sampling instant as shown in Fig.(5.6).

Parameter	Value
h	0.15
γ	0.05
μ	0.6
J	7

Table 5.3: Controller parameters used in experimental study

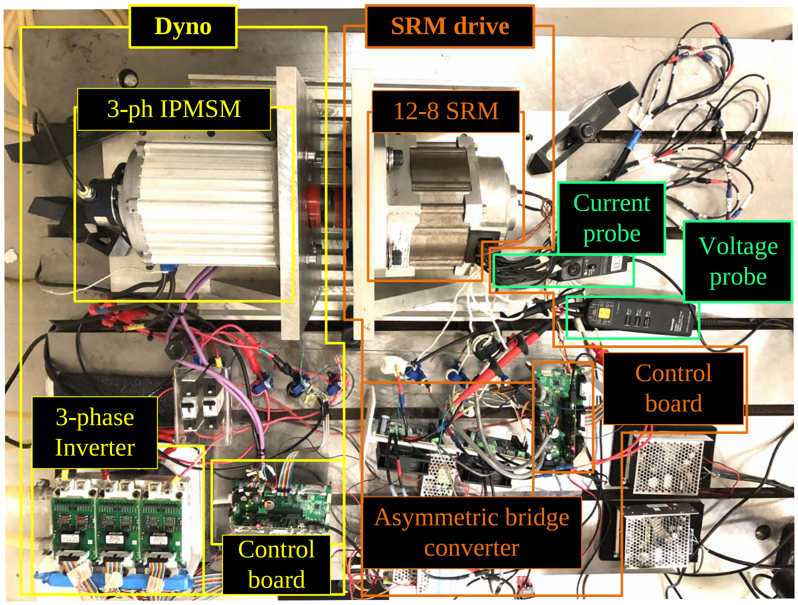

(a) Top view

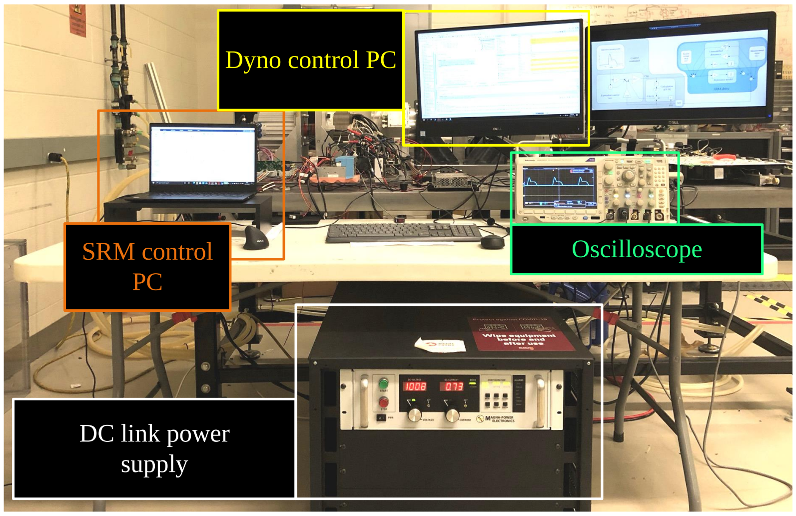

(b) Front view

Figure 5.9: Experimental Setup

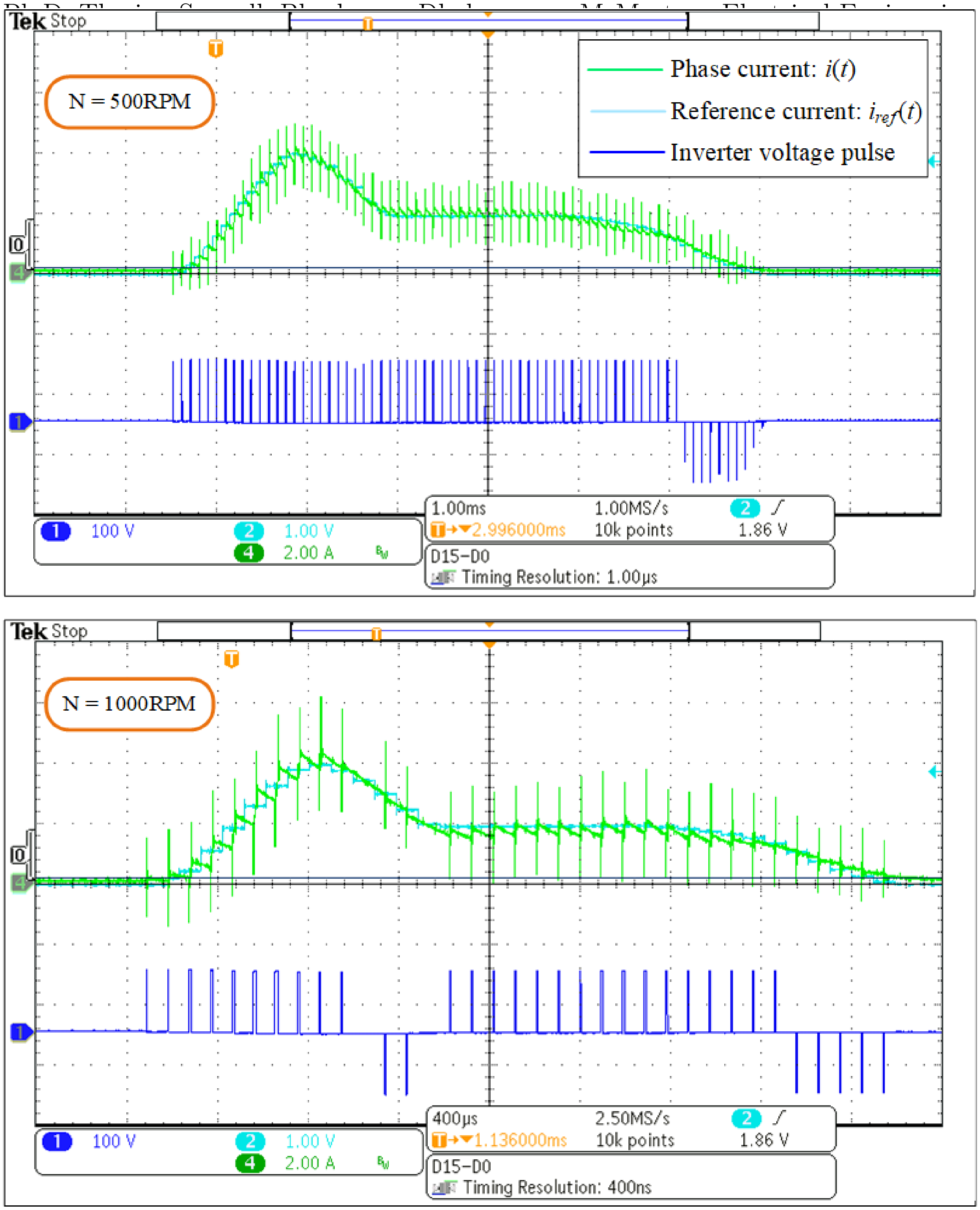

Figure 5.10: Experimental validation of reference current tracking performance with proposed control law(1)

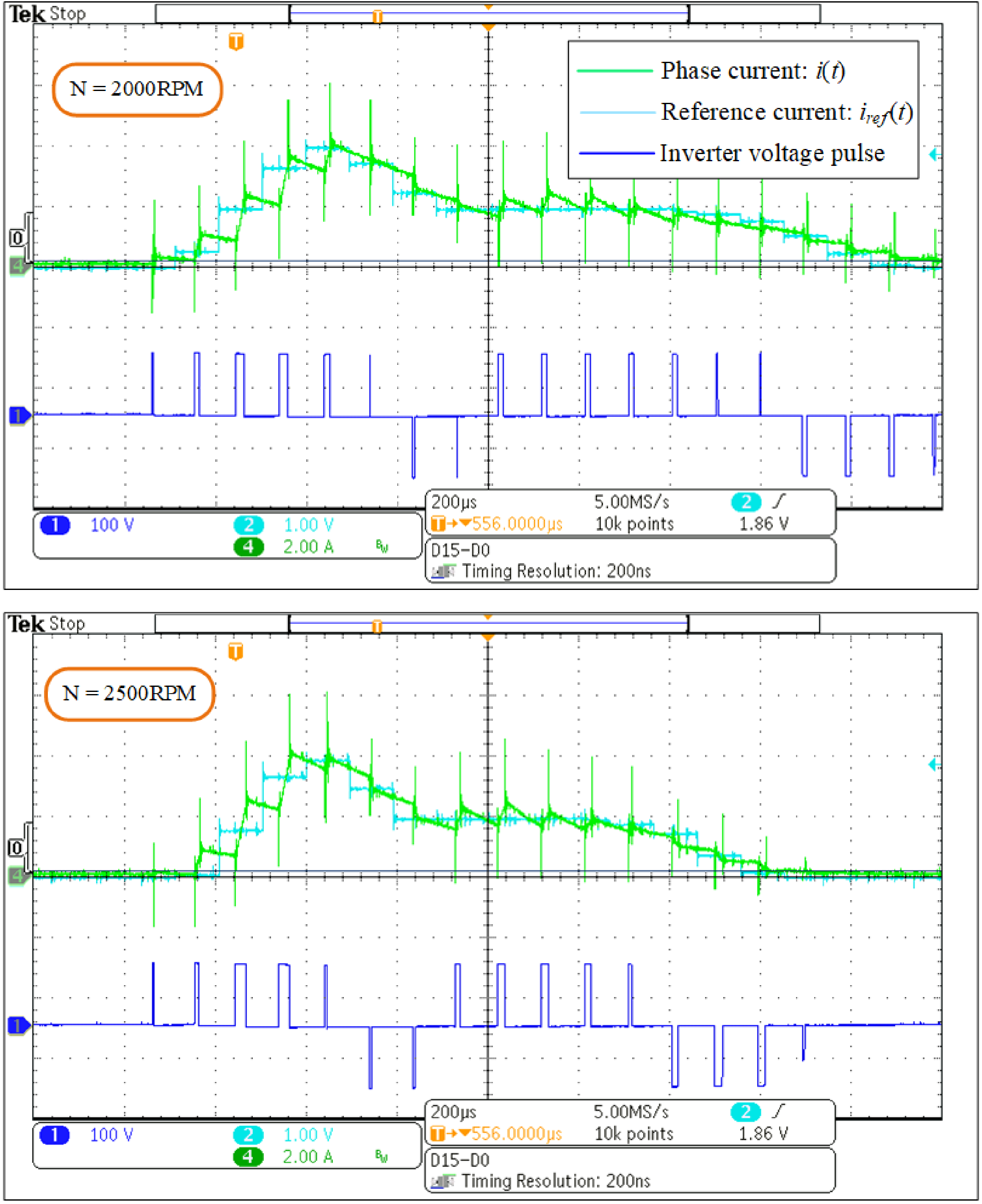

Figure 5.11: Experimental validation of reference current tracking performance with proposed control law(2)

This effect can be partially reduced by using the current sample at k^{th} instant instead of $(k-1/2)^{th}$ for calculation of $\hat{\delta}_{ph}(k)$. This provision also help reduce the effect of sampling delay on estimation of $\hat{\delta}_{ph}(k)$.

5.6 Comparative Analysis

The current tracking performance of the proposed DSMC based model-free current controller is compared with two other controller types viz,

1 Dynamic gain scheduling PI

2 Model aided Sliding Mode Controller (SMC)

The current tracking performance of all three controllers is evaluated in a comparative analysis in the form of RMS error calculated as,

$$RMSE = \sqrt{\frac{\sum_i^n (i_{ph}(i) - i_{ref}(i))^2}{n}} \tag{5.24}$$

Where, n represents total number of recorded samples and i represents the sample index.

The RMSE comparison is performed for 3 speed points shown in Fig.(5.12). The results of this study are shown in Fig.(5.13). The Comparison is also performed between model aided SMC and proposed DSMC for step change in the reference torque. As shown in Fig.(5.14), the proposed DSMC exhibits similar current reference tracking performance as model aided SMC. The maximum rates of change of the phase currents are limited by the peak phase voltage limit. Considering this limit, both the controllers exhibit high current tracking accuracy.

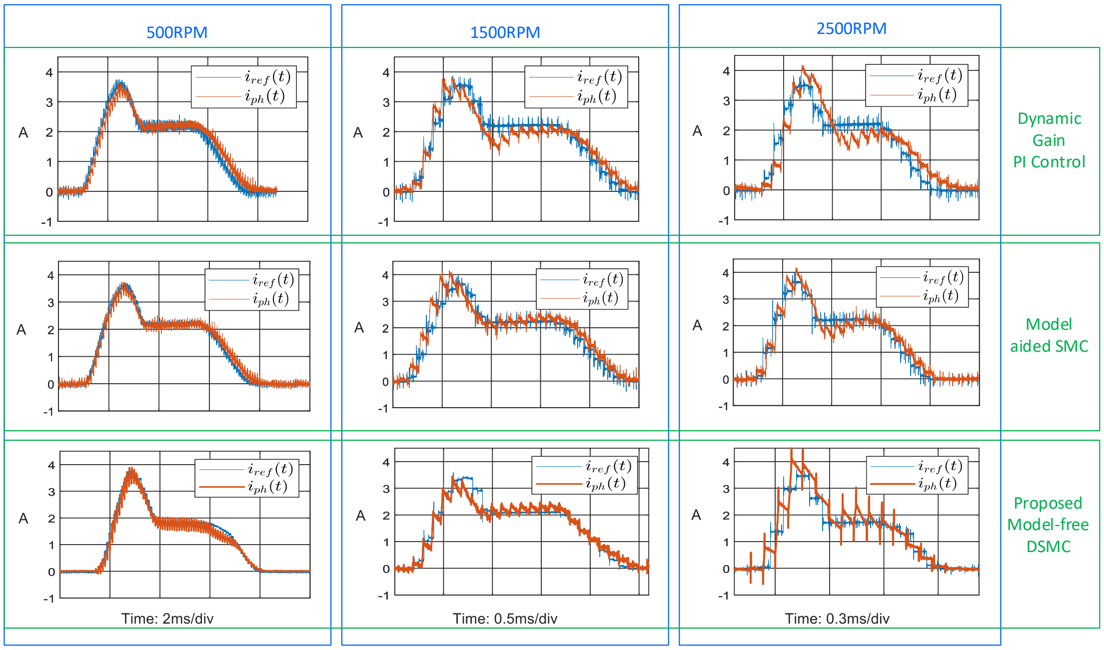

Figure 5.12: Current reference tracking performance of proposed model-free current controller with Dynamic Gain scheduling PI controller and model aided SMC

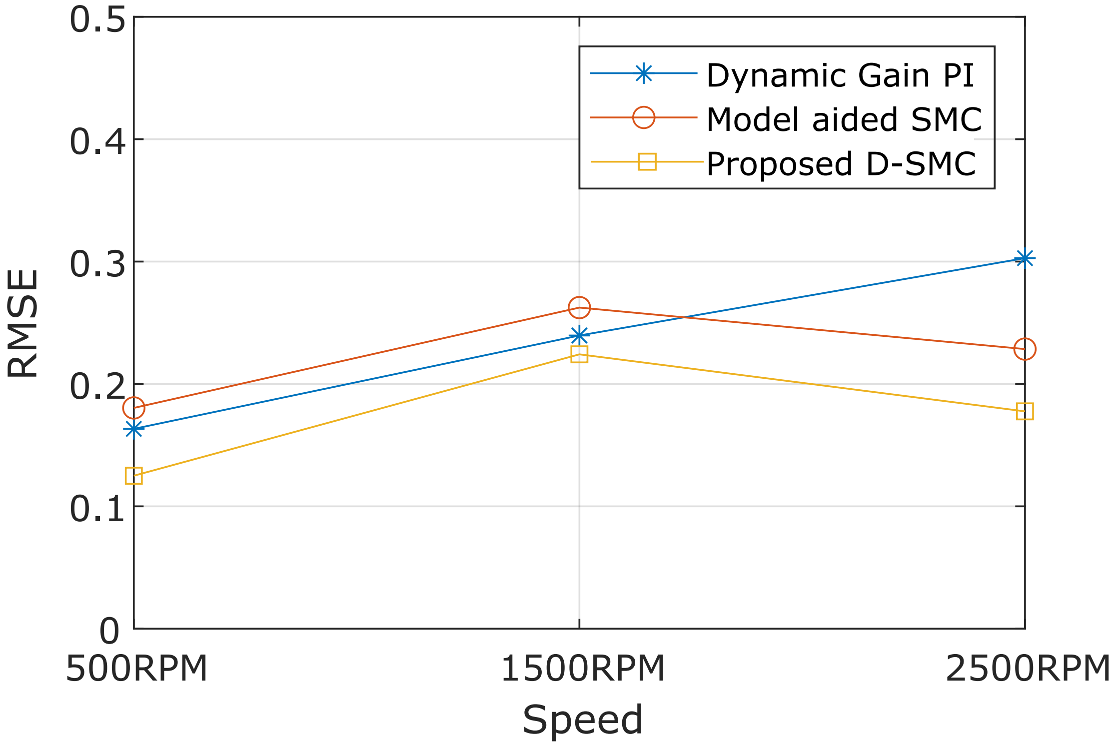

Figure 5.13: RMS current tracking error comparison among dynamic gain scheduling PI, Model aided SMC and proposed D-SMC

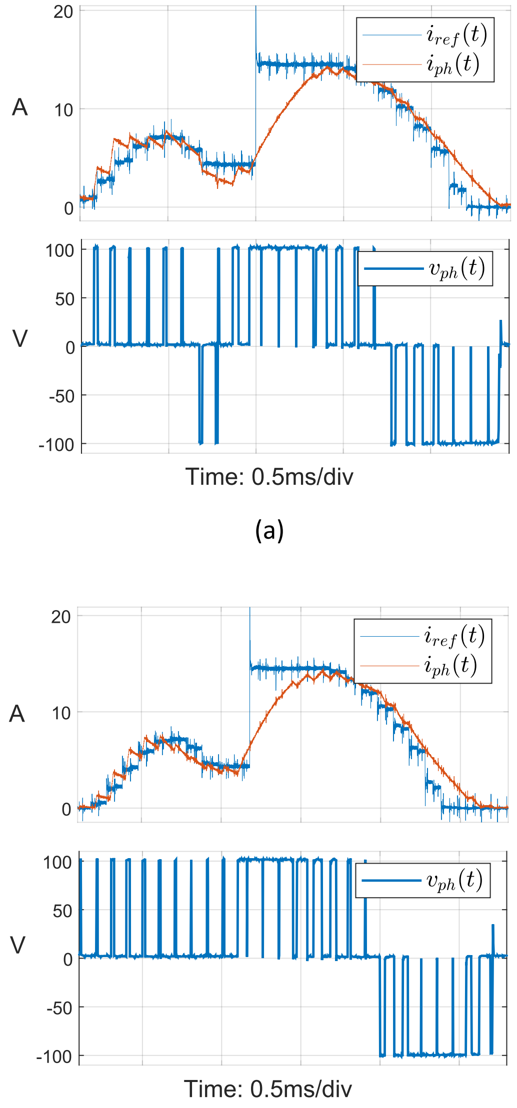

(a)

(b)

Figure 5.14: Current reference tracking performance for step change in reference torque from 0.5Nm to 1.5Nm at 1500RPM (a): model aided SMC, (b): Proposed DSMC

5.7 Summary

This chapter presents realization of a model-free current control of SRM drive. A linearized version of the nonlinear SRM phase current dynamics are obtained in discrete-time domain by treating the non-linear dynamics as an extended state ($\delta_{ph}(k)$). The compensation of $\delta_{ph}(k)$ is performed by using a delayed disturbance approximation. To mitigate the effect of inexact compensation, a compensation control law is proposed via Lyapunov stability analysis.

The simulation and experimental results validate the capability of the proposed controller to maintaining a consistent control performance over a wide conduction period as well as wide speed range amid low signal to noise ratio.

The Current controller presented in this chapter is used to perform the tracking of the references generated through the nonlinear optimization algorithms presented in the next chapters.

Chapter 6

Online Optimization Based Reference Current Identification: Algorithm Development for Torque Ripple, Copper-Loss and Mode-0 Radial Force Minimization

6.1 Introduction

This chapter presents a detailed developmental study of the optimization algorithms for identification of the optimum phase current references to maintain a ripple free torque control while achieving reduced copper loss and/or mode-0 radial forces.

The optimization processes discussed in this chapter are performed online due to their adaptability to dynamic variations in operating conditions and exclusion of cumbersome offline calculations [Valenciagarcia *et al.* (2020)].

The chapter begins with the introduction to the operating conditions for the algorithm and defining the designations for the primary and secondary phases based on the rotor electrical position in Section 6.2. The subsequent sections introduce three approaches utilized to identify the optimum magnitudes of primary and secondary phase current references. Section 6.3 introduces the most basic optimization procedure using 2-dimensional (2-D) gradient-descent algorithm for simultaneous minimization of copper-loss and torque ripple. In the next Section 6.4, a more efficient method is derived by representing the optimization problem introduced in Section 6.3 into a parametric form.

In Section 6.5 the equality constraint is utilized to reduce the 2-D optimization algorithm introduced in Section 6.3 to 1-D. This method commonly known as a projected gradient descent is used to evaluate the variation in the reference phase current profile under different priorities of the secondary objectives, viz. copper loss minimization and mode-0 radial force minimization. Finally, the conclusion derived from this study is presented in Section 6.6.

6.2 Operating Conditions for Online Optimization

One of the distinctive characteristics of an SRM is the dependence of the phase torque on the rotor electrical position. For a digitally controlled SRM drive, the electrical rotor position is obtained at sampling frequency and it is considered constant over the rest of the sampling period. Therefore, following assumption is considered valid throughout this text.

$$\theta_e(t) \approx \theta_e(k) \quad \forall \quad kT_s \leq t \leq (k+1)T_s \tag{6.1}$$

For the 3-Ph SRM drive studied in the thesis, maximum two phases are capable of generating positive torque at any instant. As discussed in Chapter 2, the performance optimization through control is only possible in the overlap region where more than one phases are capable of delivering torque in the desired direction. In the discussion presented ahead, these two phases are referred to as primary and secondary phases. The phase with smaller rotor position exhibits greater misalignment between stator and rotor centre axes and hence consider as an incoming or primary phase. This displacement in the rotor position can be visualized in the form of rotor angle $\theta_e(t)$ shown in Fig.(2.1). A more precise demonstration of the primary and secondary phase assignment process is shown in Fig.(6.1).

In an SRM drive, the required rate of change in the reference torque is usually much smaller compared to the phase current. In the presented study, the change in the reference torque is considered in the form of a 2^{nd} order curve at 250Hz natural frequency. Similar to the rotor position, the magnitude of the reference torque is kept constant over a sampling period whose dynamics are represented through following difference equation.

$$T_{ref}(k) = c_f T_{ref}(k-1) - b_f T_{ref}(k-2) + a_f T_{refss} \tag{6.2}$$

where, $T_{ref}(k)$ represent instantaneous value of the reference torque which is held constant during a sampling period:'k', and T_{refss} is the steady state value of the

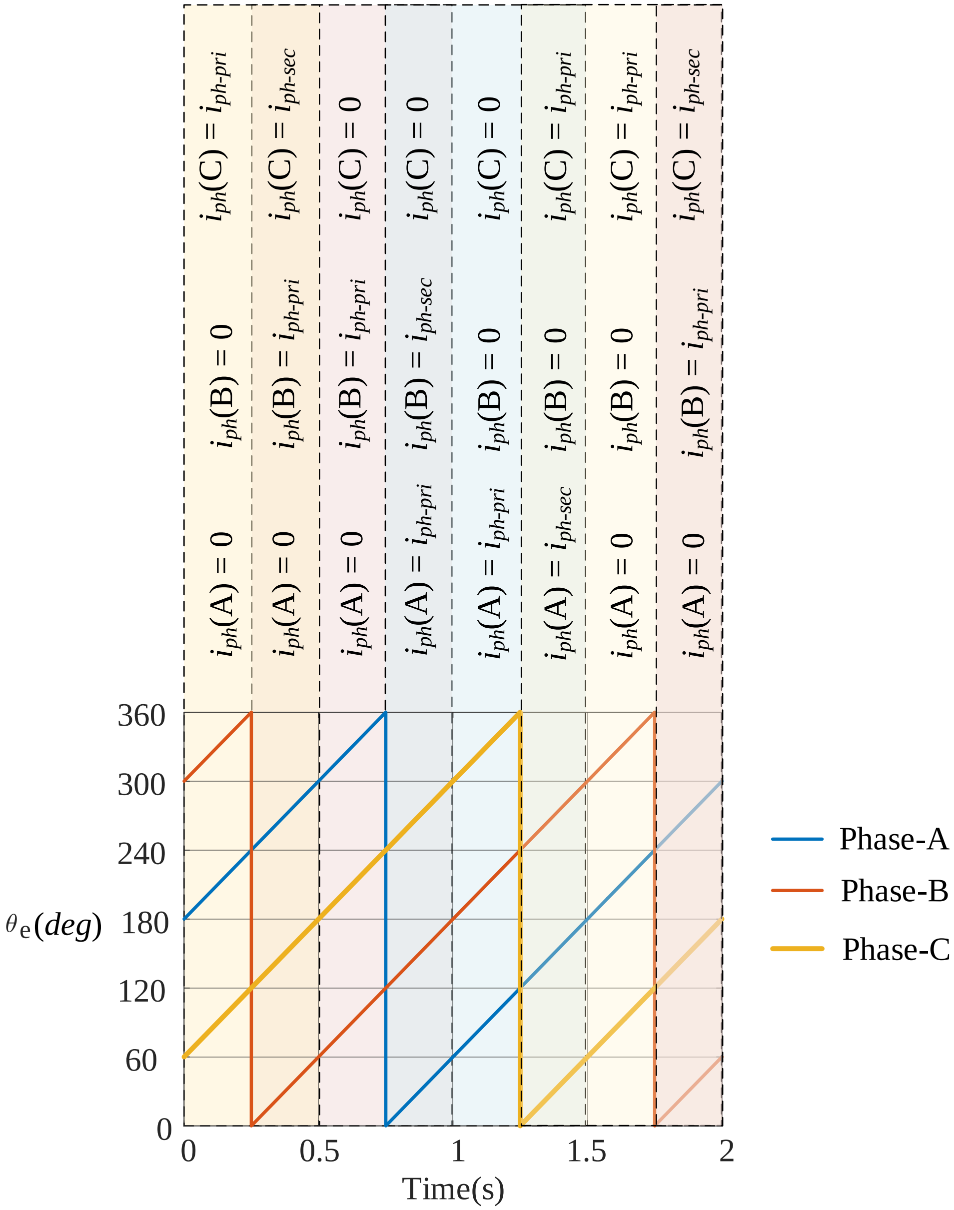

Figure 6.1: Primary and secondary phase assignments

reference torque. The coefficients, a_f, b_f, and c_f are selected to obtain the desired dynamic variation in $T_{ref}(k)$.

Since the reference torque and rotor position change per sampling instant, the identification of the reference currents is performed at each sampling instant and they are kept constant over the rest of the sampling period.

6.3 2-Dimensional Gradient Descent

In a sampling instant: 'k', The torque control problem with copper loss minimization can be represented in the following form.

$$\min_{i_{ph-pri}(k), i_{ph-sec}(k)} \quad i^2_{ph-pri}(k) + i^2_{ph-sec}(k) \tag{6.3a}$$

$$\text{subject to} \quad T_{ref}(k) - T_{ph-pri}(k) - T_{ph-sec}(k) = 0 \tag{6.3b}$$

$$0 \leq i_{ph-pri}(k) \leq i_{max} \tag{6.3c}$$

$$0 \leq i_{ph-sec}(k) \leq i_{max} \tag{6.3d}$$

The above optimization problem aims at minimization of the copper loss via 6.3a. The equality constraint, 6.3b dictates the reduction in the torque ripple. The inequality constraints 6.3c and 6.3d restrict the incoming and outgoing phase currents within admissible range.

The gradient descent method operates on the first derivative of the objective function. Therefore, it is robust to the skewed nature of the non-linear optimization problem. To maintain the constraints in the process of solution identification, the objective function is modified according to the nature of the constraints. These

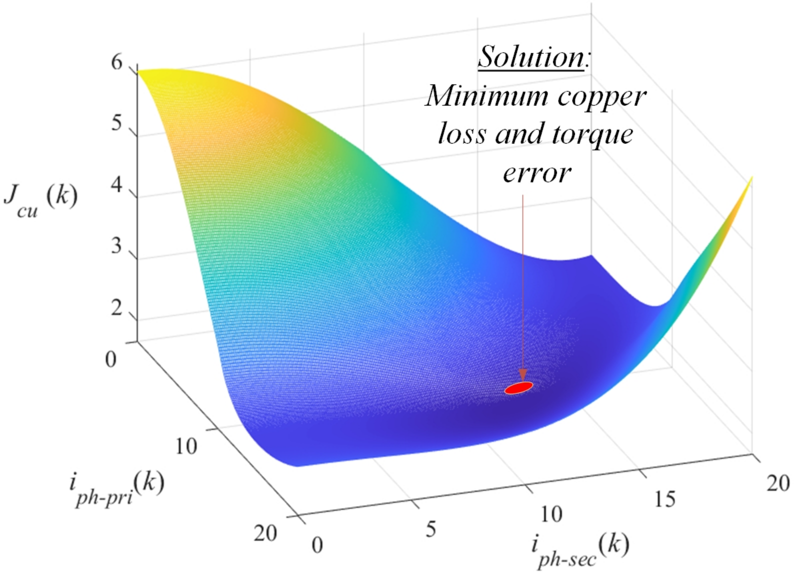

Figure 6.2: Objective function at $\theta_e = 54^0$

modifications influence the gradient of the objective function with respect to $i_{ph-pri}(k)$ and $i_{ph-sec}(k)$ in the close vicinity of these constraints. Thus, restricting also, the solution search space within a feasible range of phase current magnitudes.

The modified objective function is obtained as,

$$\min_{i_{ph-pri}(k), i_{ph-sec}(k)} \quad J_{cu}(k) = i^2_{ph-pri}(k) + i^2_{ph-sec}(k) \tag{6.4a}$$

$$+ W_t \left(T_{ref}(k) - T_{ph-pri}(k) - T_{ph-sec}(k)\right)^2 \tag{6.4b}$$

$$+ \frac{1}{\gamma_{ic}} \left[\left| log(i_{max} - i_{ph-pri}(k)) + log(i_{max} - i_{ph-sec}(k)) \right| \right] \tag{6.4c}$$

The objectives of phase current magnitudes and torque ripple minimization are to some extent, contradictory to each other. Therefore, a weighing factor: W_t is added to achieve a balance between them. The logarithmic barrier functions are added to realize the inequality constraints in the problem. Similar to the equality constraints, they are scaled by a factor γ_{ic} to achieve sufficient influence in relation with the main objective function, and the equality constraint. A graphical representation of the optimization function Eq.(6.4) is shown in Fig.(6.2) for rotor position, $\theta_e = 54^o$. The minimum of the objective function mentioned above undergoes displacement in the 2-D space formed by the optimization variables: $i_{ph-pri}(k), i_{ph-sec}(k)$ for different rotor positions. Fig.(6.3) depicts the displacement of the optimum operating point as a function of primary phase electrical position. The reference torque $(T_{ref}(k))$ considered in this case is 3.5Nm. The displacement in the solution for different magnitude to $T_{ref}(k)$ follows a different trajectory in the 2-D space. However, its nature is consistent with the one shown in Fig.(6.3).

6.3.1 Minimization Principle

The minimization of Eq.(6.4) is achieved by successively adapting $i_{ph-pri}(k)$ and $i_{ph-sec}(k)$ in their negative gradients of $J_{cu}(k)$. Considering negligible mutual coupling in the proposed SRM, these gradients are calculated as following in each iteration step.

$$\frac{\partial J_{cu}(k)|_k}{\partial i_{ph-pri}(k)|_k} = 2i_{ph-pri}(k)|_k + 2W_t \left| \frac{\partial T_{ph-pri}(k)|_k}{\partial i_{ph-pri}(k)|_k} \right| (T_{error}(k)|_k) + \frac{1}{\gamma_{ic}} \left(\frac{1}{i_{max} - i_{ph-pri}(k)|_k} \right) \tag{6.5a}$$

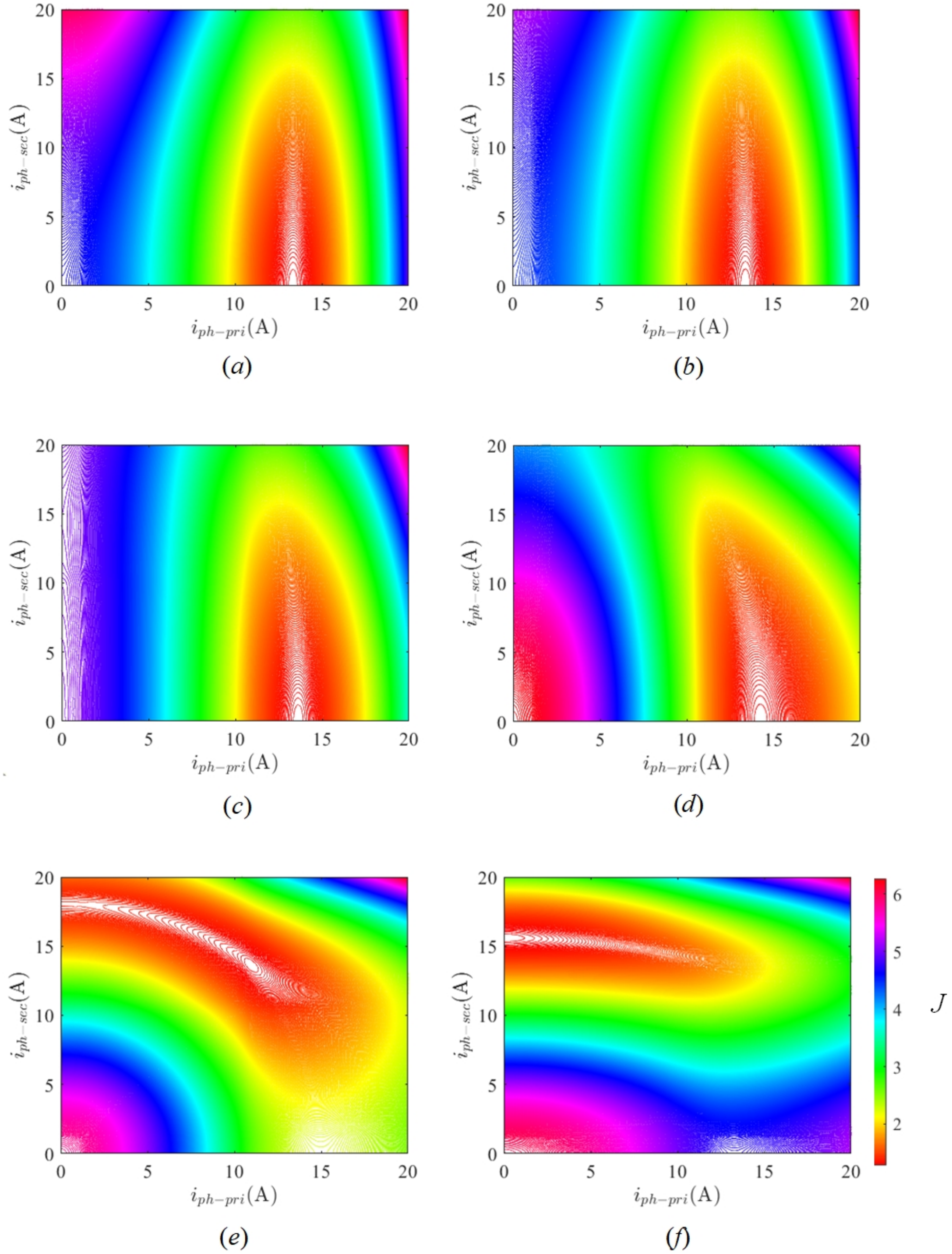

(a) (b) (c) (d) (e) (f)

Figure 6.3: Variation in Objective function for different rotor positionsθ_{e-pri} at 3.5Nm reference torque (a):0^o ; (b): 15^o ; (c): 30^o ; (d): 45^o ; (e): 55^o and (f): 58^o

and

$$\begin{aligned}\frac{\partial J_{cu}(k)|_k}{\partial i_{ph-sec}(k)|_k} = 2i_{ph-sec}(k)|_k + 2W_t\left|\frac{\partial T_{ph-sec}(k)|_k}{\partial i_{ph-sec}(k)|_k}\right|(T_{error}(k)|_k) \\ + \frac{1}{\gamma_{ic}}\left(\frac{1}{i_{max} - i_{ph-sec}(k)|_k}\right)\end{aligned} \tag{6.5b}$$

Where,

$$T_{error}(k)|_k = T_{ref}(k) - T_{ph-pri}(k)|_k - T_{ph-sec}(k)|_k$$

In Eq.(6.5), and the rest of this text, $X(k)|_k$ represents k^{th} iteration at k^{th} sampling instant for a quantity X where, $|_k$ is the iteration index. The cost function gradients presented in Eq.(6.5) require the knowledge of the phase torque and its gradient with respect to the phase current. The torque characteristics with respect to both primary and secondary phase currents are obtained from the static characterization presented in Chapter 2. The torque gradient characteristics with respect to the phase current is obtained by differentiating the torque characteristics with respect to i_{ph}. This characteristics is stored in the form of a lookup table and it calculates the current gradient of the phase torque as,

$$\frac{\partial T_{ph-pri/sec}(k)|_k}{\partial i_{ph-pri/sec}(k)|_k} \approx \left.\frac{\partial T_{ph-pri/sec}(k)}{\partial i_{ph-pri/sec}(k)}\right|_k \tag{6.6}$$

Using the torque gradient information from Eq.(6.6) in Eq.(6.5), the primary and secondary phase currents are updated as,

$$\begin{aligned} i_{ph-pri}(k)|_{k+1} &= i_{ph-pri}(k)|_k - \Lambda \frac{\partial J_{cu}(k)|_k}{\partial i_{ph-pri}(k)|_k} \\ i_{ph-sec}(k)|_{k+1} &= i_{ph-sec}(k)|_k - \Lambda \frac{\partial J_{cu}(k)|_k}{\partial i_{ph-sec}(k)|_k} \end{aligned} \tag{6.7}$$

Where, Λ represents the gradient step size.

The 2-dimensional nature of the gradient descent algorithm does not provide precise control over search direction which is necessary to achieve computational economy. Furthermore, fixed magnitude of the step size is the biggest drawback of gradient descent algorithm. The next section introduced parametric form of the optimization problem: Eq.(6.3). This provision allows 1-D representation of the optimization problem. The next section also introduces the proposed method for online estimation of 2^{nd} gradient of the cost function to achieve faster convergence.

6.4 Gradient Descent in Parametric Form

The most straightforward approach towards reduction in the dimensions of the optimization problem is its transformation into a parametric form. In this approach, the optimization problem in Eq.(6.3) is re-introduced in the following split-form.

$$\begin{aligned} \min_{\|I_{ph}(k)\|} \quad & \|T_{error}(k)\| \\ \text{subject to} \quad & 0 \leq \|I_{ph}(k)\|_\infty \leq i_{max} \end{aligned} \tag{6.8}$$

and

$$\begin{aligned} &\max_{\alpha(k)} \quad \left\| \frac{\partial T_{ph}(k)}{\partial I_{ph}(k)} \right\| \\ &\text{subject to} \quad 0^o \leq \alpha(k) \leq 90^o \end{aligned} \tag{6.9}$$

Where, $\alpha(k)$ is defined as,

$$\alpha(k) = tan^{-1}\left(\frac{i_{ph-pri}(k)}{i_{ph-sec}(k)}\right) \tag{6.10}$$

The 2-norms of phase torque and current vectors defined in chapter 3 are represented as,

$$\|T_{ph}(k)\| = \left\| T_{ph-pri}(k) \quad T_{ph-sec}(k) \right\|^T \tag{6.11a}$$

$$\|I_{ph}(k)\| = \left\| i_{ph-pri}(k) \quad i_{ph-sec}(k) \right\|^T \tag{6.11b}$$

For a fixed value of $\|I_{ph}(k)\|$, the relation between primary and secondary currents is obtained as,

$$i_{ph-pri}(k) = \|I_{ph}(k)\| sin(\alpha(k)) \tag{6.12a}$$

$$i_{ph-sec}(k) = \|I_{ph}(k)\| cos(\alpha(k)) \tag{6.12b}$$

Whereas, the torque gradient matrix is obtained as,

$$\frac{\partial T_{ph}(k)}{\partial I_{ph}(k)} = \begin{bmatrix} \frac{\partial T_{ph-pri}(k)}{\partial i_{ph-pri}(k)} & 0 \\ 0 & \frac{\partial T_{ph-sec}(k)}{\partial i_{ph-sec}(k)} \end{bmatrix} \tag{6.13}$$

The relation between $\alpha(k)$ and $\frac{\partial T_{ph-pri}(k)}{\partial i_{ph-pri}(k)}$ is defined through Eq.(6.12) and Eq.(6.13) and will be used ahead for identification of optimum search direction ($\alpha(k)$).

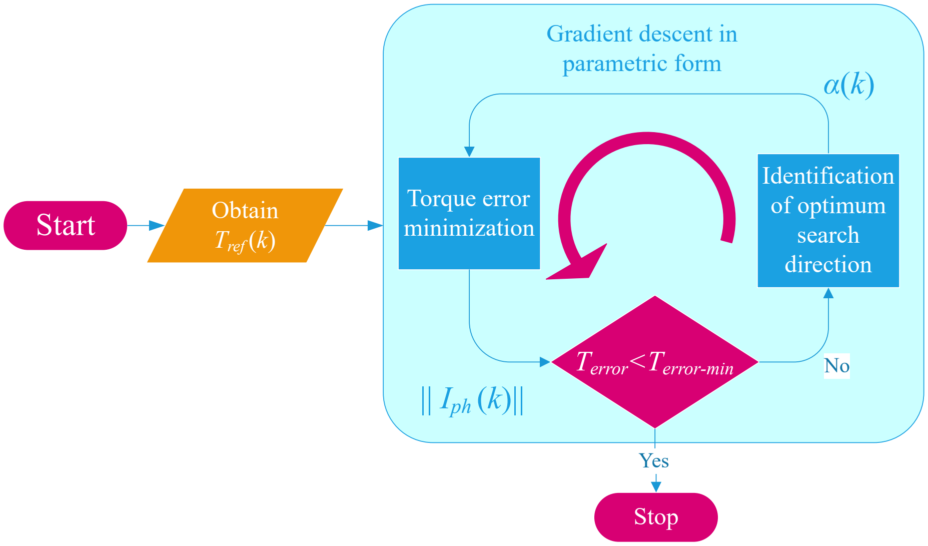

Figure 6.4: Flowchart of solution method using gradient descent in parametric form

The first optimization problem: Eq.(6.8) called 'torque error minimization' is aimed at achieving the desired torque reference while Eq.(6.9) called 'gradient maximization' focuses on identification of the steepest direction of the current gradient of the torque characteristics. Maintaining adaptation in $\|I_{ph}(k)\|$ along steepest direction of the current gradient ensures that the reference torque is achieved with minimum magnitude of $I_{ph}(k)$.

As, shown in Eq.(6.8), the torque error minimization is a 1-D problem in $\|I_{ph}(k)\|$. Due to its coupling with the torque gradient maximization problem (Eq.(6.9)), each iteration of torque error minimization is preceded by fully solving torque gradient maximization problem for the current value of $\|I_{ph}(k)\||_k$. This ensures that each step change in $\|I_{ph}(k)\|$ is performed in an optimum direction. The optimization process using gradient descent method in parametric form is shown in Fig.(6.4).

6.4.1 Torque Error Minimization

The solution of the torque error minimization is identified by finding iterative solution to the following value function.

$$\mathscr{V}_t(k)|_k = \frac{1}{2}(T_{error}(k)|_k)^2 \tag{6.14}$$

As the reference torque is constant for a sampling instant, the phase current gradient of the value function is obtained as,

$$\left.\frac{\partial \mathscr{V}_t(k)}{\partial I_{ph}(k)}\right|_k = -\left.\frac{\partial T_{ph}(k)}{\partial I_{ph}(k)}\right|_k T_{error}(k) \tag{6.15}$$

Using Eq.(6.15), the first few iterations are updated as,

$$\|I_{ph}(k)\||_{k+1} = \|I_{ph}(k)\||_k - \Lambda \left.\left\|\frac{\partial \mathscr{V}_t(k)}{\partial I_{ph}(k)}\right\|\right|_k \tag{6.16}$$

6.4.2 Identification of Optimum Search Direction

During the torque error minimization, the updated value of the phase current magnitude $\|I_{ph}(k)\||_{k+1}$ is used to identify the new phase current vector: $I_{ph}(k)|_{k+1|\alpha(k)|_{k+1}}$. From $I_{ph}(k)|_{k+1|\alpha(k)|_k}$, the new search direction: $\alpha(k)|_{k+1}$ is identified by solving the maximization problem in Eq.(6.9).

The rest of this section employs following notations for sampling instant, and iteration indices for torque error minimization and optimum search direction identification loops.

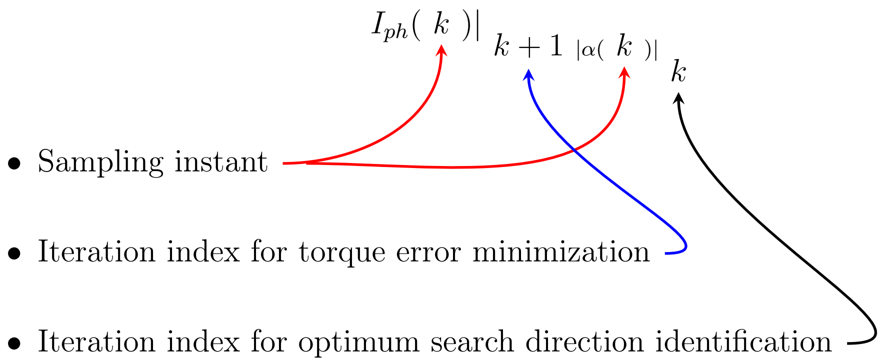

$$I_{ph}(\ k\ )|_{\ k+1\ |\alpha(\ k\ )|\ k}$$

- Sampling instant
- Iteration index for torque error minimization
- Iteration index for optimum search direction identification

First, $I_{ph}(k)|_{k+1|\alpha(k)|_k}$ is resolved into primary and secondary currents using $\alpha(k)|_k$.

$$i_{ph-pri}(k)|_{k+1|k} = \|I_{ph}\||_{k+1} sin(\alpha(k)|_k) \tag{6.17a}$$

and

$$i_{ph-sec}(k)|_{k+1|k} = \|I_{ph}\||_{k+1} cos(\alpha(k)|_k) \tag{6.17b}$$

The value function for the optimization problem, Eq.(6.9) is defined as,

$$\mathcal{V}_{\alpha}(k)|_k = \left\| \frac{\partial \mathscr{V}_t(k)}{\partial I_{ph}(k)} \right\| \Bigg|_k \tag{6.18}$$

Fig.(6.5) shows the variation in value function, $\mathcal{V}_{\alpha}(k)|_k$ as a function of $\|I_{ph}(k)\|$ and $\alpha(k)$ at $\theta_{pri} = 55^o$ ($\theta_{sec} = 175^o$). Large magnitude of $\|I_{ph}(k)\|$ signifies large net torque contribution from the motor. Therefore, $\alpha(k)$ tends to remain close to 45^o. The solution for the maximization problem is identified for a single value of $\|I_{ph}(k)\|$. The nature of the optimization procedure can be visualized through Fig.(6.6) for successive iteration of $\|I_{ph}(k)\|$. The figure depicts the evolution in the 1-D solution space of Eq.(6.9) for a particular case where the torque ripple minimization process yields the

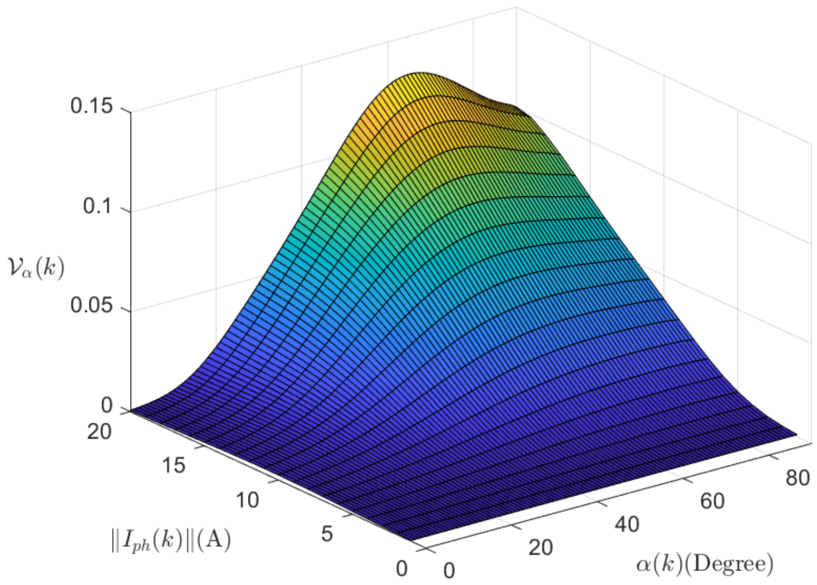

Figure 6.5: Variation in $\mathcal{V}_\alpha$ as a function of $\|I_{ph}\|$ and α at $\theta_{pri} = 55^o$

phase current vector magnitude: 2A, 7A, 14A and 21A in 4 consecutive iterations. It is important to note here that the optimum search direction identification is performed after each iteration of Eq.(6.8) and the new value of $\|I_{ph}(k)\|$ is influenced by the solution of Eq.(6.9). The particular case shown in Fig.(6.6) in presented only for the demonstration of solution identification process. The 1-D solution space for Eq.(6.9) is not exactly convex as shown in Fig.(6.6). Therefore, it is not advisable to use 2^{nd} derivative information of $\mathcal{V}_\alpha(k)$ without getting sufficiently closer to the solution. Moreover, since it is embedded in the torque error reduction problem, it is desirable to have an efficient non-iterative algorithm which can guarantee the solution within a fixed number of computations.

Considering the above requirements, a tree search algorithm is introduced. In the presented process, the gradient of $\mathcal{V}_\alpha(k)$ at a specific $\alpha(k)$ is approximately calculated

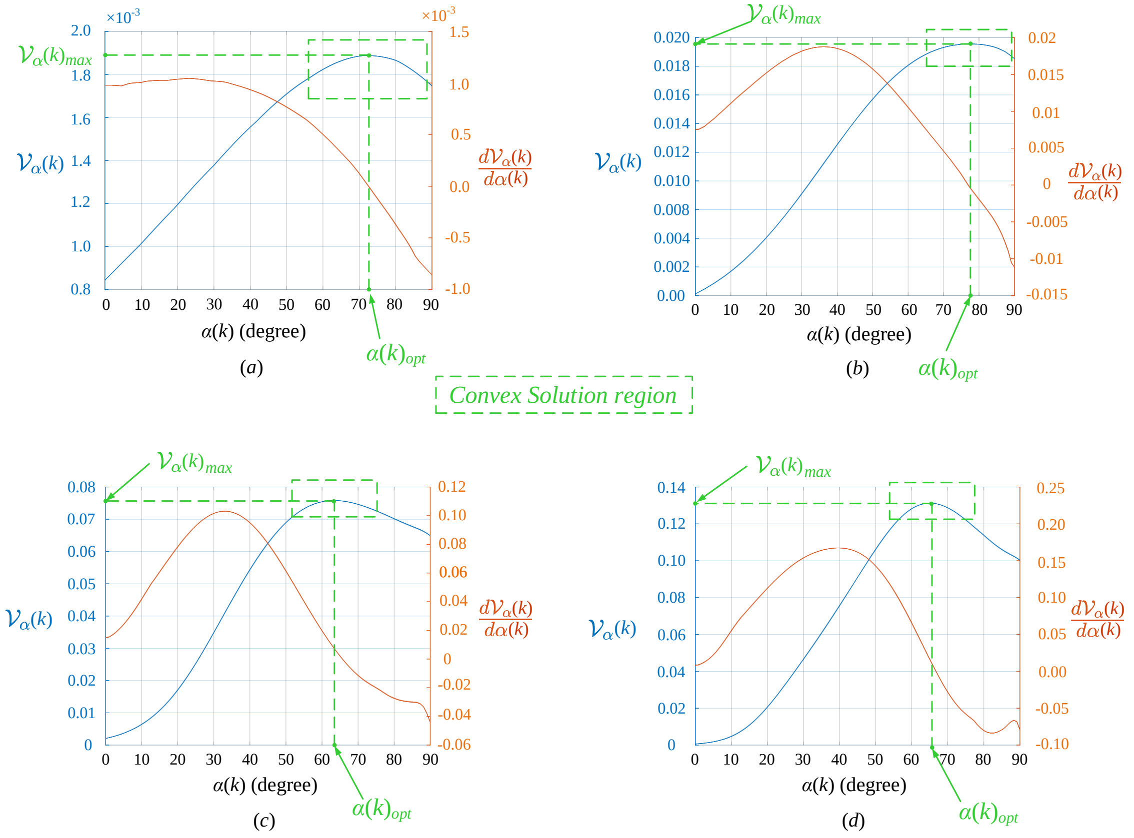

Figure 6.6: 1-D solution space in optimum search direction identification problem for increasing $\|I_{ph}\|$: (a)=2A, (b)=7A, (c)=14A, (d)=21A at $\theta_{pri}(k) = 55^o(\theta_{sec}(k) = 175^o)$

using mean value theorem as following [Besenyei (2012)].

$$\nabla \mathcal{V}_{\alpha}(k)\big|_{\alpha'(k)} = \left.\frac{\partial \mathcal{V}_{\alpha}(k)}{\partial \alpha(k)}\right|_{\alpha'(k)} \approx \frac{\mathcal{V}_{\alpha}(k)\big|_{\alpha'(k)+\bar{\alpha}} - \mathcal{V}_{\alpha}(k)\big|_{\alpha'(k)-\bar{\alpha}}}{2\bar{\alpha}} \tag{6.19}$$

In the proposed scheme, the gradient information:$\nabla \mathcal{V}_{\alpha}(k)$ is used to identify the convex region where the solution exists and only then the second derivative $\nabla^2 \mathcal{V}_{\alpha}(k)$ is used to find the exact solution. Similar to Eq.(6.19), $\nabla^2 \mathcal{V}_{\alpha}(k)$ is calculated as,

$$\nabla^2 \mathcal{V}_{\alpha}(k)\big|_{\alpha'(k)} = \left.\frac{\partial^2 \mathcal{V}_{\alpha}(k)}{\partial \alpha^2(k)}\right|_{\alpha'(k)} \approx \frac{\nabla \mathcal{V}_{\alpha}(k)\big|_{\alpha'(k)+\bar{\alpha}} - \nabla \mathcal{V}_{\alpha}(k)\big|_{\alpha'(k)-\bar{\alpha}}}{2\bar{\alpha}} \tag{6.20}$$

Finally, the optimum search direction is identified as,

$$\alpha(k)\big|_{k+1} = \alpha(k)_{opt} = \alpha'(k) - \frac{\nabla \mathcal{V}_{\alpha}(k)\big|_{\alpha'(k)}}{\nabla^2 \mathcal{V}_{\alpha}(k)\big|_{\alpha'(k)}} \tag{6.21}$$

The complete solution method for maximization problem:Eq.(6.9) using proposed tree search algorithm is presented in Fig.(6.7).

6.4.3 Faster Torque Error Minimization

As discussed earlier, due to the quasi-convex solution space in the minimization problem Eq.(6.8), first few iterations are performed with a fixed step gradient descent. From the second step, the successive values of $\dfrac{\partial \mathscr{V}_t(k)}{\partial \|I_{ph}(k)\|}$ are used to calculate the approximate second derivative as,

$$\left.\frac{\partial^2 \mathscr{V}_t(k)}{\partial \|I_{ph}(k)\|^2}\right|_{k+1|k+2} \approx \frac{\frac{\partial \mathscr{V}_t(k)}{\partial \|I_{ph}(k)\|}\Big|_{k+2} - \frac{\partial \mathscr{V}_t(k)}{\partial \|I_{ph}(k)\|}\Big|_{k+1}}{\|I_{ph}(k)\|\big|_{k+2} - \|I_{ph}(k)\|\big|_{k+1}} \tag{6.22}$$

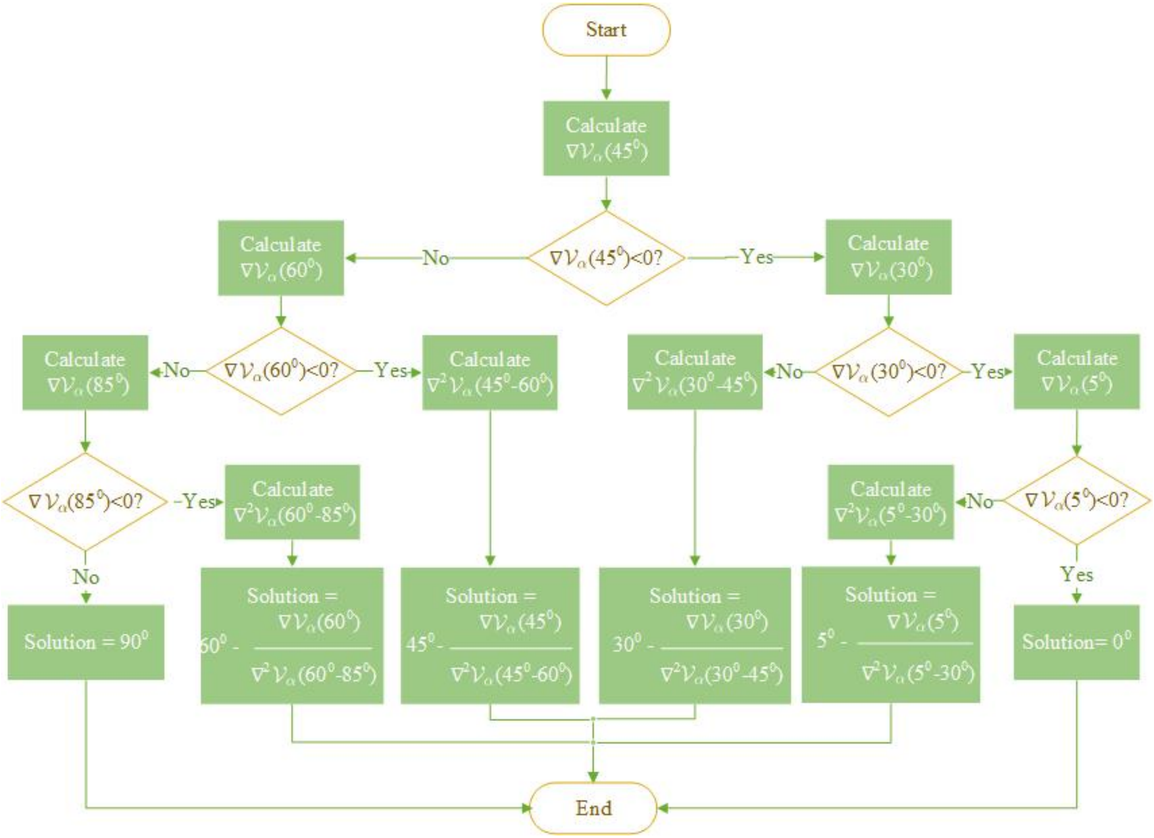

Figure 6.7: Tree search algorithm for identification of optimum search direction: α_{opt}

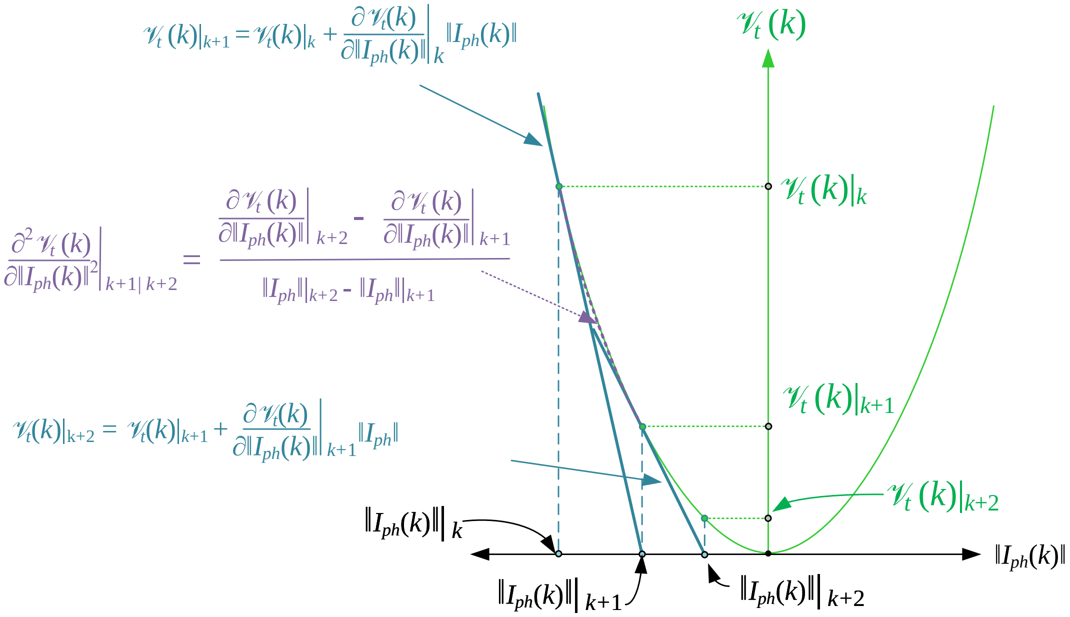

Figure 6.8: Identification of $\dfrac{\partial^2 \mathscr{V}_t(k)}{\partial\|I_{ph}(k)\|}$ in successive iterations

This process is depicted in Fig.(6.8). Using Eq.(6.22), the final adaptations in $\|I_{ph}(k)\|$ are performed as,

$$\|I_{ph}(k)\|_{k+3} = \|I_{ph}(k)\|_{k+2} - \frac{\frac{\partial \mathscr{V}_t(k)}{\partial\|I_{ph}(k)\|}\Big|_{k+2}}{\frac{\partial^2 \mathscr{V}_t(k)}{\partial\|I_{ph}(k)\|^2}\Big|_{k+1|k+2}} \tag{6.23}$$

Due to approximate nature of $\dfrac{\partial^2 \mathscr{V}_t(k)}{\partial\|I_{ph}(k)\|^2}$, Eq.(6.23) may not yield accurate solution at every instant. Therefore, several iterations are required to achieve a sufficient accuracy.

6.5 Projected Gradient Descent

In the previous two methods, the phase currents are used as optimization variables. This provides ease in handling the inequality constraints on phase current magnitude. However, the equality constraint is difficult to manage and it can only be satisfied through and iterative evaluation as performed in the previously discussed methods. In this section, the phase torque is considered as optimization variable. The reduction of the solution process dimensions from 2 to 1 is achieved by represented the secondary phase torque as a function of the primary phase torque using the equality constraint. The restrictions on phase current magnitude are handled more pragmatically using simple saturation functions.

The representation of the optimization problem using torque as optimization variable is obtained as,

$$\begin{aligned} \min_{T_{ph}(k)} \quad & \|I_{ph}(k)\| \\ \text{subject to} \quad & |T_{ph}(k)| - T_e = 0 \\ & 0 \leq \|T_{ph}(k)\|_\infty \leq T_{ph}(i_{max}, \theta_e(k)) \end{aligned} \tag{6.24}$$

Similar to the optimization processes presented in the previous section, the problem presented in Eq.(6.24) varies as a function of rotor position. The limit on the phase current magnitude however, is relatively difficult to handle. Since phase torque is also a function of rotor position, the inequality constraint is defined through a torque function varying as a function of the sampled rotor position.

6.5.1 Reduction to 1-D Problem Through Projection

The equality constraint on the phase torque is used to represent the secondary phase torque as a function of the primary phase torque as,

$$T_{sec}(k)|_k = T_{ref}(k) - T_{pri}(k)|_k \tag{6.25}$$

To simplify the representation of the solution process, the phase currents are represented as functions of torque as,

$$i_{ph-pri}(k)|_k = \mathcal{F}_{ph}(T_{ph-pri}(k)|_k, \theta_{e-pri}(k)) \tag{6.26a}$$

$$\begin{aligned} i_{ph-sec}(k)|_k &= \mathcal{F}_{ph}(T_{ph-sec}(k)|_k, \theta_{e-sec}(k)) \\ &= \mathcal{F}_{ph}(T_{ref}(k) - T_{ph-pri}(k)|_k, \theta_{e-sec}(k)) \end{aligned} \tag{6.26b}$$

The functions, $\mathcal{F}_{ph}(T_{pri}(k), \theta_{e-pri}(k))$ and $\mathcal{F}_{ph}(T_{ph-sec}(k), \theta_{e-sec}(k))$ are derived from the 'Torque-Current' characteristics shown in Fig.(6.9). This characteristics is derived by inverting the 'Current-Torque' characteristics generated via FEA analysis. Similar to the processes introduced previously in this chapter, the objective of copper loss minimization is represented as,

$$\mathcal{V}_{cu}(k)|_k = \frac{1}{2} I_{ph}(k)|_k^T I_{ph}(k)|_k \tag{6.27}$$

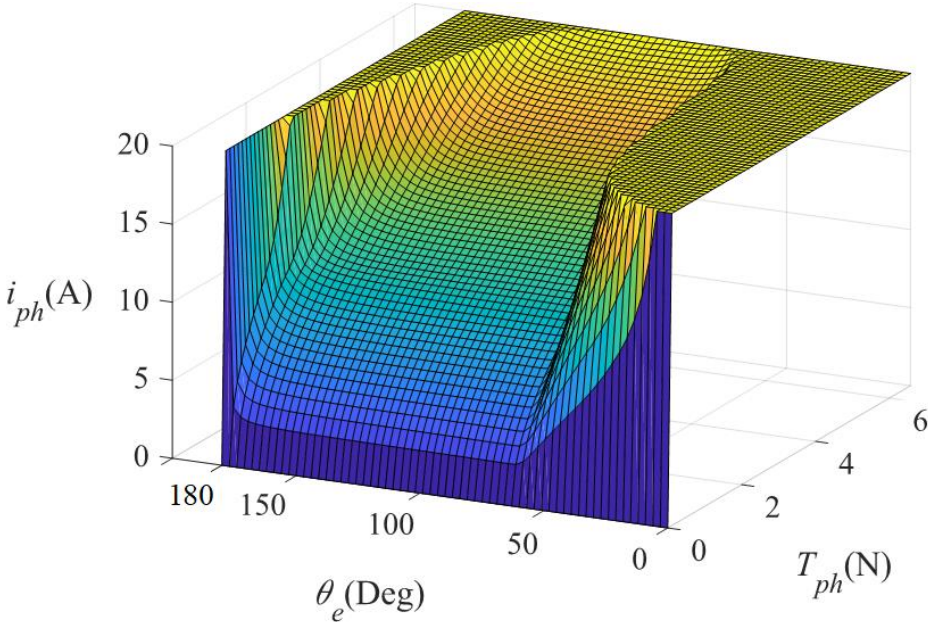

Figure 6.9: Torque to current characteristics

Using the substitution from Eq.(6.26a) and Eq.(6.26b), the gradient of $\mathcal{V}_{cu}(k)$ with respect to $T_{ph-pri}(k)$ is calculated as,

$$\begin{aligned}\nabla\mathcal{V}_{cu}(k)|_k &= \frac{\partial\mathcal{V}_{cu}(k)|_k}{\partial T_{ph-pri}(k)|_k}\\ &= \mathcal{F}_{ph}(T_{ph-pri}(k)|_k, \theta_{e-pri}(k))\frac{\partial\mathcal{F}_{ph}(T_{ph-pri}(k)|_k, \theta_{e-pri}(k))}{\partial T_{ph-pri}(k)|_k}\\ &- \mathcal{F}_{ph}(T_{ref}(k) - T_{ph-pri}(k)|_k, \theta_{e-sec}(k))\frac{\partial\mathcal{F}_{ph}(T_{ref}(k) - T_{ph-pri}(k)|_k, \theta_{e-sec}(k))}{\partial T_{ph-pri}(k)|_k}\end{aligned} \tag{6.28}$$

Using Eq(6.28), the adaptation in the primary torque reference is performed as following.

$$T_{ph-pri}(k)|_{k+1} = T_{ph-pri}(k)|_k - \lambda\nabla\mathcal{V}_{cu}(k)|_k \tag{6.29}$$

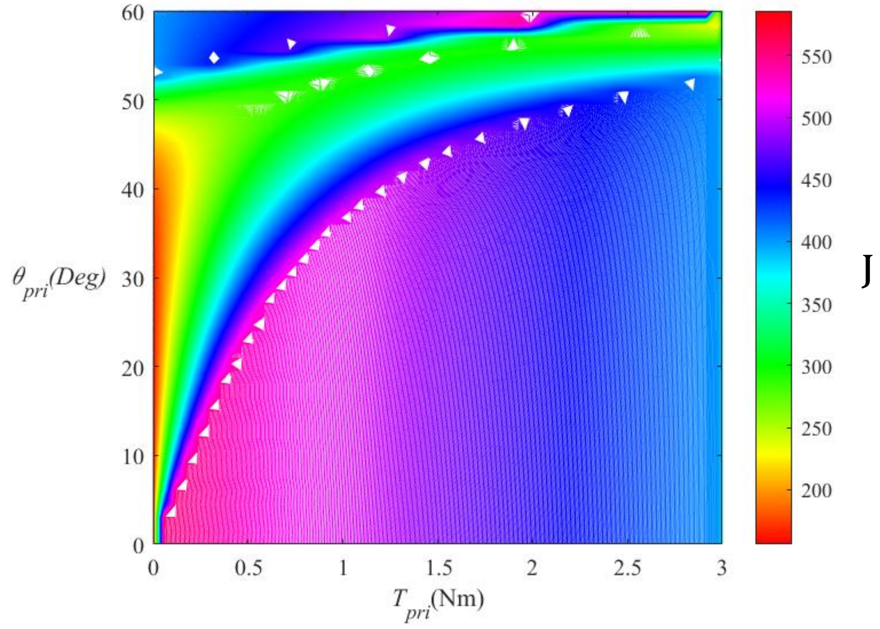

Figure 6.10: Variation in the optimum solution as a function of rotor position and T_{ph}

The nature of the solution space with projected gradient descent algorithm can be visualized as a function of $\theta_{e-pri}(k)$ and $T_{ph-pri}(k)$ through Fig.(6.10). At $\theta_{e-pri}(k) = 0$, the desired torque contribution from primary phase is zero as expected and it grows upto $T_{ref}(k)$ as $\theta_{e-pri}(k)$ approaches 60^o. The minimization in the copper loss is achieved by maintaining the contribution of the primary phase torque along the minimum $\mathcal{V}_{cu}$ throughout the displacement in θ_{e-pri}.

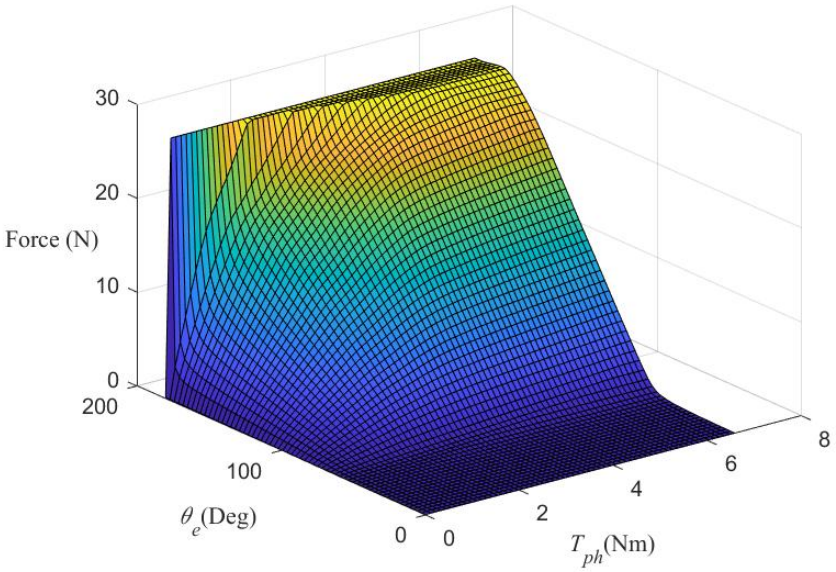

Figure 6.11: Torque to force characteristics

6.5.2 Mode-0 Radial Force Minimization

The objective of Mode-0 radial force minimization is represented in similar form as the copper loss minimization as,

$$\mathcal{V}_{rf}(k)|_k = \frac{1}{2}(F_{ph}(T_{ph-pri}(k)|_k, \theta_{e-pri}(k)))^2 + \frac{1}{2}(F_{ph}(T_{ph-sec}(k)|_k, \theta_{e-sec}(k)))^2 \quad (6.30)$$

In Eq.(6.30), The mode-0 radial force characteristics: $F_{ph}(T_{ph-pri}(k)|_k, \theta_{e-pri}(k))$ and $F_{ph}(T_{ph-sec}(k)|_k, \theta_{e-sec}(k))$ are represented as a function of rotor position and radial force. These characteristics shown in Fig.(6.11) are obtained by combining the 'Torque-to-Current' characteristics with 'Current-to-Force' characteristics.

Intuitively, using the equality constraint to reduce dimension, the transformed

Eq.(6.30) and its gradient are obtained as,

$$\begin{aligned}\mathcal{V}_{rf}(k)|_k = {} & \frac{1}{2}(F_{ph}(T_{ph-pri}(k)|_k, \theta_{e-pri}(k)))^2 \\ & + \frac{1}{2}(F_{ph}(T_{ref}(k) - T_{ph-pri}(k)|_k, \theta_{e-sec}(k)))^2 \end{aligned} \tag{6.31a}$$

$$\begin{aligned}\nabla\mathcal{V}_{rf}(k)|_k &= \frac{\partial\mathcal{V}_{rf}(T_{ph-pri}(k)|_k, \theta_{e-pri}(k))}{\partial T_{ph-pri}(k)|_k} \\ &= F_{ph}(T_{ph-pri}(k)|_k, \theta_{e-pri}(k))\frac{\partial F_{ph}(T_{ph-pri}(k)|_k, \theta_{e-pri}(k))}{\partial T_{ph-pri}(k)|_k} \\ & - F_{ph}(T_{ref}(k) - T_{ph-pri}(k)|_k, \theta_{e-sec}(k))\frac{\partial F_{ph}(T_{ref}(k) - T_{ph-pri}(k)|_k, \theta_{e-sec}(k))}{\partial T_{ph-pri}(k)|_k}\end{aligned} \tag{6.31b}$$

6.5.3 Combined Minimization Copper Loss and Mode-0 Radial Force

Adding the objectives of radial force and copper loss minimization, the combined cost function is represented as,

$$\begin{aligned}\mathcal{V}_{cu-rf}(k)|_k = {} & \frac{1}{2}(\mathcal{F}_{ph}(T_{ph-pri}(k))|_k, \theta_{e-pri}(k))^2 + \frac{1}{2}(\mathcal{F}_{ph}(T_e(k) - T_{pri}(k), \theta_{e-sec}(k)))^2 \\ & + \frac{W_w}{2}\big((F_{ph}(T_{ph-pri}(k)|_k, \theta_{e-pri}(k)))^2 + (F_{ph}(T_{ref} - T_{ph-pri}, \theta_{e-sec}(k)))^2\big)\end{aligned} \tag{6.32}$$

The phase torque gradient of $\mathcal{V}_{cu-rf}(k)|_k$ is obtained as described in Eq.(6.28) and Eq.(6.31). The two extreme cases for the solution trajectories correspond exclusively to the objectives of copper loss minimization alone and mode-0 radial force minimization alone as shown in Fig.(6.12). The choice of W_w allows to shift the solution trajectory between the two depicted in Fig(6.12).

6.6 Summary

The 2-D gradient descent algorithm provides a simplest and very robust process for minimization of the quazi-convex optimization problems introduced in the beginning of this chapter. However, for online implementation, the computational efficiency is extremely essential and it can not be guaranteed in every operating condition due to its fixed step nature. The changing nature of the optimization problem as a function of operating conditions can potentially results into inconsistent performance of the algorithm mainly during the phase overlap region due to 2 dimensional nature of the problem.

In the subsequent development, the challenges mentioned above are tackled by splitting the optimization problem into two 1-dimensional problems in the parametric form. Moreover, a faster solution method is introduced to take full advantage of the convexity of the sub-level set surrounding the solution. These modifications are performed in anticipation of the improvement in accuracy and efficiency of the solution method. Due to greater displacement in the solution per sampling period at higher speed, the accuracy of the algorithm is likely to reduce. Although each iteration in parametric form gradient descent algorithm is more computationally expensive as compared to conventional 2D gradient descent algorithm, the superiority of the former can be justified in terms of its ability to achieve solution in wider operating range.

The final method: projected gradient descent attempts to achieve reduction from 2 to 1D by defining the secondary phase quantities through equality constraint. This provision also ensures that the objective of torque ripple reduction remains satisfied

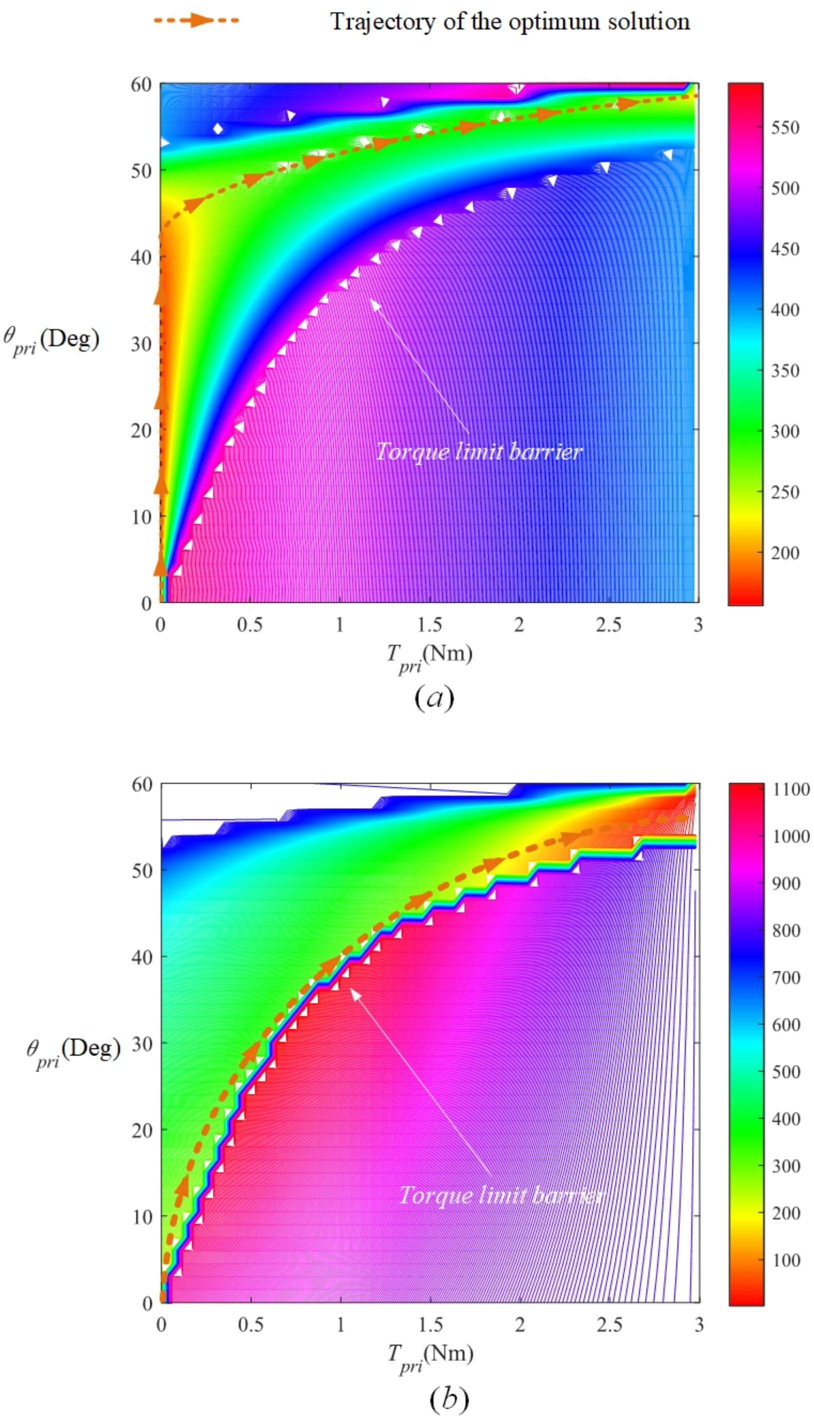

Figure 6.12: Optimum solution trajectories for (a) Copper loss minimization alone, (b) mode-0 radial force minimization alone

while the secondary objectives are being addressed through minimization.

Chapter 7

Online Optimization Based Reference Current Identification: Performance Evaluation

7.1 Introduction

In this chapter, the performance of non-linear minimization algorithms developed in the previous chapter is evaluated for different operating conditions. The chapter presents the implementation framework for each algorithm followed by the simulation study in MATLAB/Simulink® environment.

The subsequent sections, 7.2, 7.3, and 7.4 provide the implementation procedure followed by simulation results for 2-D gradient descent, parametric form gradient descent and projected gradient descent algorithms respectively. These sections, in sequence provide a developmental process for realization of the final projected gradient based algorithm. The 2-D gradient descent and parametric form gradient descent algorithms are evaluated for copper-loss minimization alone while simultaneous minimization of the mode-0 radial force and copper-loss is evaluated for projected gradient descent algorithm. The operation of this algorithm is also demonstrated in real-time over a TI-DSP F28377D micro-controller.

7.2 2-D Gradient Descent

The 2-D gradient descent algorithm requires the knowledge of torque and current gradient of torque (referred to as torque gradient for brevity) to identify the instantaneous magnitude of the objective function and its current gradients. For computational efficiency, these characteristics are stored in the form of 2-D LUTs. The complete implementation framework for 2-D gradient descent algorithm is shown in Fig.(7.1). At a sampling instant k, the sampled position signal is resolved into primary and secondary phases as detailed in Chapter 6. These signals are used to distinguish primary and secondary torque and torque gradient characteristics from the LUTs. These characteristics are employed in an iterative process to identify optimum values of $i_{ph-pri}(k)$ and $i_{ph-sec}(k)$. It should be noted that the unit delay function:z^{-1} in Fig.(7.1) corresponds to the iterations in the optimization process alone.

Fig.(7.2) shows the simulation result for reference torque tracking performance for $T_{ref-ss} = 2Nm$ at 100RPM. The worst case torque ripple appears during the phase commutation region defined by non-zero values of phase currents as shown in Fig.(6.1). The performance limitation of this algorithm during the phase commutation period becomes increasingly significant as the operating speed increases. As shown in Fig.(7.3), the torque ripple is very large at 500RPM. In the current implementation process, solution achieved at previous sampling instant is used as initial condition

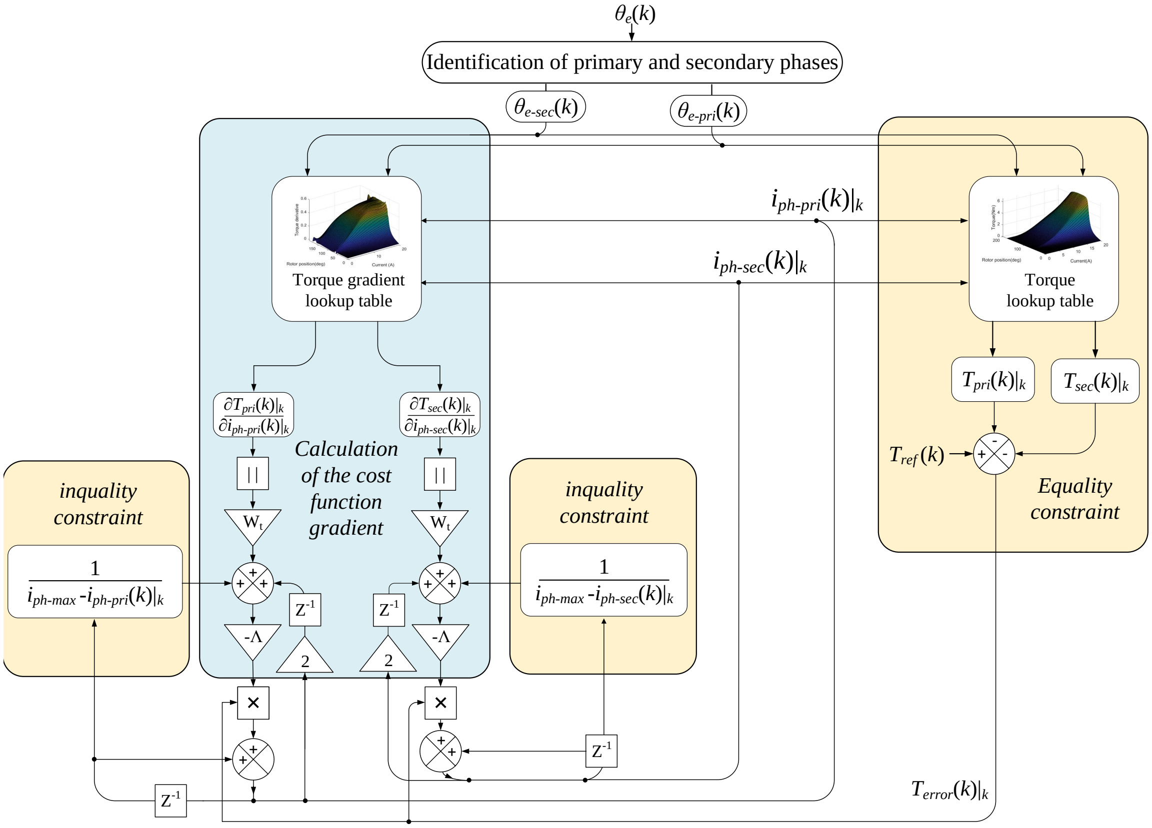

Figure 7.1: Implementation framework for 2D gradient descent algorithm

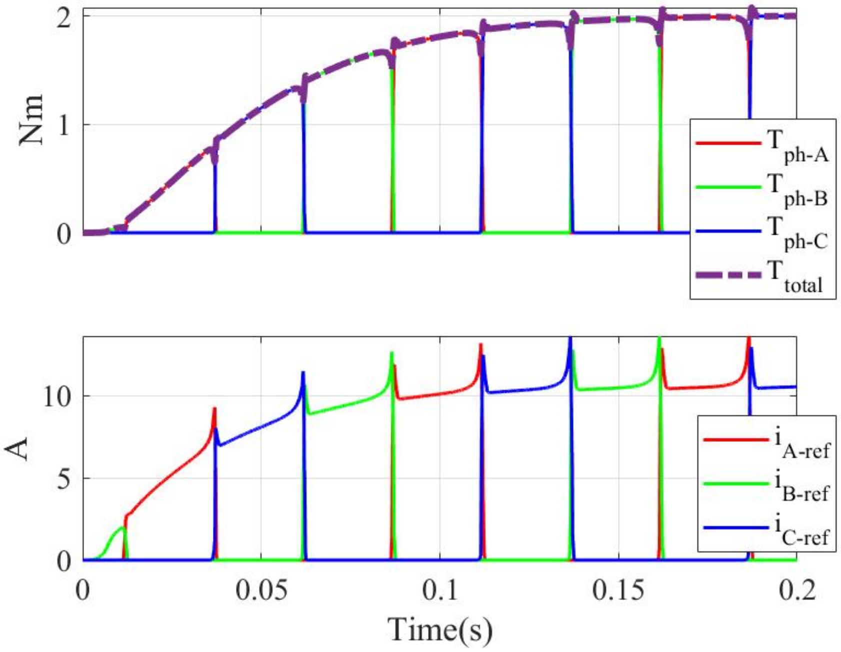

Figure 7.2: Phase current reference identification via gradient descent algorithm for $T_{ref} = 2Nm$ and speed = 100RPM

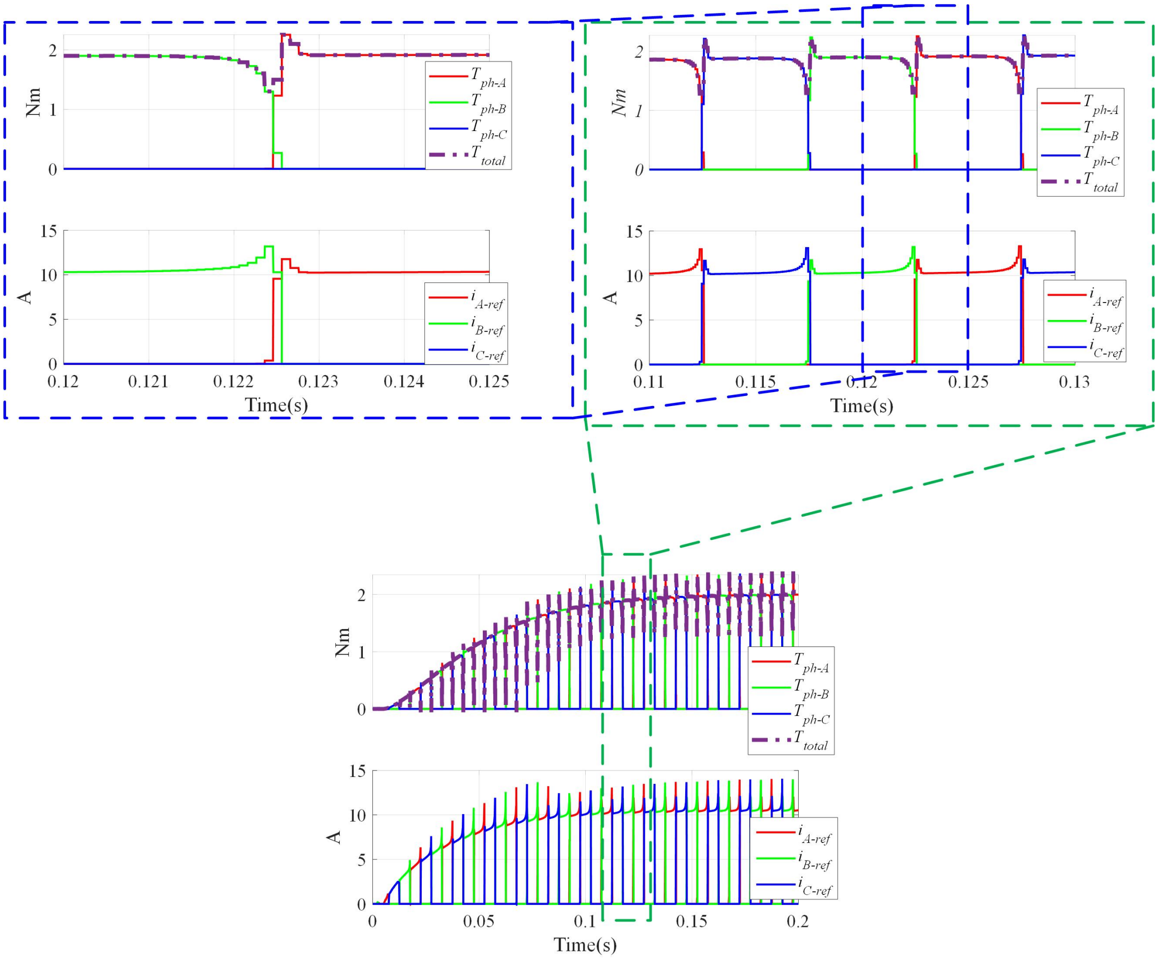

Figure 7.3: Phase current reference identification via 2-D gradient descent algorithm for $T_{ref} = 2Nm$ and speed= 500RPM

for identification of the solution in the subsequent sampling period. As the speed increases, the solutions in consecutive sampling periods tend to get further displaced from each other. Thus, the algorithm is required to perform more iterations to arrive sufficiently close to the real solution. Fig.(7.4) provides a clearer demonstration of this phenomenon. During the phase overlap period, the number of iterations per sampling period required to attain the sufficiently accurate solution is very large and goes beyond the capacity of the micro-controller for real-time implementation.

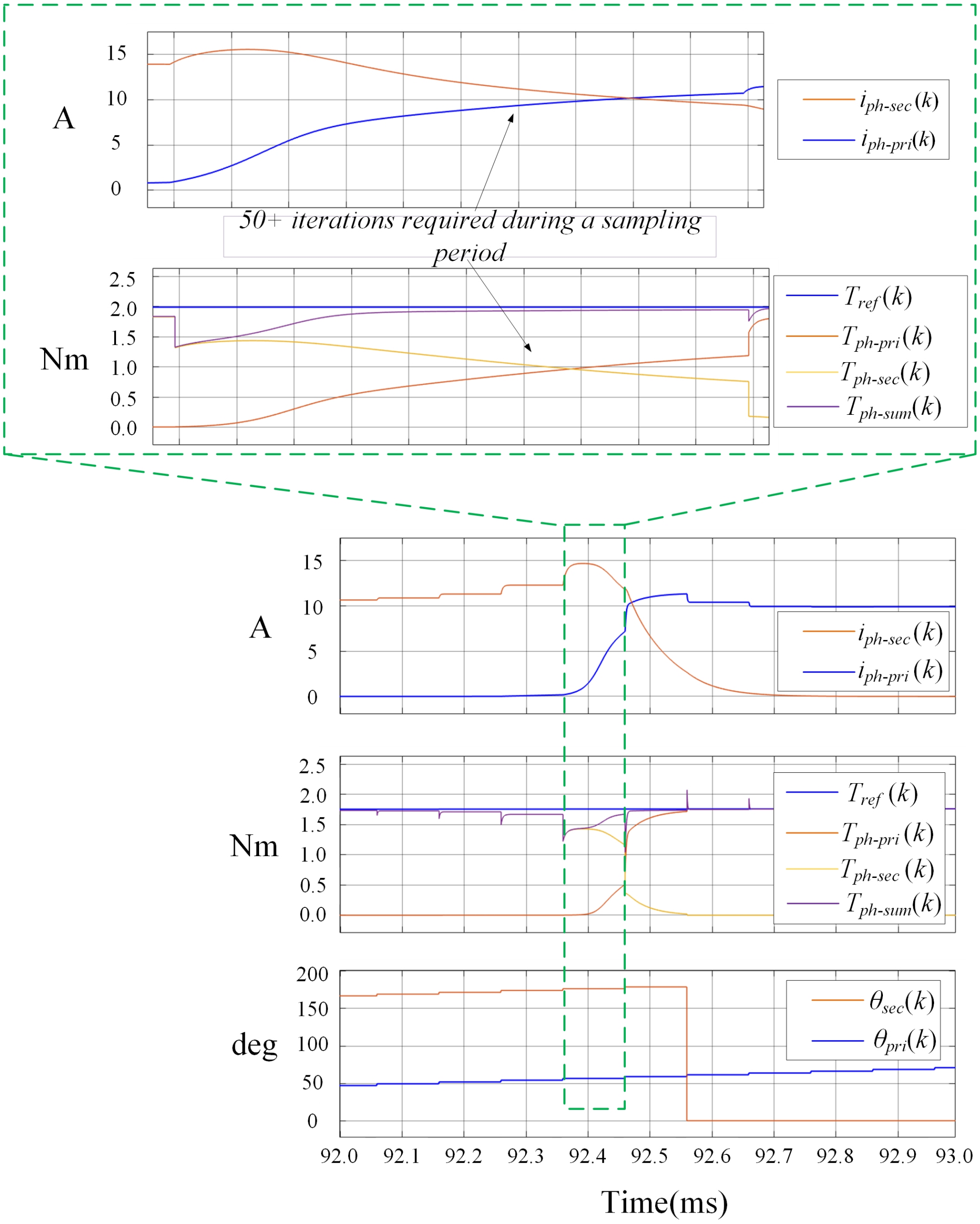

Figure 7.4: Performance of 2-D gradient descent algorithm during phase overlap period

Therefore, the utility of this algorithm is limited up-to a very small operating speed range of the machine.

7.3 Gradient Descent in Parametric Form

Similar to 2-D gradient descent algorithm, the torque and torque gradient characteristics in parametric form gradient descent algorithm are stored in the form of LUTs for online implementation as shown in the Fig.(7.5).

Similar to the study for fixed gradient descent presented in the previous section, the reference torque dynamics are maintained as second-order curves for $T_{ref-ss} = 2Nm$. The simulation is performed for increasing operating speeds up to the base speed and the performance of the algorithm is evaluated in terms of torque ripple magnitude.

Fig.(7.6) shows the simulation results for the operating speed from 500RPM to 2500RPM. The estimated torque ripple grows as the speed increases. The worst case torque ripple is close to $1Nm$ at 2500RPM. The steady state values of the worst case torque ripple are enlisted in the Table 7.1. Although the parametric form gradient descent algorithm performs better that 2-D gradient descent algorithm, its performance is not consistent across the speed range yielding worst case torque ripple = 50%. However, the biggest improvement is seen in terms of the number of iterations required per sampling instant. Thanks to the faster solution method employed in torque error minimization loop, the parametric gradient descent algorithm yields the solution within 4-6 iterations only.

For both the algorithms discussed above, the worst case performance is observed in the phase overlap region. Although splitting the 2-D problem in to two 1-D problems

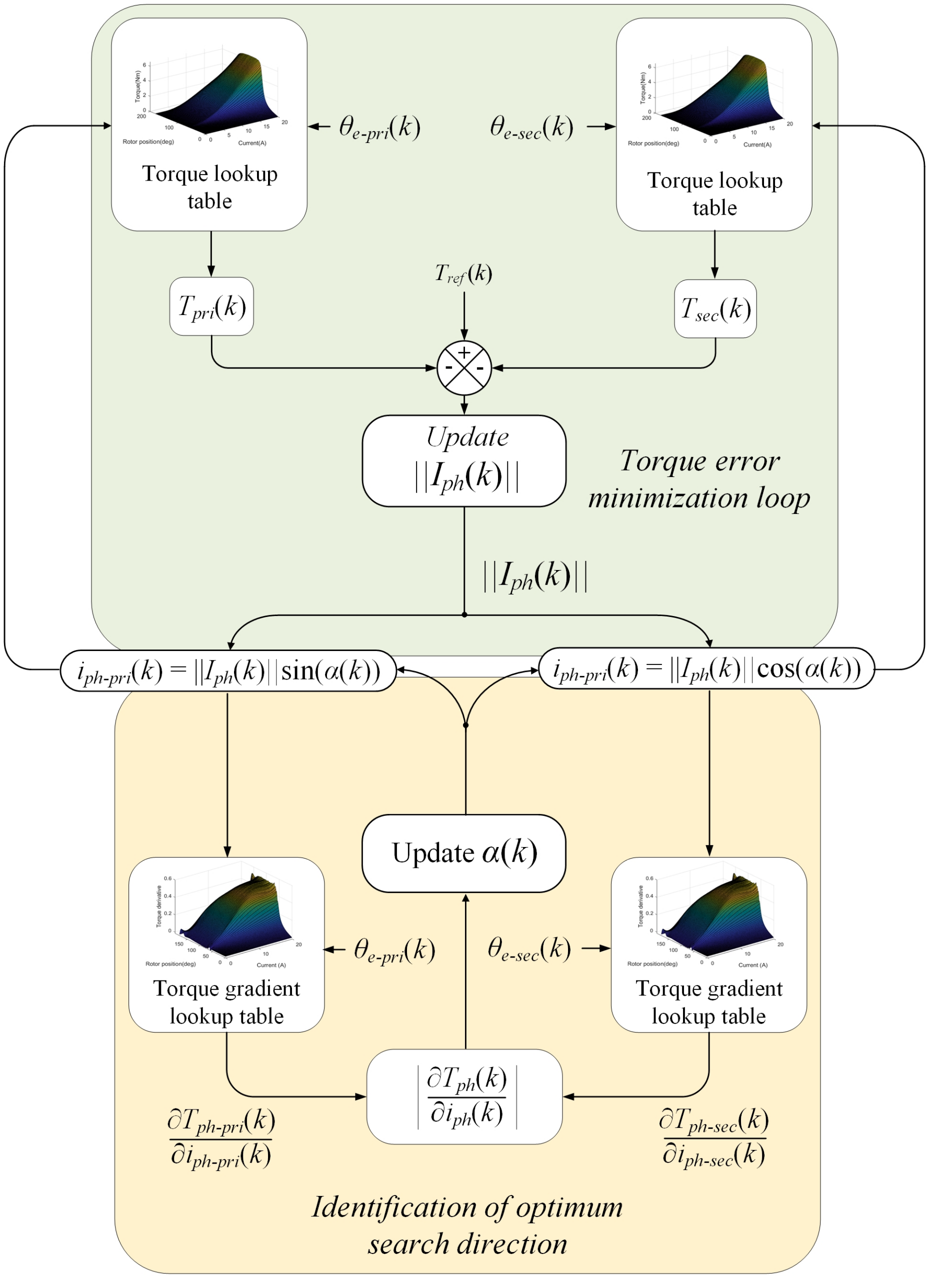

Figure 7.5: Implementation framework for gradient descent algorithm in a parametric form

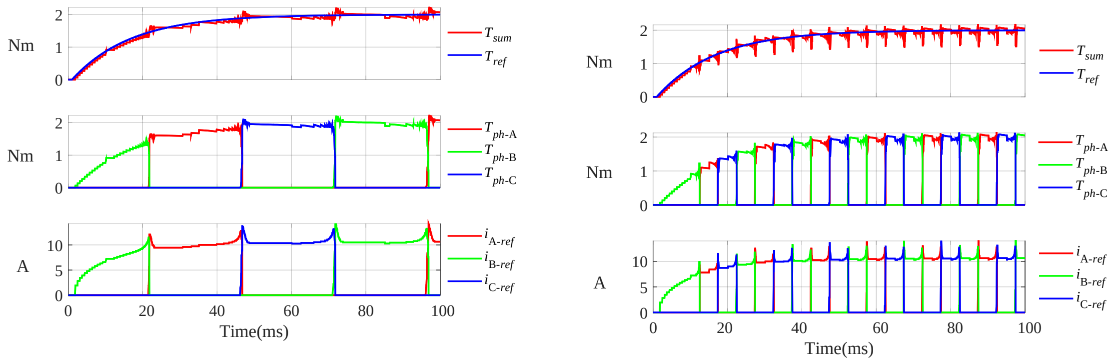

(*a*): 100RPM (*b*): 500RPM

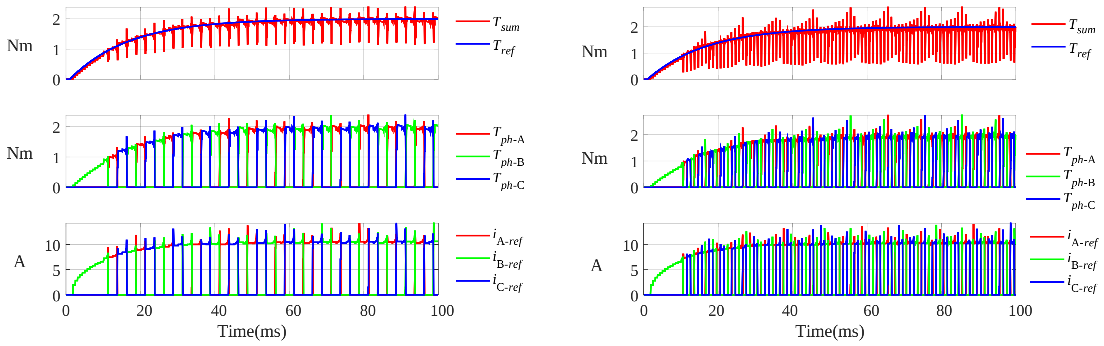

(*c*): 1000RPM (*d*): 2500RPM

Figure 7.6: Performance of the parametric algorithm for $T_{ref-ss} = 2Nm$

Speed(RPM)	$T_{ripple-ss}$
100	5%
500	24%
1000	35%
2500	50%

Table 7.1: Torque ripple percentage as a function of operating speed

improved the performance, the consistency in the solution is still difficult to achieve with parametric form gradient descent algorithm.

The torque ripple at higher speed with of this algorithm can be improved by performing more iteration and improving the $\alpha_{opt}(k)$ identification process near 0^o and 90^o.

7.4 Projected Gradient Descent

Similar to the 2-D gradient descent and parametric form gradient descent methods discussed in the previous sections, the projected gradient descent algorithm uses the torque and torque gradient information in the form of 2-D LUTs for copper loss minimization alone. Two additional 2-D LUTs: mode-0 radial force and torque gradient of the mode-0 radial force are required to perform simultaneous minimization of the copper loss and mode-0 radial force. The implementation frameworks for both the methods are shown in Fig.(7.7) and Fig.(7.8). The torque control performance under copper loss minimization objective for different operating speeds is shown in the Fig.(7.9) in comparison with the parametric form gradient descent, the projected gradient descent algorithm is capable of providing a more consistent dynamic response. Table 7.2 enlists the percentage torque ripple for each operating speed. As expected

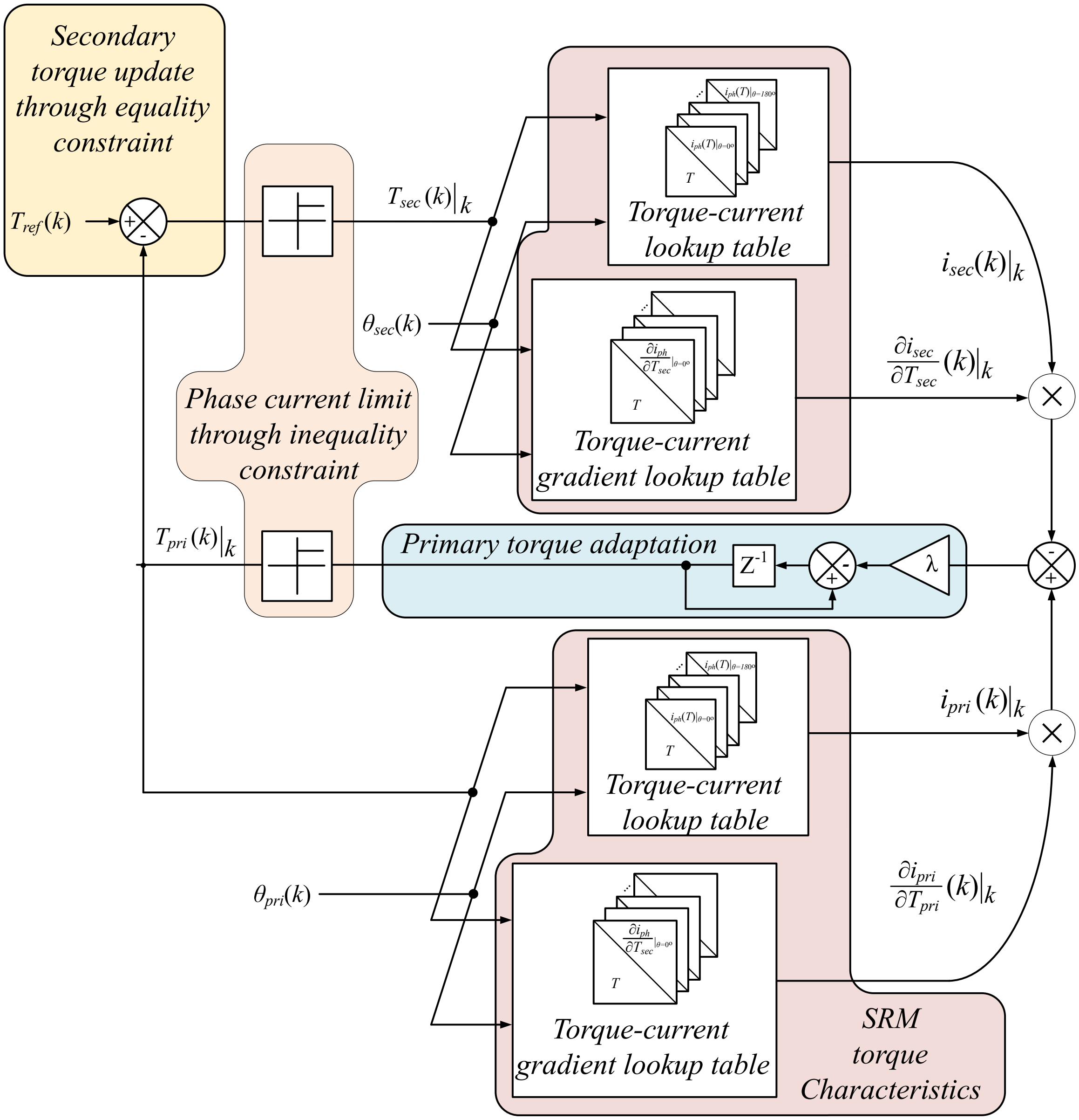

Figure 7.7: Implementation of the projected gradient descent algorithm for copper loss minimization

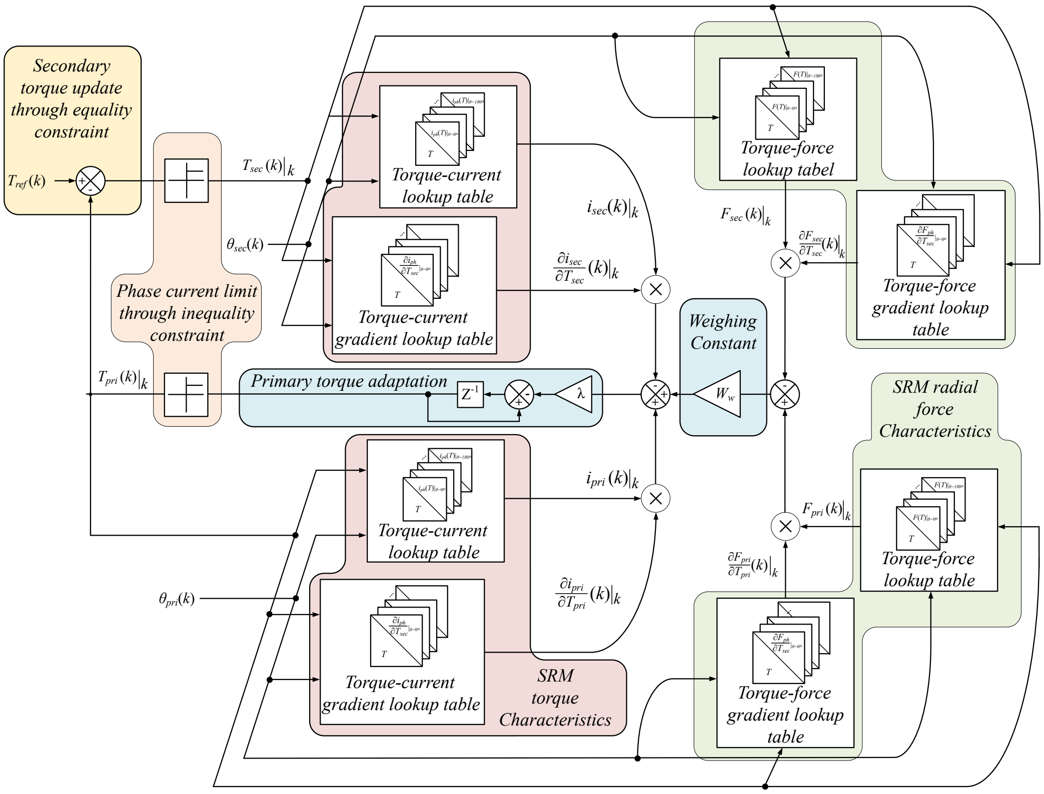

Figure 7.8: Implementation of the projected gradient descent algorithm for simultaneous minimization of copper loss and mode-0 radial force

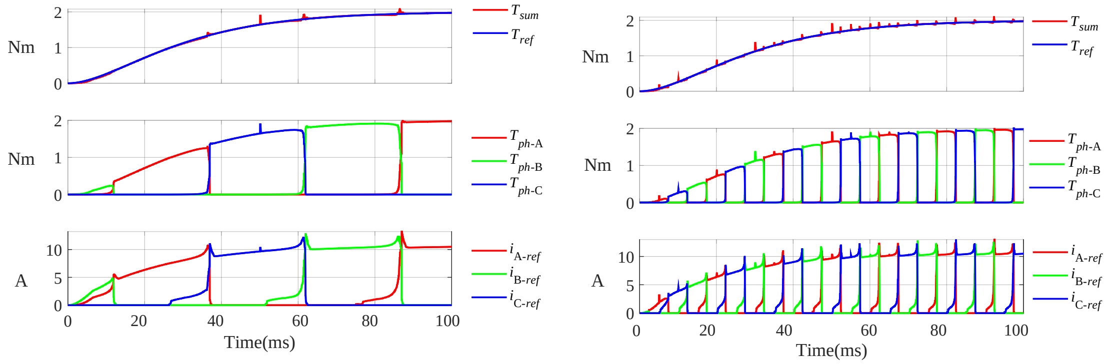

(*a*): 100RPM (*b*): 500RPM

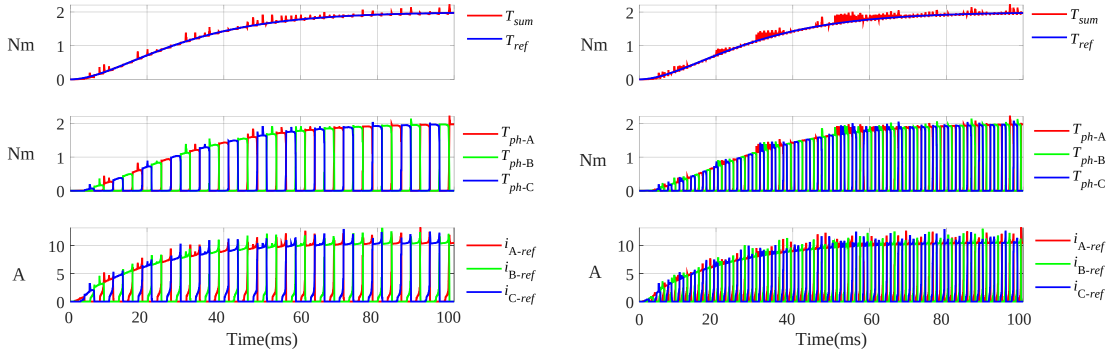

(*c*): 1000RPM (*d*): 2500RPM

Figure 7.9: Performance evaluation of the projected gradient descent algorithm for copper loss minimization at $T_{ref-ss} = 2Nm$

the worst case torque ripple appears during the phase overlap period. It is also observed that the magnitude of this ripple can be reduced by performing larger number of iterations. The simulation results in Fig.(7.9), 10 iterations are performed at each sampling instant for each operating condition.

The performance of the algorithm for combined minimization of copper-loss and mode-0 radial force is shown in Fig.(7.10). It should be noted here that these two

Speed(RPM)	$T_{ripple-ss}$
100	10%
500	10%
1000	14%
2500	20%

Table 7.2: Steady state torque ripple for the projected gradient descent algorithm

objectives are contradictory to each other. Therefore, the peak phase current magnitude is likely to increase for reduction in mode-0 radial force. The simulation results shown in Fig.(7.10) are obtained for a constant value of weighing factor, $W_w = 25$. The performance in terms of torque ripple magnitude is similar to that with the copper loss minimization alone for 10 iterations.

Larger value of W_w corresponds to greater priority to the minimization of mode-0 radial force. Fig.(7.11) shows the torque control performance for two extreme cases: $W_w = 0$ and $W_w = 40$. The former corresponds to copper loss minimization alone while the latter provides maximum priority to mode-0 radial force minimization. These two conditions correspond to the optimum solution trajectories represented in Fig.(6.12). For 2 Nm torque reference, the difference between two trajectories in terms of peak mode-0 radial force and phase current magnitude is presented in Table 7.3.

7.5 Operation over digital control card

The combined minimization of copper loss and mode-0 radial force is evaluated for different operating speeds over TI DSP F28377D digital control card. The evaluation is performed for $T_{ref-ss} = 2Nm$ and mechanical speed varying from 100RPM upto 2500RPM. Fig.(7.12) shows the scope outputs for the two operating speeds: 500RPM

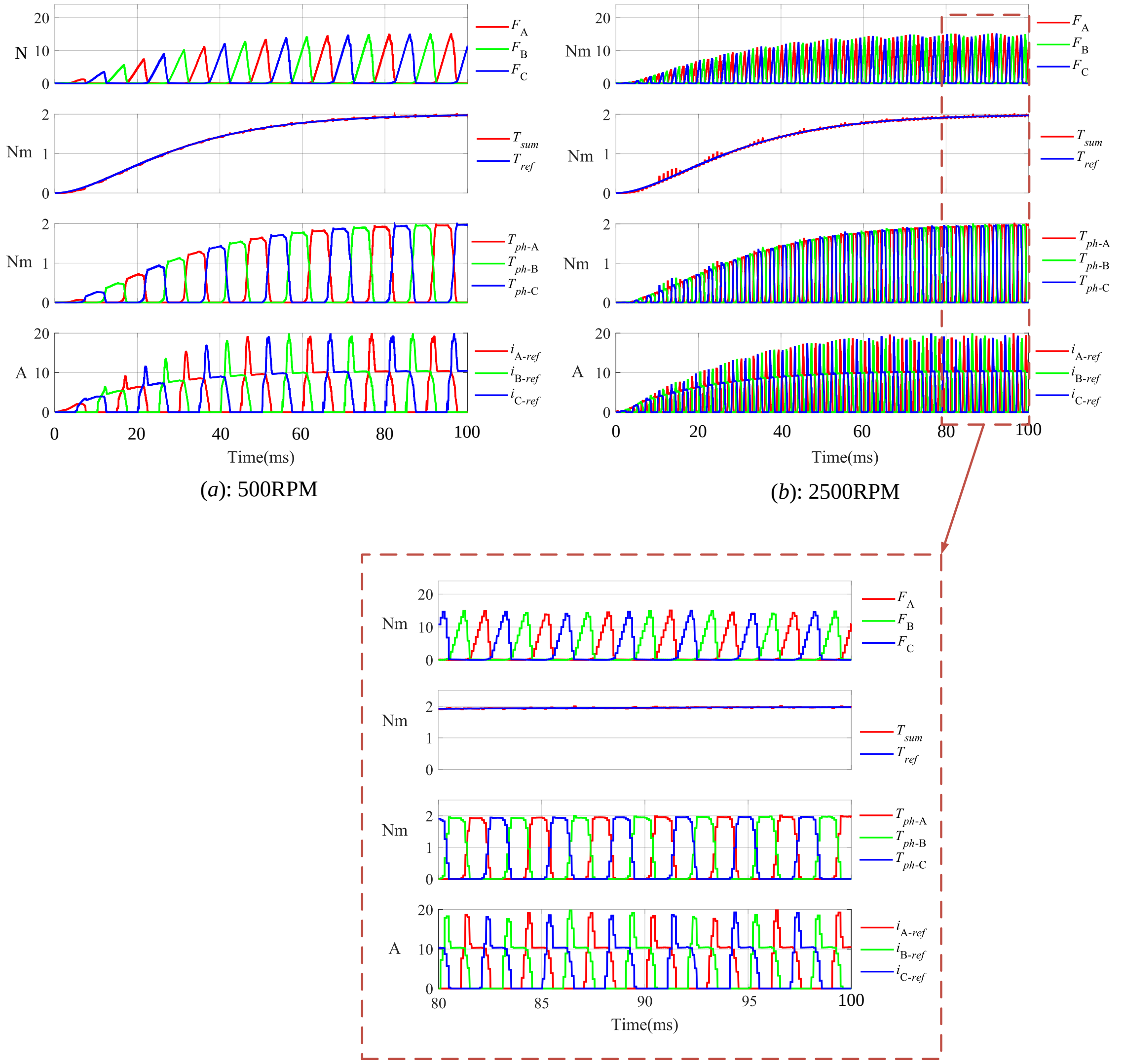

(*a*): 500RPM

(*b*): 2500RPM

Figure 7.10: Simultaneous minimization of mode-0 radial force and copper loss using projected gradient descent algorithm

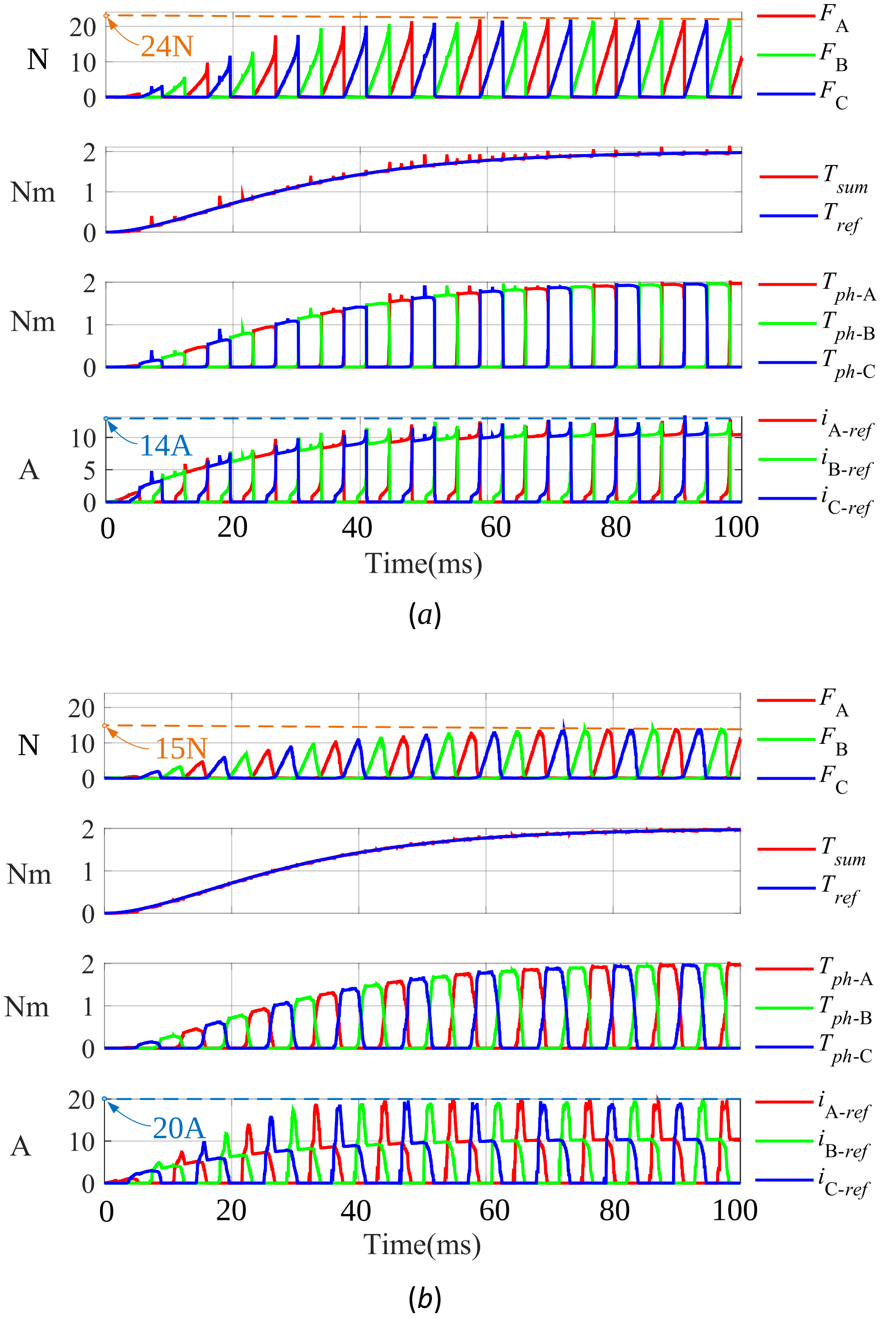

(a)

(b)

Figure 7.11: Torque control performance comparison with (a): Copper-loss minimization alone ($W_w = 0$) and (b): Mode-0 Radial force minimization alone ($W_w = 40$) at 700RPM

Table 7.3: Comparison of the solution trajectories generated from the projected gradient descent algorithm for (1): Copper loss minimization ($W_w = 0$) and (2): Mode-0 radial force minimization ($W_w = 40$)

Parameter	Optimum solution trajectory	
	1: Copper loss minimization	2: Mode-0 radial force minimization
Peak phase current(A)	14	24
Mode-0 radial force(N)	20	15

and 2500RPM.

7.6 Experimental Validation

The performance of the proposed control technique is evaluated over a 3.2kW, 12-8 SRM test drive setup. The first trajectory ($W_w = 0$) prioritizes copper-loss minimization alone results in to the average copper-loss of 56.43W while the peak radial force is 17.5N. On the other hand, the trajectory-2 yields reduced mode-0 radial force magnitude of 13.44N at the expense of increased copper loss by 42.7W. Table 7.4 enlists the variation in the performance indices for both the trajectories. Fig.(7.13) and Fig.(7.14) shows the experimental waveforms for the Trajectory-1 and Trajectory-2 at 500RPM respectively.

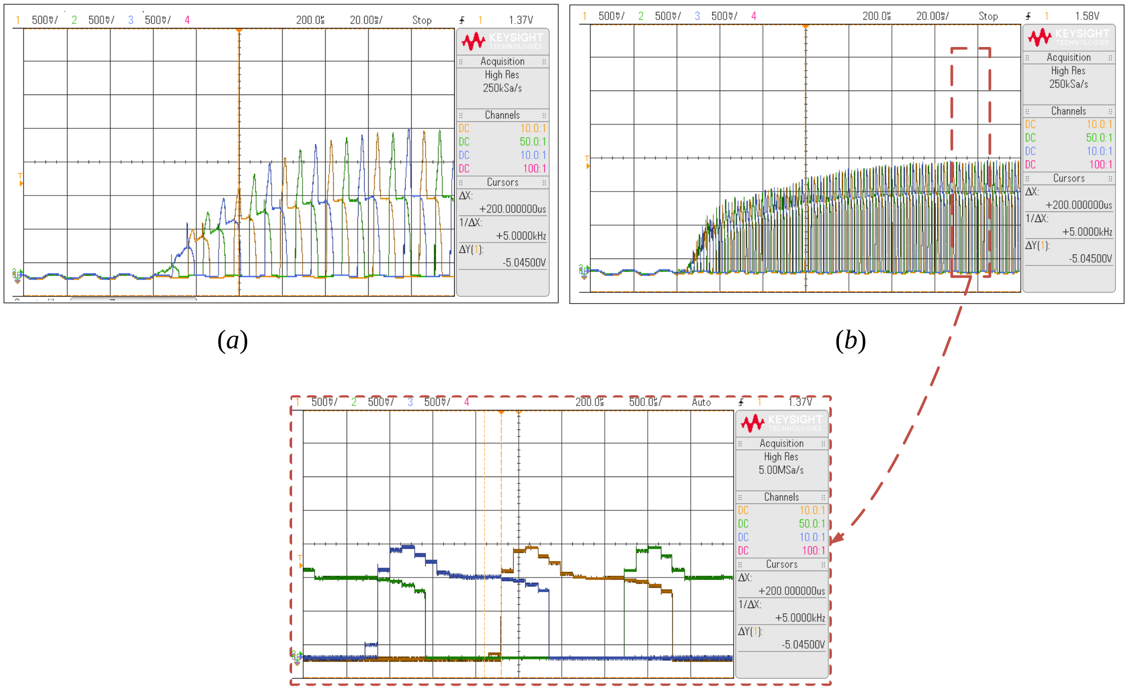

(a) (b)

(c)

Figure 7.12: Experimental verification of the reference current generation for combined minimization of copper loss and mode-0 radial force over digital control card. (a) 500RPM, (b) 2500RPM

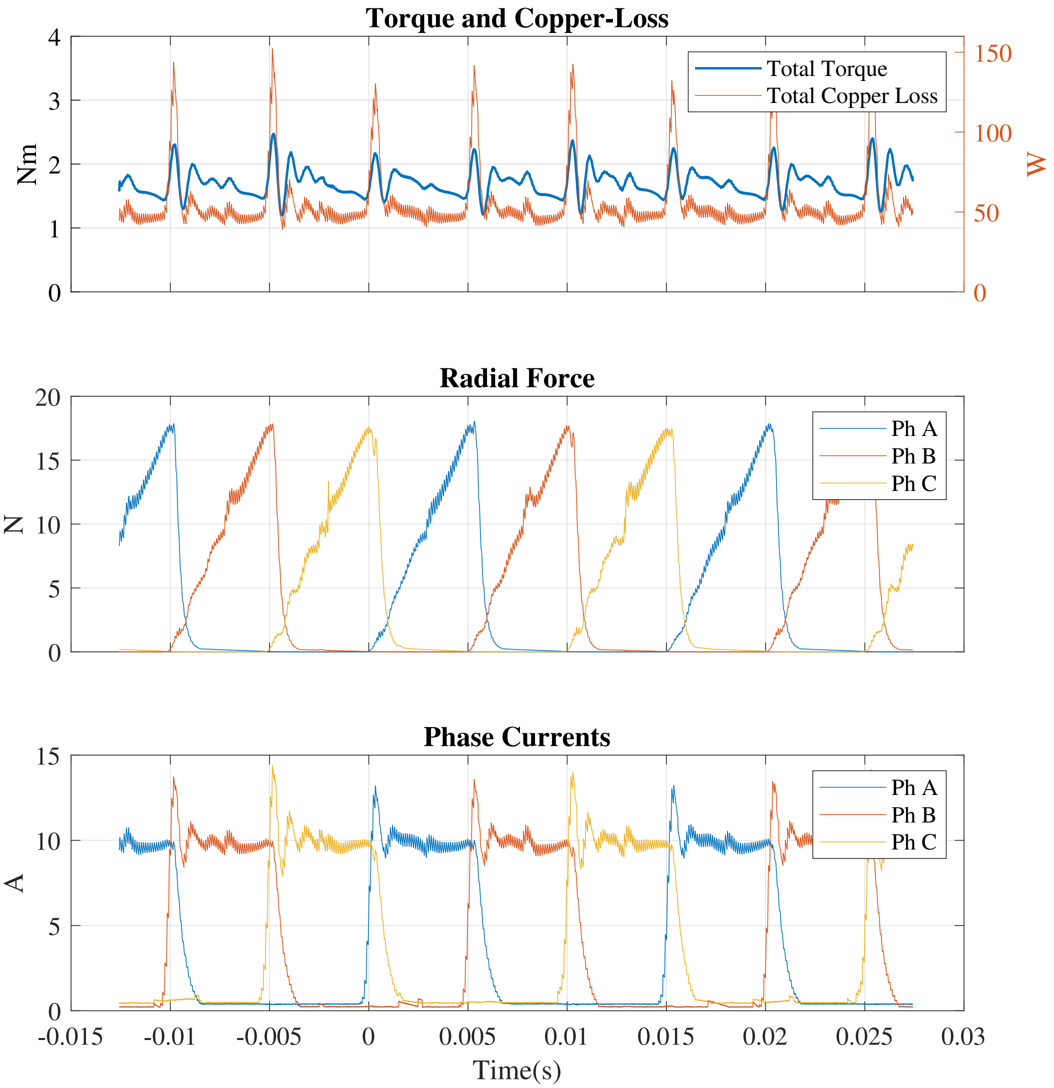

Figure 7.13: Copper-loss minimization ($W_w = 0$) at 500RPM at 2Nm reference torque

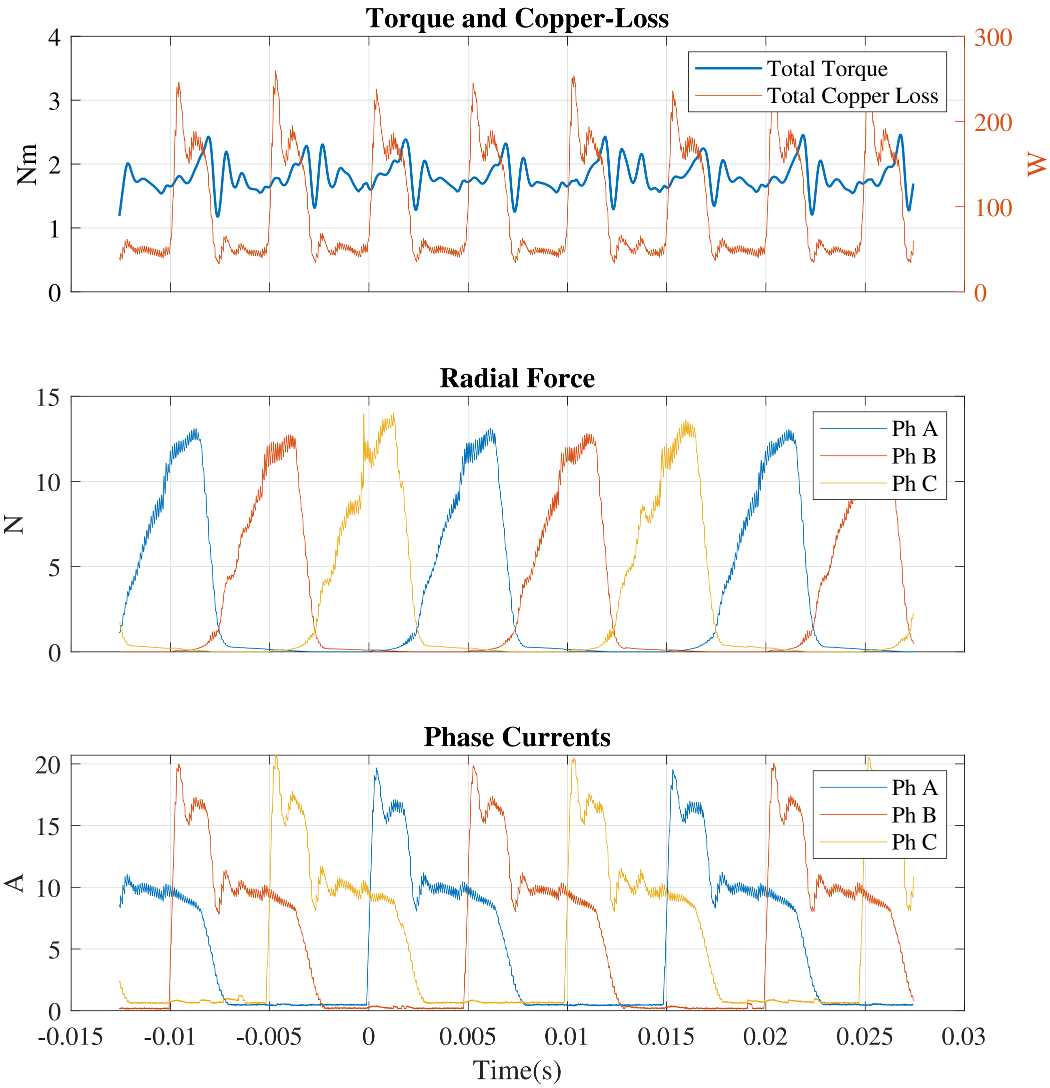

Figure 7.14: Radial-force minimization at 500RPM at 2Nm reference torque

7.7 Summary

Owing to its robustness, the 2-Dimensional gradient descent algorithm is capable of achieving the solution to the nonlinear optimization problem. However, it lacks computational efficiency and it is capable of identifying the solution only for a very small speed range (0-500RPM). The parametric form gradient descent algorithm successfully achieves the solution for the copper loss minimization problem withing 4-6 iterations across the entire controllable operating speed range. Although efficient, this algorithm fails to achieve consistent performance. The magnitude of the worst case torque ripple grows significantly as speed increases and becomes very high at the base speed. The projected gradient descent provides greater consistency in torque ripple reduction across wide speed range. On the other hand, it requires more iterations to achieve the solution as compared to the parametric form gradient descent.

The parametric form gradient descent algorithm is also evaluated for combined minimization of copper loss and mode-0 radial force. Due to the conflicting nature of these objectives, the contribution of primary phase torque as a function of rotor position differ for different priorities for the secondary objectives. As a result of this variation, minimization of one secondary objective results into maximization of the other. In each case however, torque ripple minimization is maintained with good consistency.

Table 7.4: Comparisons of trajectories

Performance index	Trajectory 1	Trajectory 2
Average Cu-loss	56.43W	98.9W
Peak radial force	17.5N	13.44N

Chapter 8

Conclusions and Future Work

This thesis presents an efficient torque control mechanism for SRM drives, capable of maintaining minimum torque ripple at a fixed switching frequency modulation while achieving minimization of the copper-loss and/or mode-0 radial forces.

The problem of SRM torque control improvement through online optimization is rigorously studied in this thesis. Due to the nonlinear characteristics of SRM, the nature of the solution space is highly skewed. Therefore, development of the optimum solution method is a complex process. Since the gradient descent algorithm is unaffected by the inconsistent 2^{nd} derivatives of the objective function with respect to the optimization variables, it is a good candidate for the given problem. However, it does not guarantee best computational efficiency. Nevertheless, a compromise can be achieved by performing the initial iterations with fixed step size and the subsequent iterations with the help of second derivative information. For parametric form gradient descent algorithm, this approach helped reduce the number of iterations significantly.

The last among the proposed algorithms uses torque as an optimization variable.

It achieves transformation to 1-dimension by exploiting the equality constraint to update secondary torque reference as a function of primary torque reference. This algorithm yielded the most efficient among the solution methods presented in this thesis, and it is successfully utilized to perform simultaneous minimization of copper loss and mode-0 radial forces. This aspect is of great importance as it allows for dynamic management of the priorities for these secondary objective based on the operating conditions.

The thesis also presents a comprehensive analysis of the nonlinear electromagnetic characteristics of SRM in discrete-time domain. The most popular SRM current control techniques presented in literature are studied in detail and theoretical evaluations of their performances are presented along with proposed recommendations for improvements. Subsequently, a mode-free current controller is presented. This controller is developed using the principles of digital sliding mode control. Unlike the continuous-time domain SMC, the DSMC performs the compensation of the unmodelled dynamics through delayed disturbance rejection. To overcome the effect of the noise mismatch due to estimation delay, a corrective action is derived through Lyapunov energy function analysis in discrete-time domain. The resultant controller benefits from the online estimation of the nonlinear dynamics while maintaining robustness through the conservative correction effort from the auxiliary controller. The effectiveness of this controller is validated experimentally at low signal to noise ratio until the base speed. The model-free nature of this controller also boasts high computational and memory efficiency.

Except FL, all the model based control techniques presented in the literature, incorporate the electromagnetic characteristics of SRM in the form of LUT's. Therefore, they require multiple interpolations loops which are iterative in nature and hence computationally burdensome. The modern multi-core micro-controllers come with an additional fixed point processor (CLA) with direct access to the ADC output signals. If the controller is implemented within CLA, the main cores can be freed to preform complex operations corresponding to identification of optimum phase current trajectories.

The CLA in the micro-controller used in this thesis, does not support any iterative operation and hence, it can not support LUT based controller implementation. On the other hand, the model-free nature of the proposed current controller makes it suitable for application in CLA, yielding a highly robust and efficient current control solution. Since the current control is entirely performed on CLA, the main CPU cores are free from the corresponding computational burden and they can be devoted entirely for the optimization based identification of current references and condition monitoring.

8.1 Future Work

8.1.1 DC-Link Voltage Utilization

The thesis only considers, copper loss and mode-0 radial force minimization as secondary objectives. Therefore, the resultant phase current references attain a large magnitude near fully aligned position. This effect is more significant when only copper-loss minimization is performed. Due to limited DC-link voltage, it is not possible to track these references at high speed. Therefore, the effective operating range of the SRM drive gets restricted. This effect can be countered by incorporating the objective of voltage utilization through flux linkage characteristics as following.

$$\min_{T_{ph}} \quad I_{ph}^T I_{ph} + W_w \|F_e\| + W_v \left\| \frac{\Delta\psi_{ph}}{\omega_e} \right\|_\infty \tag{8.1a}$$

$$\text{subject to} \quad |T_{ph}| - T_e = 0, \tag{8.1b}$$

$$0 \leq \|T_{ph}(\theta_e)\|_\infty \leq T_{max}(\theta_e) \tag{8.1c}$$

8.1.2 Exclusion of Rotor Position Feedback

The electromagnetic torque and force characteristics used in the optimization process were modelled as functions of rotor position and phase current. These characteristics can also be modelled as functions of flux linkage and phase current. This provision excludes the need for rotor position measurement. However, it is very sensitive to flux linkage estimation.

8.1.3 Geometries with Significant Mutual Coupling Effect

The SRM used in the presented analysis consists of low mutual coupling effect. Therefore, its effect on the phase torque can be conveniently neglected.

The high torque density SRM configurations often exhibit high mutual coupling between the successive phases. In such cases, the electromagnetic torque and force characteristics used for online optimization must also include this effect which can also significantly influence the nature of the solution space.

References

(2018). 179-analysis of sr motor static characteristics. Technical report.

Abdel-Maksoud, H. (2020). A hybrid torque sharing function with controlled commutation period for torque ripple minimization in srm.

Ahmad, S. S. and Narayanan, G. (2016). Linearized modeling of switched reluctance motor for closed-loop current control. *IEEE Transactions on Industry Applications*, **52**(4), 3146–3158.

Ahmad, S. S. and Narayanan, G. (2016). Linearized modeling of switched reluctance motor for closed-loop current control. *IEEE Transactions on Industry Applications*, **52**(4), 3146–3158.

Ahmad, S. S. and Narayanan, G. (2018). Predictive control based constant current injection scheme for characterization of switched reluctance machine. *IEEE Transactions on Industry Applications*, **54**(4), 3383–3392.

Al-Amyal, F., Al Quraan, L., and Szamel, L. (2020). Torque sharing function optimization for extended speed range control in switched reluctance motor drive. In *2020 IEEE 3rd International Conference and Workshop in Óbuda on Electrical and Power Engineering (CANDO-EPE)*, pages 000119–000124. IEEE.

Alharkan, H. A., Saadatmand, S., Ferdowsi, M., and Shamsi, P. (2020). Optimal tracking current control of switched reluctance motor drives using reinforcement q-learning scheduling. *arXiv preprint arXiv:2006.07764*.

Alonge, F., Cirrincione, M., D'Ippolito, F., Pucci, M., and Sferlazza, A. (2017). Robust active disturbance rejection control of induction motor systems based on additional sliding-mode component. *IEEE Transactions on Industrial Electronics*, **64**(7), 5608–5621.

Amor, L. B., Dessaint, L. ., Akhrif, O., and Olivier, G. (1992). Adaptive feedback linearization for position control of a switched reluctance motor: analysis and simulation. In *Proceedings of the 1992 International Conference on Industrial Electronics, Control, Instrumentation, and Automation*, pages 150–159 vol.1.

Amor, L. B., Akhrif, O., Dessaint, L. A., and Olivier, G. (1993). Adaptive nonlinear torque control of a switched reluctance motor. In *1993 American Control Conference*, pages 2831–2836. IEEE.

Anderson, B. D. and Moore, J. B. (2007). *Optimal control: linear quadratic methods*. Courier Corporation.

Anuchin, A., Demidova, G. L., Hao, C., Zharkov, A., Bogdanov, A., and Šmídl, V. (2020). Continuous control set model predictive control of a switch reluctance drive using lookup tables. *Energies*, **13**(13), 3317.

Åström, K. J. (1991). Adaptive control. In *Mathematical System Theory*, pages 437–450. Springer.

Bae, H.-K., Lee, B.-S., Vijayraghavan, P., and Krishnan, R. (2000). A linear switched reluctance motor: converter and control. *IEEE Transactions on Industry Applications*, **36**(5), 1351–1359.

Banque, B., Perat, J., Andrada, P., and Torrent, M. (2005). Improving efficiency in switched reluctance motor drives with online control of turn-on and turn-off angles. In *2005 European Conference on Power Electronics and Applications*, pages P.1 – P.9, Dresden.

Belfore, L. A. and Arkadan, A.-R. (1997). Modeling faulted switched reluctance motors using evolutionary neural networks. *IEEE transactions on industrial electronics*, **44**(2), 226–233.

Ben Salem, F., Bahri, I., Maamri, H., and Derbel, N. (2020). A second-order sliding mode control of switched reluctance motor. *Electric Power Components and Systems*, **48**(6-7), 640–651.

Besenyei, A. (2012). A brief history of the mean value theorem. *Talk slides, September*, **12**.

Bilgin, B., Jiang, J. W., and Emadi, A. (2019). *Switched reluctance motor drives: fundamentals to applications*. CRC Press.

Bilgin, B., Howey, B., Callegaro, A. D., Liang, J., Kordic, M., Taylor, J., and Emadi, A. (2020). Making the case for switched reluctance motors for propulsion applications. *IEEE Transactions on Vehicular Technology*, **69**(7), 7172–7186.

Bimbhra, P. (2010). Electrical machinery. *khanna publishers, New Delhi.*

Blaabjerg, F., Kjaer, P. C., Rasmussen, P. O., and Cossar, C. (1999). Improved digital current control methods in switched reluctance motor drives. *IEEE Transactions on power electronics*, **14**(3), 563–572.

Bolognani, S. and Zigliotto, M. (1996). Fuzzy logic control of a switched reluctance motor drive. *IEEE Transactions on Industry Applications*, **32**(5), 1063–1068.

Bortoff, S. A., Kohan, R. R., and Milman, R. (1998). Adaptive control of variable reluctance motors: a spline function approach. *IEEE Transactions on Industrial Electronics*, **45**(3), 433–444.

Bose, B. K. (2020). *Power electronics and motor drives: advances and trends*. Academic press.

Bostanci, E., Moallem, M., Parsapour, A., and Fahimi, B. (2017). Opportunities and challenges of switched reluctance motor drives for electric propulsion: A comparative study. *IEEE transactions on transportation electrification*, **3**(1), 58–75.

Boyd, S. and Sastry, S. S. (1986). Necessary and sufficient conditions for parameter convergence in adaptive control. *Automatica*, **22**(6), 629–639.

Brauer, H. J., Hennen, M. D., and De Doncker, R. W. (2011). Control for polyphase switched reluctance machines to minimize torque ripple and decrease ohmic machine losses. *IEEE Transactions on Power Electronics*, **27**(1), 370–378.

Callegaro, A. D., Bilgin, B., and Emadi, A. (2019). Radial force shaping for acoustic noise reduction in switched reluctance machines. *IEEE Transactions on Power Electronics*, **34**(10), 9866–9878.

Cardenas, R., Pena, R., Perez, M., Clare, J., Asher, G., and Wheeler, P. (2005). Control of a switched reluctance generator for variable-speed wind energy applications. *IEEE transactions on Energy conversion*, **20**(4), 781–791.

Chan, C. (2002). The state of the art of electric and hybrid vehicles. *Proceedings of the IEEE*, **90**(2), 247–275.

Choi, J.-W. and Sul, S.-K. (1996). Inverter output voltage synthesis using novel dead time compensation. *IEEE transactions on Power Electronics*, **11**(2), 221–227.

Chowdhuri, S., Biswas, S. K., and Mukherjee, A. (2006). Performance studies of fuzzy logic based pi-like controller designed for speed control of switched reluctance motor. In *2006 1ST IEEE Conference on Industrial Electronics and Applications*, pages 1–5. IEEE.

Chowdhuri, S., Biswas, S. K., and Mukherjee, A. (2006). Performance studies of fuzzy logic based pi-like controller designed for speed control of switched reluctance motor. In *2006 1ST IEEE Conference on Industrial Electronics and Applications*.

Dannehl, J., Fuchs, F. W., Hansen, S., and Thøgersen, P. B. (2010). Investigation of active damping approaches for pi-based current control of grid-connected pulse width modulation converters with lcl filters. *IEEE Transactions on Industry Applications*, **46**(4), 1509–1517.

de Paula, M. V. and Barros, T. A. D. S. (2021). A sliding mode ditc cruise control for srm with steepest descent minimum torque ripple point tracking. *IEEE Transactions on Industrial Electronics*.

de Paula, M. V., dos Santos Barros, T. A., and Neto, P. (2020). A review of classic torque control techniques for switched reluctance motors. In *Modelling and Control of Switched Reluctance Machines*, page 247. IntechOpen.

Dhale, S., Nahid-Mobarakeh, B., and Emadi, A. (2021). A review of fixed switching frequency current control techniques for switched reluctance machines. *IEEE Access*, **9**, 39375–39391.

Divandari, M., Rezaie, B., and Amiri, E. (2020). Robust speed control of switched reluctance motor drive based on full order terminal sliding mode control. In *2020 IEEE Applied Power Electronics Conference and Exposition (APEC)*, pages 2423–2428. IEEE.

Drakunov, S. V. and Utkin, V. (1990). On discrete-time sliding modes. In *Nonlinear Control Systems Design 1989*, pages 273–278. Elsevier.

Espinosa-Pérez, G., Maya-Ortiz, P., Velasco-Villa, M., and Sira-Ramírez, H. (2004). Passivity-based control of switched reluctance motors with nonlinear magnetic circuits. *IEEE Transactions on Control Systems Technology*, **12**(3), 439–448.

Eweda, E. and Macchi, O. (1987). Convergence of the rls and lms adaptive filters. *IEEE Transactions on Circuits and Systems*, **34**(7), 799–803.

Fadhel, S., Bahri, I., and Zhang, M. (2017). H-infinity controller design for the switched reluctance machine. *International Journal of Mechanical and Mechatronics Engineering*, **11**(1), 132 – 141.

Fiedler, J. O., Kasper, K. A., and De Doncker, R. W. (2006). Spectral composition of stator vibrations resulting from modal superposition in srm.

Fisch, J. H., Li, Y., Kjaer, P., Gribble, J., and Miller, T. (1997). Pareto-optimal firing angles for switched reluctance motor control.

Francis, B. A. (1987). Lecture notes in control and information sciences.

Frobenius, G. (1895). *Verallgemeinerung des Sylow'schen satzes*. Reimer.

Gallegos-López, G. and Rajashekara, K. (2002). Peak pwm current control of switched reluctance and ac machines. In *Conference Record of the 2002 IEEE Industry Applications Conference. 37th IAS Annual Meeting (Cat. No. 02CH37344)*, volume 2, pages 1212–1218. IEEE.

Gan, C., Wu, J., Sun, Q., Yang, S., Hu, Y., and Jin, L. (2016). Low-cost direct instantaneous torque control for switched reluctance motors with bus current detection under soft-chopping mode. *IET Power Electronics*, **9**(3), 482–490.

Gan, C., Wu, J., Sun, Q., Kong, W., Li, H., and Hu, Y. (2018). A review on machine topologies and control techniques for low-noise switched reluctance motors in electric vehicle applications. *IEEE Access*, **6**, 31430–31443.

Garrigan, N. R., Soong, W. L., Stephens, C. M., Storace, A., and Lipo, T. A. (1999). Radial force characteristics of a switched reluctance machine. In *Conference Record of the 1999 IEEE Industry Applications Conference. Thirty-Forth IAS Annual Meeting (Cat. No. 99CH36370)*, volume 4, pages 2250–2258. IEEE.

Haiqing, Y., Panda, S. K., and Chii, L. Y. (1996). Performance comparison of sliding mode control with pi control for four-quadrant operation of switched reluctance motors. In *Proceedings of International Conference on Power Electronics, Drives and Energy Systems for Industrial Growth*, volume 1, pages 381–387. IEEE.

Han, J. (2009). From pid to active disturbance rejection control. *IEEE transactions on Industrial Electronics*, **56**(3), 900–906.

Hannoun, H., Hilairet, M., and Marchand, C. (2011a). High performance current control of a switched reluctance machine based on a gain-scheduling pi controller. *Control Engineering Practice*, **19**(11), 1377–1386.

Hannoun, H., Hilairet, M., and Marchand, C. (2011b). High performance current control of a switched reluctance machine based on a gain-scheduling pi controller. *Control Engineering Practice*, **19**(11), 1377 – 1386.

Hao, C. and Pavlitov, C. (2009). Large power analysis of switched reluctance machine system for coal mine. *Mining Science and Technology (China)*, **19**(5), 657–659.

Harikrishnan, R. and Fernandez, F. M. (2016). Improved online torque-sharing-function based low ripple torque control of switched reluctance motor drives. In *2016 IEEE International Conference on Power Electronics, Drives and Energy Systems (PEDES)*, pages 1–6. IEEE.

Hasegawa, M., Tanaka, N., Chiba, A., and Fukao, T. (2002). The operation analysis and efficiency improvement of switched reluctance motors with high silicon steel. In *Proceedings of the Power Conversion Conference-Osaka 2002 (Cat. No. 02TH8579)*, volume 3, pages 981–986. IEEE.

Hashemnia, N. and Asaei, B. (2008). Comparative study of using different electric motors in the electric vehicles. In *2008 18th International Conference on Electrical Machines*, pages 1–5. IEEE.

Hofmann, A., Al-Dajani, A., Bösing, M., and De Doncker, R. W. (2013). Direct instantaneous force control: A method to eliminate mode-0-borne noise in switched reluctance machines. In *2013 International Electric Machines & Drives Conference*, pages 1009–1016. IEEE.

Husain, I. (2002). Minimization of torque ripple in srm drives. *IEEE transactions on Industrial Electronics*, **49**(1), 28–39.

Husain, I. and Ehsani, M. (1996). Torque ripple minimization in switched reluctance motor drives by pwm current control. *IEEE transactions on power electronics*, **11**(1), 83–88.

Ilic, M., Marino, R., Peresada, S., Taylor, D., *et al.* (1987). Feedback linearizing control of switched reluctance motors. *IEEE Transactions on Automatic Control*, **32**(5), 371–379.

Ilic'-Spong, M., Marino, R., Peresada, S., and Taylor, D. (1987). Feedback linearizing control of switched reluctance motors. *IEEE Transactions on Automatic Control*, **32**(5), 371–379.

Ilic-Spong, M., Miller, T. J., MacMinn, S. R., and Thorp, J. S. (1987). Instantaneous torque control of electric motor drives. *IEEE Transactions on Power Electronics*, (1), 55–61.

Inderka, R. B. and De Doncker, R. W. (2003a). Ditc-direct instantaneous torque control of switched reluctance drives. *IEEE Transactions on Industry Applications*, **39**(4), 1046–1051.

Inderka, R. B. and De Doncker, R. W. (2003b). High-dynamic direct average torque control for switched reluctance drives. *IEEE Transactions on Industry Applications*, **39**(4), 1040–1045.

Isfahani, M. N., Saghaian-Nejad, S., Rashidi, A., and Zarchi, H. A. (2011). Passivity-based adaptive sliding mode speed control of switched reluctance motor drive considering torque ripple reduction. In *2011 IEEE International Electric Machines & Drives Conference (IEMDC)*, pages 1480–1485. IEEE.

Isidori, A. (2013). *Nonlinear control systems*. Springer Science & Business Media.

Jacobson, C. A., Stankovic, A. M., Tadmor, G., and Coric, Z. (1995). A family of robust control strategies for switched reluctance motors. In *Proceedings of 1995 International Conference on Power Electronics and Drive Systems. PEDS 95*, pages 192–197. IEEE.

Jiang, J. W., Bilgin, B., Howey, B., and Emadi, A. (2015). Design optimization of switched reluctance machine using genetic algorithm. In *2015 IEEE International Electric Machines & Drives Conference (IEMDC)*, pages 1671–1677. IEEE.

Johnstone, R. M., Johnson Jr, C. R., Bitmead, R. R., and Anderson, B. D. (1982). Exponential convergence of recursive least squares with exponential forgetting factor. *Systems & Control Letters*, **2**(2), 77–82.

Kalman, R. E. (1960). On the general theory of control systems. In *Proceedings First International Conference on Automatic Control, Moscow, USSR*, pages 481–492.

Kamalakannan, C., Kamaraj, V., Paramasivam, S., and Paranjothi, S. (2011).

Switched reluctance machine in automotive applications—a technology status review. In *2011 1st International Conference on Electrical Energy Systems*, pages 187–197. IEEE.

Karakas, E. and Vardarbasi, S. (2007). Speed control of sr motor by self-tuning fuzzy pi controller with artificial neural network. *Sadhana*, **32**(5), 587–596.

Karakas, E. and Vardarbasi, S. (2007). Speed control of sr motor by self-tuning fuzzy pi controller with artificial neural network. *IEEE Transactions on Industrial Electronics*, **32**(5), 587–596.

Keerthana, C. and Sundaram, M. (2020). State of art of control techniques adopted for torque ripple minimization in switched reluctance motor drives. In *2020 4th International Conference on Trends in Electronics and Informatics (ICOEI)(48184)*, pages 105–110. IEEE.

Kim, T.-I., Han, J.-S., Oh, T.-H., Kim, Y.-S., Lee, S.-H., *et al.* (2019). A new accurate discretization method for high-frequency component mechatronics systems. *Mechatronics*, **62**, 102250.

Kirk, D. E. (2004). *Optimal control theory: an introduction.* Courier Corporation.

Kiumarsi-Khomartash, B., Lewis, F. L., Naghibi-Sistani, M.-B., and Karimpour, A. (2013). Optimal tracking control for linear discrete-time systems using reinforcement learning. In *52nd IEEE Conference on Decision and Control*, pages 3845–3850. IEEE.

Klein-Hessling, A., Hofmann, A., and De Doncker, R. W. (2017). Direct instantaneous torque and force control: a control approach for switched reluctance machines. *IET Electric Power Applications*, **11**(5), 935–943.

Krishnan, R. (2017). *Switched reluctance motor drives: modeling, simulation, analysis, design, and applications*. CRC press.

Lawrenson, P. (1965). Development and application of reluctance motors. *Electronics and Power*, **11**(6), 195–198.

Lawrenson, P. and Agu, L. (1964). Theory and performance of polyphase reluctance machines. In *Proceedings of the Institution of Electrical Engineers*, volume 111, pages 1435–1445. IET.

Lee, D.-H., Liang, J., Lee, Z.-G., and Ahn, J.-W. (2009). A simple nonlinear logical torque sharing function for low-torque ripple sr drive. *IEEE Transactions on Industrial Electronics*, **56**(8), 3021–3028.

Li, G., Ojeda, X., Hlioui, S., Hoang, E., Gabsi, M., and Balpe, C. (2009). Comparative study of switched reluctance motors performances for two current distributions and excitation modes. In *2009 35th Annual Conference of IEEE Industrial Electronics*, pages 4047–4052. IEEE.

Li, G., Zhu, Z., Ma, X., and Jewell, G. (2016). Comparative study of torque production in conventional and mutually coupled srms using frozen permeability. *IEEE Transactions on Magnetics*, **52**(6), 1–9.

Li, H., Bilgin, B., and Emadi, A. (2018). An improved torque sharing function for torque ripple reduction in switched reluctance machines. *IEEE Transactions on Power Electronics*, **34**(2), 1635–1644.

Li, X. and Shamsi, P. (2015a). Inductance surface learning for model predictive current control of switched reluctance motors. *IEEE Transactions on Transportation Electrification*, **1**(3), 287–297.

Li, X. and Shamsi, P. (2015b). Model predictive current control of switched reluctance motors with inductance auto-calibration. *IEEE Transactions on Industrial Electronics*, **63**(6), 3934–3941.

Liaw, C.-M., Lu, M.-Z., Jhou, P.-H., and Chou, K.-Y. (2020). Some basic and key issues of switched-reluctance machine systems. In *Modelling and Control of Switched Reluctance Machines*, page 221. IntechOpen.

Lin, Z., Reay, D., Williams, B., and He, X. (2010). High-performance current control for switched reluctance motors based on on-line estimated parameters. *IET electric power applications*, **4**(1), 67–74.

Lin, Z., Reay, D., Williams, B., and He, X. (2010). High-performance current control for switched reluctance motors based on on-line estimated parameters. *IET Electric Power Applications*, **4**(1), 67–74.

Liu, C., Chau, K., Lee, C. H., and Song, Z. (2020). A critical review of advanced electric machines and control strategies for electric vehicles. *Proceedings of the IEEE*.

Lu, W., Keyhani, A., and Fardoun, A. (2003). Neural network-based modeling and parameter identification of switched reluctance motors. *IEEE transactions on energy conversion*, **18**(2), 284–290.

Mademlis, C. and Kioskeridis, I. (2003). Performance Optimization in Switched Reluctance Motor Drives With Online Commutation Angle Control. *IEEE Transactions on Energy Conversion*, **18**(3), 448–457.

Maksoud, H. (2020). Torque ripple minimization of a switched reluctance motor using a torque sharing function based on the overlap control technique. *Engineering, Technology & Applied Science Research*, **10**(2), 5371–5376.

Mikail, R., Husain, I., Sozer, Y., Islam, M. S., and Sebastian, T. (2013). Torque-ripple minimization of switched reluctance machines through current profiling. *IEEE Transactions on Industry Applications*, **49**(3), 1258–1267.

Mikail, R., Husain, I., Sozer, Y., Islam, M. S., and Sebastian, T. (2014). A fixed switching frequency predictive current control method for switched reluctance machines. *IEEE Transactions on Industry Applications*, **50**(6), 3717–3726.

Naitoh, H. and Ishikawa, H. (2010). A current controller for a switched reluctance motor based on model reference adaptive control. In *SPEEDAM 2010*, pages 1270–1275. IEEE.

Namazi, M. M., Rashidi, A., Saghaian-Nejad, S. M., and Jin-Woo Ahn (2016). Chattering-free robust adaptive sliding-mode control for switched reluctance motor drive. In *2016 IEEE Transportation Electrification Conference and Expo, Asia-Pacific (ITEC Asia-Pacific)*, pages 474–478.

Neuhaus, C. R., Fuengwarodsakul, N. H., and De Doncker, R. W. (2006). Predictive pwm-based direct instantaneous torque control of switched reluctance drives. In *2006 37th IEEE Power Electronics Specialists Conference*, pages 1–7. IEEE.

Ouddah, N., Boukhnifer, M., Chaibet, A., Monmasson, E., and Berthelot, E. (2014). Experimental robust h_∞ controller design of switched reluctance motor for electrical vehicle application. In *2014 IEEE Conference on Control Applications (CCA)*, pages 1570–1575. IEEE.

Panda, S. and Dash, P. (1996). Application of nonlinear control to switched reluctance motors: a feedback linearisation approach. *IEE Proceedings-Electric Power Applications*, **143**(5), 371–379.

Panda, S. K. and Dash, P. K. (1996). Application of nonlinear control to switched reluctance motors: a feedback linearisation approach. *IEE Proceedings - Electric Power Applications*, **143**(5), 371–379.

Peng, F., Ye, J., and Emadi, A. (2015). A digital pwm current controller for switched reluctance motor drives. *IEEE Transactions on Power Electronics*, **31**(10), 7087–7098.

Peng, F., Ye, J., and Emadi, A. (2016). A digital pwm current controller for switched reluctance motor drives. *IEEE Transactions on Power Electronics*, **31**(10), 7087–7098.

Radun, A. (1994). Generating with the switched reluctance motor. In *Proceedings of 1994 IEEE Applied Power Electronics Conference and Exposition-ASPEC'94*, pages 41–47. IEEE.

Rafiq, M., Rehman, S.-u., Rehman, F.-u., Butt, Q. R., and Awan, I. (2012). A second order sliding mode control design of a switched reluctance motor using super twisting algorithm. *Simulation Modelling Practice and Theory*, **25**, 106–117.

Rahman, K., Rajarathnam, A., and Ehsani, M. (1997). Optimized instantaneous torque control of switched reluctance motor by neural network. In *IAS'97. Conference Record of the 1997 IEEE Industry Applications Conference Thirty-Second IAS Annual Meeting*, volume 1, pages 556–563. IEEE.

Rajendran, A. and Padma, S. (2012). H-infinity robust control technique for controlling the speed of switched reluctance motor. *Frontiers of Electrical and Electronic Engineering*, **7**(3), 337–346.

Richter, E. (1988). High temperature, lightweight, switched reluctance motors and generators for future aircraft engine applications. In *1988 American Control Conference*, pages 1846–1851. IEEE.

Richter, E. and Ferreira, C. (1995). Performance evaluation of a 250 kw switched reluctance starter generator. In *IAS'95. Conference Record of the 1995 IEEE Industry Applications Conference Thirtieth IAS Annual Meeting*, volume 1, pages 434–440. IEEE.

Rigatos, G., Siano, P., and Ademi, S. (2019). Nonlinear h-infinity control for switched reluctance machines. *Nonlinear Engineering*, **9**(1), 14–27.

Sadeghzadeh, A. and Araabi, B. N. (2006). Auto-tune predictive control of switched reluctance motor. In *2006 IEEE International Symposium on Industrial Electronics*, volume 1, pages 335–340. IEEE.

Sahoo, S. K., Panda, S. K., and Xu, J.-X. (2004). Iterative learning-based high-performance current controller for switched reluctance motors. *IEEE Transactions on Energy Conversion*, **19**(3), 491–498.

Sahoo, S. K., Panda, S. K., and Xu, J.-X. (2005). Indirect torque control of switched reluctance motors using iterative learning control. *IEEE Transactions on Power Electronics*, **20**(1), 200–208.

Sahoo, S. K., Panda, S. K., and Jian-Xin Xu (2005). Indirect torque control of switched reluctance motors using iterative learning control. *IEEE Transactions on Power Electronics*, **20**(1), 200–208.

Sahoo, S. K., Dasgupta, S., Panda, S. K., and Xu, J.-X. (2011). A lyapunov function-based robust direct torque controller for a switched reluctance motor drive system. *IEEE Transactions on Power Electronics*, **27**(2), 555–564.

Schulz, S. E. and Rahman, K. M. (2003). High-performance digital pi current regulator for ev switched reluctance motor drives. *IEEE Transactions on industry applications*, **39**(4), 1118–1126.

Schulz, S. E. and Rahman, K. M. (2003). High-performance digital pi current regulator for ev switched reluctance motor drives. *IEEE Transactions on Industry Applications*, **39**(4), 1118–1126.

Seshadri, A. and Lenin, N. C. (2019). Review based on losses, torque ripple, vibration and noise in switched reluctance motor. *IET Electric Power Applications*, **14**(8), 1311–1326.

Shang, W., Zhao, S., Shen, Y., and Qi, Z. (2009). A sliding mode flux-linkage controller with integral compensation for switched reluctance motor. *IEEE Transactions on Magnetics*, **45**(9), 3322–3328.

Shang, W., Zhao, S., Shen, Y., and Qi, Z. (2009). A sliding mode flux-linkage controller with integral compensation for switched reluctance motor. *IEEE Transactions on Magnetics*, **45**(9), 3322–3328.

Shtessel, Y., Edwards, C., Fridman, L., and Levant, A. (2014). *Sliding mode control and observation*. Springer.

Sira-Ramírez, H., Linares-Flores, J., García-Rodríguez, C., and Contreras-Ordaz, M. A. (2014). On the control of the permanent magnet synchronous motor: An active disturbance rejection control approach. *IEEE Transactions on Control Systems Technology*, **22**(5), 2056–2063.

Song, S., Fang, G., Hei, R., Jiang, J., Ma, R., and Liu, W. (2020). Torque ripple and efficiency online optimization of switched reluctance machine based on torque per ampere characteristics. *IEEE Transactions on Power Electronics*, **35**(9), 9610–9618.

Spall, J. C. and Cristion, J. A. (1998). Model-free control of nonlinear stochastic systems with discrete-time measurements. *IEEE Transactions on Automatic Control*, **43**(9), 1198–1210.

Sun, Q., Wu, J., and Gan, C. (2020a). Optimized direct instantaneous torque control for srms with efficiency improvement. *IEEE Transactions on Industrial Electronics*, **68**(3), 2072–2082.

Sun, X., Wu, J., Lei, G., Guo, Y., and Zhu, J. (2020b). Torque ripple reduction of srm drive using improved direct torque control with sliding mode controller and observer. *IEEE Transactions on Industrial Electronics*.

Szamel, L. (2002). Model reference adaptive control of srm drives, epe-pemc 2002, 10th int. In *Power Electronics and Motion Control Conf., Cavtat & Dubrovnik (Croatia)*, page 466.

Taylor, D. G. (1990). Improved pulse-width modulated control of switched reluctance motors. In *1990 American Control Conference*, pages 2083–2088. IEEE.

Taylor, D. G. (1991). Adaptive control design for a class of doubly-salient motors. In *[1991] Proceedings of the 30th IEEE Conference on Decision and Control*, pages 2903–2908. IEEE.

Tsakalis, K. and Ioannou, P. (1987). Adaptive control of linear time-varying plants. *Automatica*, **23**(4), 459–468.

Ustun, O. (2009). A nonlinear full model of switched reluctance motor with artificial neural network. *Energy conversion and management*, **50**(9), 2413–2421.

Üstün, O. and Önder, M. (2020). An improved torque sharing function to minimize torque ripple and increase average torque for switched reluctance motor drives. *Electric Power Components and Systems*, **48**(6-7), 667–681.

Utkin, V. and Drakunov, S. (1989). On discrete-time sliding modes. *IFAC Proceedings Volumes*, **22**(3), 273–278.

Valenciagarcia, D. F., Tarvirdilu-Asl, R., Garcia, C., Rodriguez, J., and Emadi, A. (2020). A review of predictive control techniques for switched reluctance machine drives. part ii: Torque control, assessment and challenges. *IEEE Transactions on Energy Conversion*.

Wang, S. (2017). Conductive emi issues in power electronics systems. In *2017 IEEE International Symposium on Electromagnetic Compatibility & Signal/Power Integrity (EMCSI)*, pages 1–110. IEEE.

Wang, S. and Liu, Y. (2011). A modified pi-like fuzzy logic controller for switched reluctance motor drives. *IEEE Transactions on Industrial Electronics*, **58**(5), 1812–1825.

Wang, S.-C. and Liu, Y.-H. (2010). A modified pi-like fuzzy logic controller for switched reluctance motor drives. *IEEE Transactions on Industrial Electronics*, **58**(5), 1812–1825.

Weiss, C. P., Singh, S., and De Doncker, R. W. (2020). Radial force minimization control for fault tolerant switched reluctance machines with distributed inverters. *IEEE Transactions on Transportation Electrification*.

Wu, W., Dunlop, J. B., Collocott, S. J., and Kalan, B. A. (2003). Design optimization of a switched reluctance motor by electromagnetic and thermal finite-element analysis. *IEEE Transactions on Magnetics*, **39**(5), 3334–3336.

Wu-Chung Su, Drakunov, S. V., and Ozguner, U. (2000). An o(t^2) boundary layer in sliding mode for sampled-data systems. *IEEE Transactions on Automatic Control*, **45**(3), 482–485.

Xia, Z., Bilgin, B., Nalakath, S., and Emadi, A. (2020). A new torque sharing function method for switched reluctance machines with lower current tracking error. *IEEE Transactions on Industrial Electronics*.

Xue, X., Cheng, K. W. E., and Ho, S. L. (2009). Optimization and evaluation of torque-sharing functions for torque ripple minimization in switched reluctance motor drives. *IEEE transactions on power electronics*, **24**(9), 2076–2090.

Ye, J., Malysz, P., and Emadi, A. (2014). A fixed-switching-frequency integral sliding mode current controller for switched reluctance motor drives. *IEEE Journal of Emerging and Selected Topics in Power Electronics*, **3**(2), 381–394.

Ye, J., Malysz, P., and Emadi, A. (2015). A fixed-switching-frequency integral sliding mode current controller for switched reluctance motor drives. *IEEE Journal of Emerging and Selected Topics in Power Electronics*, **3**(2), 381–394.

Ye, J., Bilgin, B., and Emadi, A. (2015). An offline torque sharing function for torque ripple reduction in switched reluctance motor drives. *IEEE Transactions on energy conversion*, **30**(2), 726–735.

Yu, Q., Bilgin, B., and Emadi, A. (2015). Loss and efficiency analysis of switched reluctance machines using a new calculation method. *IEEE Transactions on Industrial Electronics*, **62**(5), 3072–3080.

Zhang, M., Bahri, I., Mininger, X., Vlad, C., and Berthelot, E. (2019a). Vibration reduction control of switched reluctance machine. *IEEE Transactions on Energy Conversion*, **34**(3), 1380–1390.

Zhang, X., Yang, Q., Ma, M., Lin, Z., and Yang, S. (2019b). A switched reluctance motor torque ripple reduction strategy with deadbeat current control and active thermal management. *IEEE Transactions on Vehicular Technology*, **69**(1), 317–327.

Zhao, T., Wu, Y., and Gui, X. (2019). A modified current predict controll with incremental inductance and resistance self-learning for switched reluctance machines. In *2019 22nd International Conference on Electrical Machines and Systems (ICEMS)*, pages 1–6. IEEE.

Zhu, Z.-Q. and Howe, D. (2007). Electrical machines and drives for electric, hybrid, and fuel cell vehicles. *Proceedings of the IEEE*, **95**(4), 746–765.